May 2020

Behavior of Iron Species and Free Radicals in Ambient PM2.5 and PM Surrogates

Cholena Russo Ren
Louisiana State University and Agricultural and Mechanical College

BEHAVIOR OF IRON SPECIES AND FREE RADICALS IN AMBIENT $PM_{2.5}$ AND PM SURROGATES

A Dissertation

Submitted to the Graduate Faculty of the
Louisiana State University and
Agricultural and Mechanical College
in partial fulfillment of the
requirements for the degree of
Doctor of Philosophy

in

The Department of Chemistry

by
Cholena Russo Ren
B.S., University of West Florida, 2012
August 2020

ACKNOWLEDGMENTS

Accomplishments in my work and career–academic and professional–would not have been possible without the support of my family and mentors. First, I would like to acknowledge my family. My husband, Alexander Ren, supported me financially and emotionally through my graduate career. Thank you for making sacrifices and being by my side. I could not have done it without you. Love endures everything. I would also like to thank my parents, Robert and Sandra Russo, who taught me to never give up.

Next, I would like to acknowledge my mentors. Dr. Tim Royappa and Dr. Fred Hileman were excellent mentors during my undergraduate years. They taught me valuable skills that have gone a long way in my graduate studies. I cannot thank them enough for their superior teaching and advice. I am blessed to have had two great mentors.

Last, I would like to thank my first graduate advisor, Dr. Barry Dellinger, who accepted me into his group. May he rest in peace. Before you became ill, you encouraged me to pursue a fellowship. I will never forget the smile on your face when I shared the that I had been awarded a fellowship. That smile brought me so much joy, then and still now, in my memory. I know you will be here in spirit to see me graduate.

I also want to give special recognition to Dr. Robin McCarley. When my confidence about continuing my graduate career waivered, Dr. McCarley believed in me. If not for his support, I would not be here today. Dr. McCarley went above and beyond his responsibilities as a graduate professor; he became my second graduate advisor when he did not have to. I want to thank you, Dr. McCarley, for making this dream possible.

It has been a long journey and well worth this moment. I appreciate and am grateful for all the support and good will that helped me, and that continues to lead me on. Thank you to all of those who have made this possible and God bless.

TABLE OF CONTENTS

LIST OF FIGURES

LIST OF IMAGES

LIST OF SCHEMES

LIST OF ABBREVIATIONS

DPPH	2,2-diphenyl-1-picrylhydrazyl
EPFRs	Environmentally Persistent Free Radicals
EPR	Electron Paramagnetic Resonance Spectroscopy
FT-IR	Fourier-Transform Infrared Spectroscopy
PAHs	Polycyclic Aromatic Hydrocarbons
PM	Particulate Matter
$PM_{0.1}$	Particulate Matter less than 0.1 μm or less in aerodynamic diameter
$PM_{2.5}$	Particulate Matter less than 2.5 μm or less in aerodynamic diameter
PM_{10}	Particulate Matter less than 10 μm or less in aerodynamic diameter
PTFE	Polytetrafluoroethylene
ROS	Reactive Oxygen Species
SEM	Scanning Electron Microscopy
TEM	Transmission Electron Microscopy
UV-Vis/NIR	Ultraviolet-Visible/Near-Infrared Spectroscopy
VOCs	Volatile Organic Compounds
XPS	X-ray Photoelectron Spectroscopy
XRD	X-ray Diffraction
XRF	X-ray Fluorescence Spectroscopy

ABSTRACT

Air pollution, consisting of ambient particulate matter (PM), has been a rising health concern to the public. PM contains free radicals and have been known to damage human cells; however, their free radical chemistry is not well understood. This study utilized various vacuum and/or heat treatments to study free radical behavior in $PM_{2.5}$ (particulate matter with an aerodynamic diameter of 2.5 μm or less) and PM surrogates and simulated sunlight effects on $PM_{2.5}$. To mimic PM, iron-silica catalysts (i.e. PM surrogates) were synthesized and real-world ambient $PM_{2.5}$ was selected. The free radicals in $PM_{2.5}$ have been referred to as environmentally persistent free radicals (EPFRs). It has been proposed that EPFR formation happens when phenol vapor is exposed to the iron surfaces of PM surrogates yielding a narrow electron paramagnetic resonance (EPR) signal with a *g*-factor of 2. However, adsorption of phenol on PM surrogates at room temperature did not form EPFRs, but poly(*p*-phenylene) material was detected. Free radical formation was observed when the phenol-exposed PM surrogates were heated above 300 °C. Ferric iron associated with superparamagnetic nanoparticles (less than 4 nm in diameter) as well as free radicals were shown to yield a narrow $g = 2$ EPR signal in PM surrogates and obey the Curie-Weiss Law. Distinguishing between the superparamagnetic nanoparticles and free radicals was accomplished by the experimental steps used on PM surrogates. Superparamagnetic behavior of the nanoparticles was observed by heating PM surrogates to 120 °C under ambient conditions yielding an increased intensity of the narrow $g = 2$ EPR signal while free radicals did not respond to this heat treatment. This was the first time the heating treatments were used to identify superparamagnetic species in $PM_{2.5}$. Also, adventitious carbon yielded a small $g = 2$ EPR signal and was observed in PM surrogates and the polytetrafluoroethylene filters used to collect $PM_{2.5}$. To further gain an understanding of the changes at the $g = 2$ EPR signal under

environmental conditions, $PM_{2.5}$ was exposed to simulated sunlight but did not demonstrate any changes to the intensity.

CHAPTER 1. INTRODUCTION

1.1. Purpose and hypotheses

Environmentally persistent free radicals (EPFRs) found in ambient $PM_{2.5}$ (particulate matter with an aerodynamic diameter of 2.5 μm or less) have been previously described as having an underlying link to health effects. The behaviors of these radicals in ambient $PM_{2.5}$ under environmental conditions are not well understood. Therefore, the purpose of this work was to: (1) assess radical behavior in ambient $PM_{2.5}$ by conducting various heating and/or vacuum treatment, and at times, combining this with phenol exposures on ambient $PM_{2.5}$ and PM surrogates; (2) understand how environmental conditions such as sunlight affects sustainability of the radicals; and (3) correlate changes in behavior of radicals between ambient $PM_{2.5}$ and PM surrogates under the controlled environments. The following hypotheses were assumed: (1) ambient $PM_{2.5}$ and PM surrogates exposed to vapor-phase phenol will produce higher concentrations of radicals; (2) exposure of simulated sunlight will generate higher concentrations of radicals in ambient $PM_{2.5}$; and (3) ambient $PM_{2.5}$ and PM surrogates with higher metal content will yield higher concentrations of radicals.

1.2. Origin, composition, and sizes of atmospheric particulate matter

Many reactions of atmospheric aerosols and interactions of tiny particle formation take place in the atmosphere. Atmospheric particulate matter (PM) can be found in the troposphere, the lower atmosphere of the Earth. As PM forms, it takes on different sizes and compositions at various stages. The four different steps involved in PM formation starts with the nucleation mode. The nucleation mode enables vapor-phase reactions to form particles in sizes of about 1 nm. Next, the Aitken mode is where these 1 nm particles interact with combustion-generated particles and other small man-made matter to either aggregate or react with some other species

that may condensate at the particle surface and form 100 nm particles. This leads to a third, accumulation, mode where additional condensation and aggregation take place forming larger particles of 2.5 μm or less in aerodynamic diameter. Finally, the course mode progresses with more condensation and aggregation growing leading to particles of 10 μm or less in aerodynamic diameter (Griffin, 2013). A particle's aerodynamic diameter is defined as a unit density sphere that has the same settling velocity as the particle (Sjoholm et al., 2001). The PM sizes matters because the smaller the particles, the longer they remain suspended in the air. Also, PM sizes matter from a human health perspective.

Smaller PM can be inhalable by humans. The first size of inhalable PM is PM_{10} or particulate matter 10 μm or less in aerodynamic diameter. PM_{10} can be inhaled into the upper parts of the respiratory system and is commonly classified as course particles. This matter is commonly composed of natural matters like sea salt, dust, mold spores, and pollen. The next smaller size of inhalable PM is $PM_{2.5}$, referred to as fine particles that have an aerodynamic diameter of 2.5 μm or less. $PM_{2.5}$ consists of man-made combustion-generated particles like, metals, sulfates, nitrates, and organic matter. Subsequently, $PM_{0.1}$ or ultrafine particles, consists of a similar composition as $PM_{2.5}$ and has an aerodynamic diameter of 0.1 μm or less. The smaller the particles are, the deeper they can infiltrate and deposit more into the respiratory system (EPA, 2018). The health effects caused by the inhalation of PM of any size (further discussed in Section 1.5. Toxicity of $PM_{2.5}$), has sparked interest in scientific communities leading to further investigations of causal factors in PM's composition (Hazari et al., 2018; Polichetti et al., 2009). Smaller size fractions of PM like $PM_{0.1}$ are more of a health concern but are also difficult to collect. Therefore, $PM_{2.5}$ is the focus of this study.

1.3. Free radicals in combustion-generated particles

The combustion processes emit toxic air pollutants into the atmosphere, such as nitrogen dioxide, sulfur dioxide, lead, carbon monoxide, volatile organic compounds (VOCs), and particulate matter. Combustion is a high temperature heating process that takes place in atmospheric air resulting in complete and incomplete combustion. Ambient $PM_{2.5}$ consists of combustion-generated particles. Figure 1.1 shows the combustion process starts with zone 1 where fuel is introduced; zone 2 involves ignition and exothermic reactions; zone 3 concludes with the formation of various pollutants. As the combustion process transitions from zone 2 to zone 3, a release of organic vapors allows for the nucleation mode to initiate. Metals may condense or aggregate on particle surfaces (Aitken and accumulation modes) during zone 3 (Cormier et al., 2006).

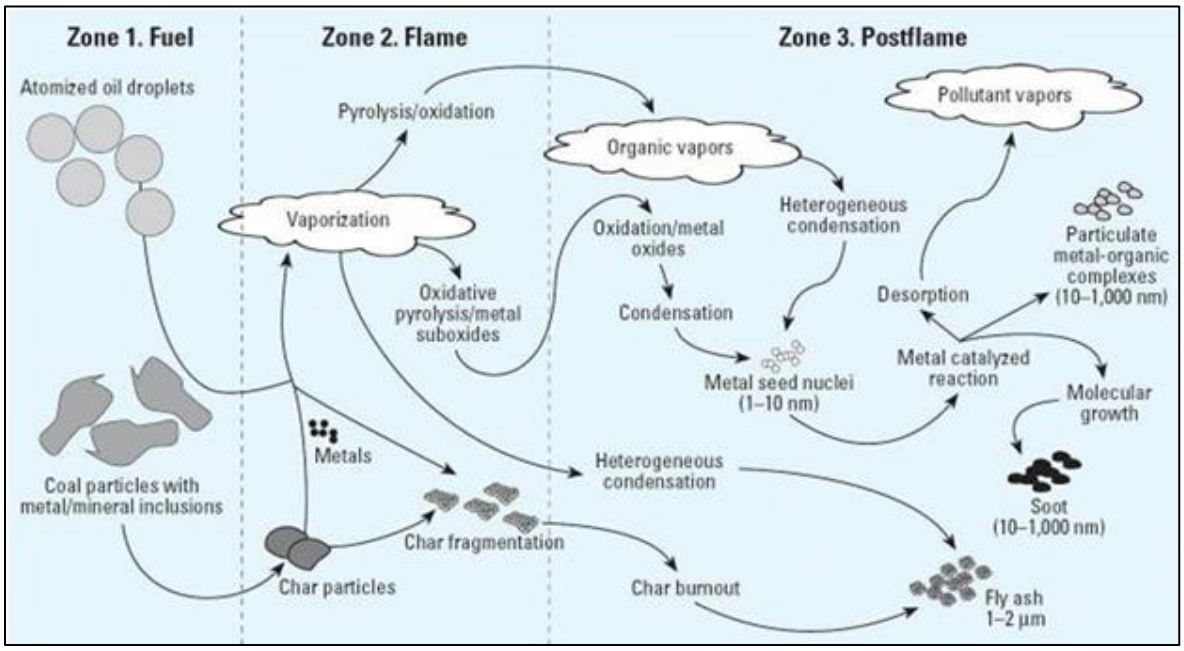

Figure 1.1. Zones of the combustion process and their products (Cormier et al., 2006). Reproduced with permission from Environmental Health Perspectives.

In the end, the combustion process produces metal-organic particulates or soot that contains free radicals. These free radicals can form a three-step reaction. Step one is called

initiation: here heat breaks down a stable molecule into free radicals. Followed by step two, propagation, this is where free radicals can then react with other stable molecules to form additional free radicals. The final involves termination, where two radicals react to form stable molecules (Upadhyay, 2006). Free radicals are very reactive and can live long in the environment. Therefore, it is important to investigate the chemical kinetics of free radicals because of their persistency in the ambient atmosphere.

There are different types of free radicals. One type, carbon-centered free radicals, has been previously detected in combustion-generated particles (Tian et al., 2009; Valavanidis et al., 2008). Carbon-centered free radicals have a characteristic *g*-factor value of about 2.0035 as detected by electron paramagnetic resonance (EPR) spectroscopy. The *g*-factor of an absorption signal in the EPR spectrum is important, because it is related to the electronic environment. For example, a carbon-centered radical has a lower *g*-factor value compared to an oxygen-centered radical. Values of *g*-factors between 2.0030–2.0040 suggest a carbon-centered radical with a nearby oxygen atom. From previous reports it was found free radicals detected in ambient $PM_{2.5}$ yield an EPR signal with a *g*-factor value between 2.0030–2.0038 (Dellinger et al., 2001; Gehling et al., 2013).

Combustion-generated particles, such as soot, contribute to the free radicals identified in ambient $PM_{2.5}$. It is easier to control and collect soot than to sample for ambient $PM_{2.5}$. Thus, soot has been widely studied, in part as a proxy for PM. Also reports have detected polycyclic aromatic hydrocarbons (PAHs) in soot (Guarieiro et al., 2014; Richter et al., 2000). PAHs are a group of aromatic organic compounds known for their toxic properties.

Dr. Herring and his coworkers investigated the lifetime of free radicals in soot and soot-iron oxide particles. The lifetime is how long it takes for the initial EPR signal intensity to

decrease by $1/e$. The soot utilized was generated from a custom-designed dual zone reaction combustion system using the PAH 1-methylnapthlene (Herring et al., 2013). Two lifetimes were reported on radical species yielding *g*-factors of about 2.0030. The radical species produced from the pyrolysis of 1-methylnapthlene had a lifetime of 1.8 days. The other radical species had a higher EPR signal intensity due to the addition of iron and reported a longer lifetime of 2.9 days (Herring et al., 2013). This longer lifetime of 2.9 days indicates this species can be long-lived in the environment.

Experiments involving the burning of tobacco in air at room temperature also indicated its soot yielded an EPR signal with a *g*-factor around 2.0030 and revealed more than one radical species (Church et al., 1985). It was proposed that the EPR signal with a *g*-factor at 2.0030 correlates to a quinone radical species. Quinones are derived from aromatic compounds. The results were demonstrated from the addition of aromatic compounds (catechol or 1,4-naphthoquinone) to the tobacco. This, followed by burning the tobacco under ambient atmosphere, caused a significant increase in the intensity of the EPR signal. Furthermore, metal ions were added to tobacco for testing. Zinc showed an increase in the EPR signal intensity while copper reduced the intensity. Another species yielding an EPR signal with a *g*-factor of 2.0028 was also reported; however, it was not identified (Church et al., 1985).

More recently, oxygen-centered semiquinone-type radicals were identified with a *g*-factor of 2.0053 after the pyrolysis of tobacco containing added catechol or hydroquinone. Species at a *g*-factor of 2.0035 were associated with phenoxyl-type radicals and carbon-centered semiquinone-type radicals with an oxygen nearby (Maskos et al., 2005). Different resonance structures for semiquinones and phenoxyl radicals are shown in Scheme 1.1. Two slightly different free radical species, presented simultaneously, may cause the EPR signals to overlap

and may appear as one signal. Shifts in the *g*-factor value may help to explain which radical types are more abundant.

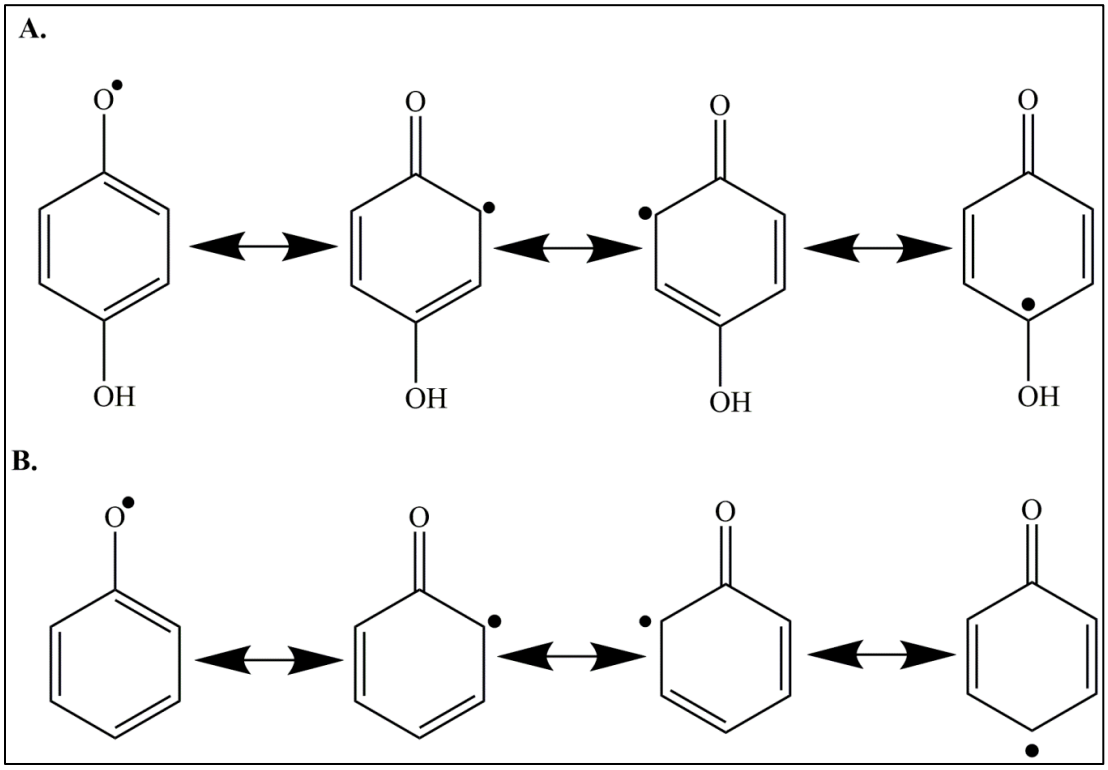

Scheme 1.1. Resonance structures of A. semiquinone radicals and B. phenoxyl radicals.

1.4. Proposed mechanism for EPFR formation in combustion systems

It has been suggested that semiquinones or phenoxyl radicals may be stabilized via their interactions with the surfaces of transition metal oxides. The stable free radicals observed at a *g*-factor of around 2.0030 have been referred to as Environmentally Persistent Free Radicals (EPFRs). A proposed mechanism for EPFR formation is displayed in Scheme 1.2 (Dellinger et al., 2000; Lomnicki et al., 2008).

Formations of EPFRs are thought to occur in the post-flame region (also referred to as cool zone, Figure 1.1) combustion process by surface-mediated reactions between phenolic and quinone compounds and metal oxides. Metal oxides are known to have a charged surface layer of hydrous metal oxides. Due to van der Waals forces, the hydroxide group on the organic

precursor is statically drawn to the hydrous metal oxide. This step is referred to as a physisorption (shown by the dotted line in Scheme 1.2). The next step is chemisorption, which takes place during thermal treatment and results in loss of water and formation of a chemical bond. An electron transfer from the organic precursor to the metal oxide form stable semiquinones or phenoxyl radicals. These EPFRs could have a combination of oxygen and carbon-centered radicals. Previous research has found the presence of EPFRs in ambient $PM_{2.5}$ (Dellinger et al., 2000; Dellinger et al., 2001; Gehling et al., 2013).

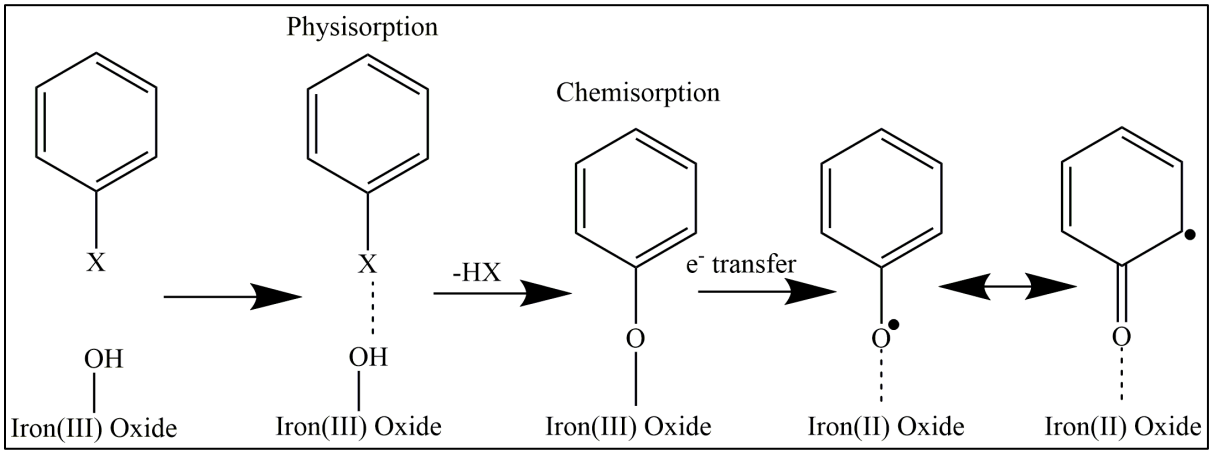

Scheme 1.2. Proposed mechanism for the formation of EPFRs.

1.5. Toxicity of $PM_{2.5}$

Research has demonstrated health effects from $PM_{2.5}$, such as asthma, decreased lung function, heart attack, and premature death (Brook Robert et al., 2010; Pope et al., 2011; West et al., 2016). Because $PM_{2.5}$ is commonly emitted and has been correlated with increased health risks, it has been listed as a major air pollutant under the Clean Air Act. The enactment of the Clean Air Act of 1963 was triggered by a historic air pollution event in Donora, Pennsylvania known as the “Donora smog of 1948”. The smog event was caused by two U.S. Steel plants that released toxic pollutants into the atmosphere, which killed 20 people and sickened thousands of others (Hamill). $PM_{2.5}$ significantly contributes to smog events by reducing visibility and

increasing health risks. In 2013, the International Agency for Research on Cancer and World Health Organization listed PM as carcinogenic to humans (IARC.). Today, the U.S. Environmental Protection Agency is responsible for regulating $PM_{2.5}$ through the National Ambient Air Quality Standards.

A recent study revealed that free radicals in $PM_{2.5}$ are the suspected cause for cardiovascular health effects. Hazari and coworkers found increased heart rate variability in mice when mice were exposed to particulate matter (Hazari et al., 2018). The smaller the size of particulate matter, the more likely it can enter the blood stream causing increased heart rates.

Free radicals are known to generate exogenous reactive oxygen species (ROS) in the body that cause oxidative stress (Krötz et al., 2002). Studies have detected microorganisms, such as bacteria, fungi, and the common cold virus, found in $PM_{2.5}$ allows for transportation of viruses into the lungs (Du et al., 2018). The combined effects of induced ROS and exposure to microorganisms results in lowered immunity, which makes humans more susceptible to illnesses. Scheme 1.3 shows a previously proposed mechanism for ROS generation initiated by the semiquinone radical obtained from the EPFR mechanism (Dellinger et al., 2000). ROS are natural in the human body, but imbalances in ROS can lead to cellular damage. Hydroxyl radicals are known to do the most cellular damage and are a byproduct of Fenton reactions (Cadet et al., 1999). Fenton reactions occur between a redox-active transition metal and hydrogen peroxide to form hydroxyl radicals (Dellinger et al., 2011; Lakey et al., 2016; Valavanidis et al., 2005). The presence of redox-active transition metals could be significant in understanding health implications caused by ROS imbalances. The presence of transition metals in ambient $PM_{2.5}$, such as iron, copper, and zinc, could be triggering ROS imbalances caused by inhalation of ambient $PM_{2.5}$ (Duan et al., 2013; Lakey et al., 2016; Rogula-Kozłowska et al.,

2014). Therefore, the role of transition metals in free radical formation and ROS needs further investigation.

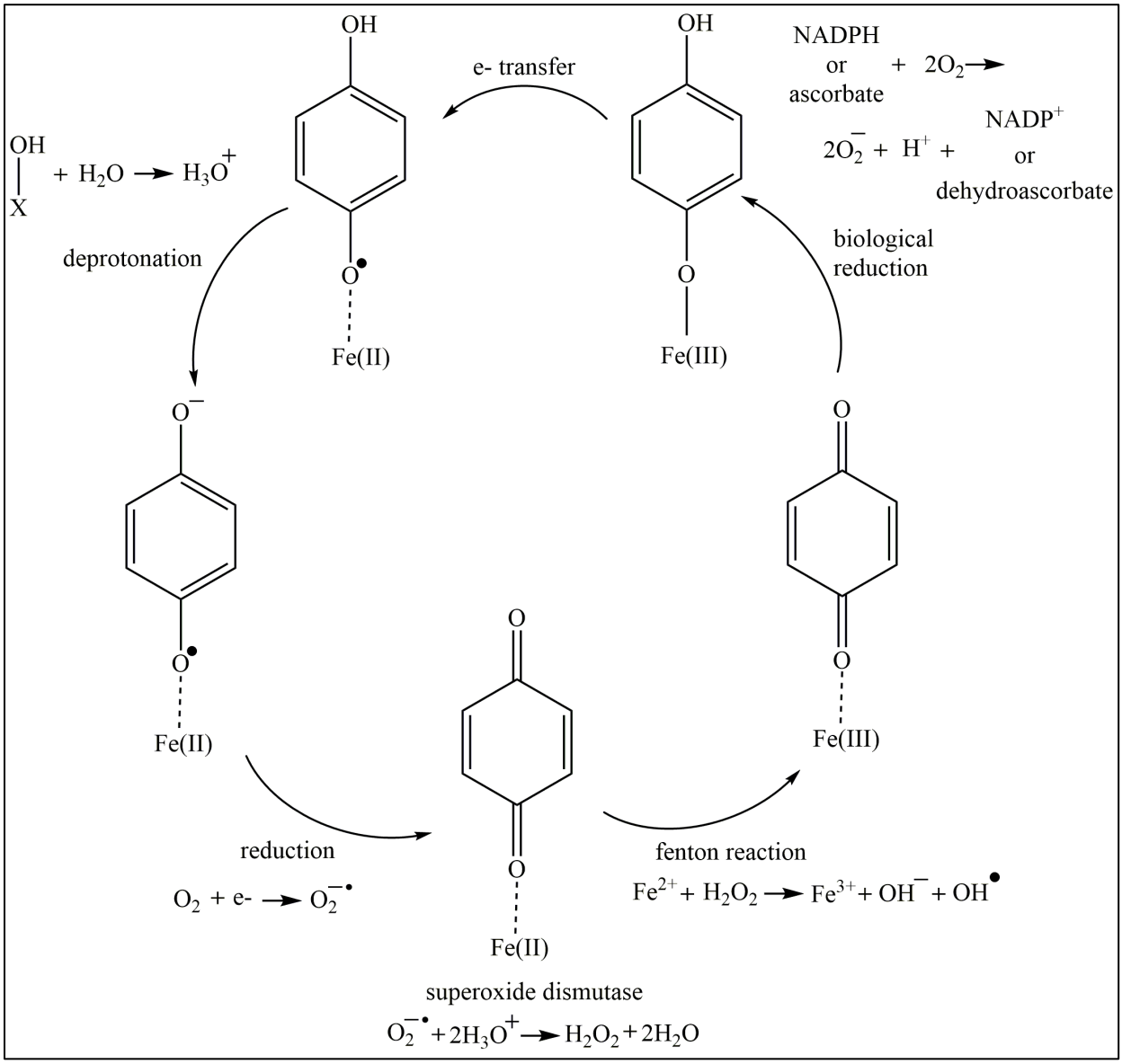

Scheme 1.3. Proposed mechanism for ROS formation.

1.6. Heterogeneous catalyst as PM surrogate

For experiments, a surrogate for ambient $PM_{2.5}$ is important for the following reasons: (1) ambient $PM_{2.5}$ is a heterogeneous complex mixture of matter; (2) various metals are frequently detected in ambient $PM_{2.5}$ composition; and (3) unknown formed EPFR species are

already present in ambient $PM_{2.5}$. Heterogeneous catalysts composed of a metal and silica have been previously demonstrated as ideal surrogates for combustion particles and the formation of EPFRs and thus may serve as surrogates for ambient $PM_{2.5}$. Vejerano and coworkers formed EPFRs on a heterogeneous catalyst composed of 5% iron-silica particles exposed to vapor-phase phenol. The 5% iron-silica particles—synthesized using silica gel—were exposed to vapor-phase phenol at temperatures between 150–400 °C and demonstrated EPFR formation with characteristic *g*-factors around 2.0030–2.0040. Experiments carried out with vapor-phase phenol at 400 °C demonstrated slightly higher *g*-factor values. It was reported that these higher *g*-factors were a result of the decomposition of phenoxyl radicals that led to the formation of cyclopentadienyl radicals on metal surfaces (Vejerano et al., 2011). Though an iron-silica material appears to be an ideal PM surrogate for EPFR formation, other research demonstrated iron-silica particles—synthesized using silica gel—produced an EPR signal with a *g*-factor around 2.0030 after heat treatment without any exposure to vapor-phase organics (Beletskii, 1980). The absence of an exposed organic suggest the EPR signal with a *g*-factor around 2.0030 signal may not correlate to EPFR presence. Accordingly, experimental procedures should be carefully examined when conducting vapor-phase exposure studies with the PM surrogate.

Other researchers have also demonstrated EPFR formation with different metal oxides-silica materials; however, iron and silica were chosen for the PM surrogate in this study because of its abundance in nature and frequent detection in ambient $PM_{2.5}$ (Ault et al., 2012; Cheung et al., 2012; Gehling et al., 2014; Kiruri et al., 2014; Patterson et al., 2017; Patterson et al., 2013; Vejerano et al., 2012). Kiruri and coworkers demonstrated EPFR formation with different vapor-phase organics on copper oxide-silica surrogates having various copper oxide concentrations from 0.25% through 5%. The EPFRs formed, using 2-monochlorophenol and phenol as the

organic precursors, on the 1% copper oxide-silica surrogates exhibited a longer lifetime than surrogates with higher copper oxide concentrations (Kiruri et al., 2014). Metal content in the metal-silica PM surrogates appears to affect the lifetime and persistency of EPFRs, and there is a lack of literature on examining heterogeneous iron-silica particles with metal concentrations less than 1% by EPR.

Preferably, a surrogate for ambient $PM_{2.5}$ needs to have a low concentration of metal, because there are low concentrations of ambient $PM_{2.5}$ in the atmosphere. In the United States, the daily National Ambient Air Quality Standard for $PM_{2.5}$ is 35 $\mu g/m^3$ of air (EPA, 2020). The less PM there is to collect the lower the metal concentration will be and exposure to humans. However, a low metal concentration can be challenging to detect within instrumental detection limits. Because previous studies have demonstrated significant differences in EPFR formation by EPR with other metal concentrations less than 1%, the PM surrogate used in this study also used concentrations less than 1%.

1.7. Adsorption of phenol on iron surfaces

For EPFR formation phenol was chosen as the organic precursor for two reasons. One, methyl groups on benzene were shown to sterically hinder chemisorption to goethite, an iron oxyhydroxide mineral, surfaces (McBride et al., 1991). Because phenol's structure is simple with only a hydroxyl group attached to the benzene, it has a low steric hindrance in comparison with other aromatic compounds. Additionally, oxygenated-PAHs have been detected in ambient PM (Koenig et al., 1983). Second, it has been shown that phenol-exposed iron-silica materials yield EPFRs with a significantly longer lifetime than copper-silica materials so it seems best to utilize phenol to further investigate EPFR formation (Vejerano et al., 2012).

Vapor-phase exposure experiments with phenol have been previously shown to adsorb on surfaces of amorphous iron oxide and goethite. A proposed mechanism for chemisorption of phenol on surfaces of hematite (α-Fe_2O_3) and goethite (FeO(OH)) is shown in Scheme 1.4 (McBride et al., 1991). Interestingly, the mechanism does not indicate formation of free radical species, but it is very similar to the proposed EPFR mechanism. Now adsorption of phenol on iron surfaces in aqueous solution is not desirable nor does it account for condensation, which is an important contribution to $PM_{2.5}$ formation (Griffin, 2013). Most surface sites of an iron-silica material would be taken up by water molecules. Thus, vapor-phase exposure experiments are best to simulate the condensation process.

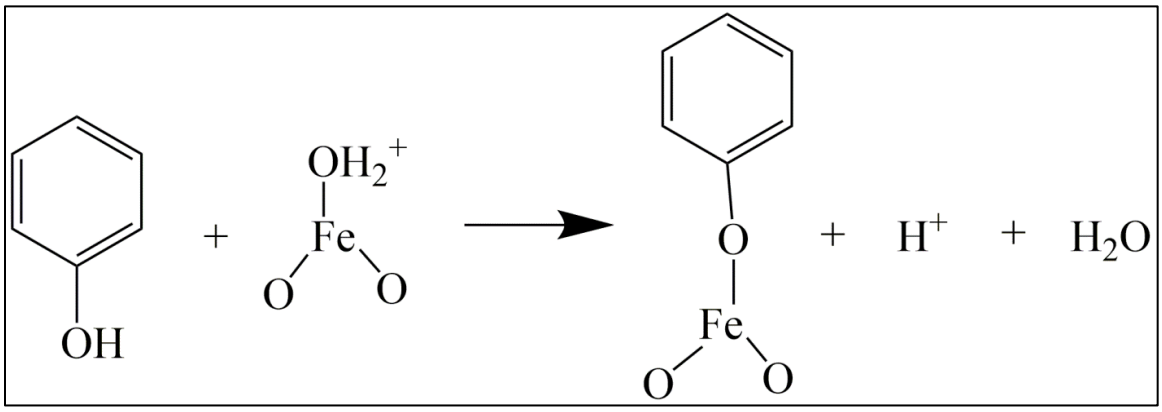

Scheme 1.4. Chemisorption of phenol on iron protonated hydroxyl groups.

1.8. Synthesis of catalysts on silica supports

The synthesis of heterogeneous catalysts is crucial for reproducibility of the catalytic activity and thus can affect free radical/EPFR formation. Factors that could change a catalyst's activity include particle size, pH, temperature, grinding, vacuum, concentrations, and wetting time. A catalyst can be prepared two ways: by bulk or support. Supported catalysts would be best to mimic ambient $PM_{2.5}$, because lower metal concentrations can be achieved. Therefore, impregnation techniques are utilized to synthesize supported metal catalysts. There are two impregnation techniques that could be used: (1) wet impregnation; (2) incipient wetness

impregnation. Wet impregnation is prepared with an excess solution, whereas incipient wetness impregnation is when the volume of the solution is less than or equal to the volume of the support's pores. Wet impregnation is a slower diffusional process, but incipient wetness impregnation is ideal because it is faster by allowing capillary action to occur to quickly draw solution within the support's pores (Marceau, 2009).

Some previous EPFR formation studies previously discussed have used silica gel as the support to prepare metal oxide particles instead of fumed silica (Vejerano et al., 2011). However, in this work, the support used in the incipient wetness impregnation technique to model ambient $PM_{2.5}$ was fumed silica. Fumed silica was chosen over silica gel because fumed silica has a higher specific surface area. Materials higher in specific surface area have smaller particle sizes. Fumed silica and silica gel are amorphous so they are less irritating to the respiratory tract compared to silica materials that are crystalline (Merget et al., 2002). Thus, amorphous silica makes it a better choice to use if one were to reproduce this work to conduct health exposure studies.

In addition to determining a suitable support, solvents used to prepare the catalysts should also be considered. Previous investigations of nickel(II) oxide (NiO) on silica support particles created using the incipient wetness impregnation technique demonstrated changes in NiO particles sizes based on different solvent used to dissolve the solute (Liyanage, 2014). Particles prepared with methanol had an average diameter of 3.6 nm compared to 49.1 nm for preparation in water. It is known that the catalyst support, silica, is hydrolyzed when water is added limiting ligand substitution between metal ions and silica, unlike methanol which allows for the formation of nickel silicates (Liyanage, 2014). Additionally, the samples prepared with methanol had a low size dispersity of the NiO particles compared to the samples prepared in water

(Liyanage, 2014). Therefore, preparation of catalysts using water is more realistic to use in the preparation of the PM surrogate than methanol, because water vapor is commonly found in the environment and ambient $PM_{2.5}$ heterogeneous composition would have higher size dispersity.

1.9. Effects of experimental treatment on catalytic activity

Vacuum pressure is another important factor to consider when examining chemical changes. Many previous studies on EPFR formation between vapor-phase organic precursors and metal oxides took place under thermal and vacuum treatment. Simultaneous thermal and vacuum treatment of cobalt oxide particles on a silica support demonstrated smaller, more uniform, and less aggregated particles compared to cobalt-silica particles just thermally exposed to air. Therefore, the particles treated under vacuum and heat had a higher catalytic activity (Zhou et al., 2011). Aggregation is a common behavior for particles formed from combustion systems and could affect the activity of free radical/EPFR formation. Other literature also has suggested that vacuum and heat treatments leads to changes in the coordination environment of ferric ions (Fe^{3+}) on a silica support (Bordiga et al., 1996).

1.10. Metal coordination environments in silicate materials

Previous studies related to this work have identified that framework and extra-framework iron species play a critical role in the occurrence of a broad EPR signal with a *g*-factor of 2 in analogous PM surrogates which is nearby the suspected EPFR EPR signal. It was also identified that the EPR signal with a *g*-factor of 4.3 is of importance for ferric ions and this was not investigated in previous EPFR formation studies on iron-silica materials. Previous reports on iron-silica materials have correlated EPR signals with a *g*-factor at 2 (broad) and 4.3 to changes in the ferric ions coordination environment (Berlier et al., 2002; Bordiga et al., 1996; Goldfarb et al., 1994; Lin et al., 1989). Thus, it is important when using the PM surrogates to examine EPR

signals with *g*-factors at 2 (broad) and 4.3. EPR can help identify changes in a metal's coordination environment by undergoing zero field splitting. It was previously investigated by Bordiga and coworkers that an iron silicate framework with an undistorted tetrahedral coordination environment yields an EPR signal with a *g*-factor of 2 (broad) when exposed to ammonia (NH_3). This is because the positive ion on protonated ammonia (NH^{+4}) allows for a charge balance in the iron silicate framework (Bordiga et al., 1996; Tuel et al., 1998).

Accordingly, a distorted tetrahedral coordination environment yielding an EPR signal with a *g*-factor of 4.3 is feasible when NH_3 is removed by heat and vacuum treatment as displayed in Scheme 1.5. Based on these results, it is suggested that Brønsted acid sites, where a proton (H^+) is donated, causes ferric ions to be in distorted tetrahedral coordination environments in an iron silicate framework. Similarly, this can relate to adsorbed water as shown in Scheme 1.6. In addition to the undistorted tetrahedral coordination, octahedral coordination environments for isolated ferric ions in extra-framework sites or iron oxide nanoparticles (experiencing superparamagnetism) could also be present (Bhaumik et al., 2005; Bordiga et al., 1996; Geinguenaud et al., 2015; Lassoued et al., 2017; Tuel et al., 1998).

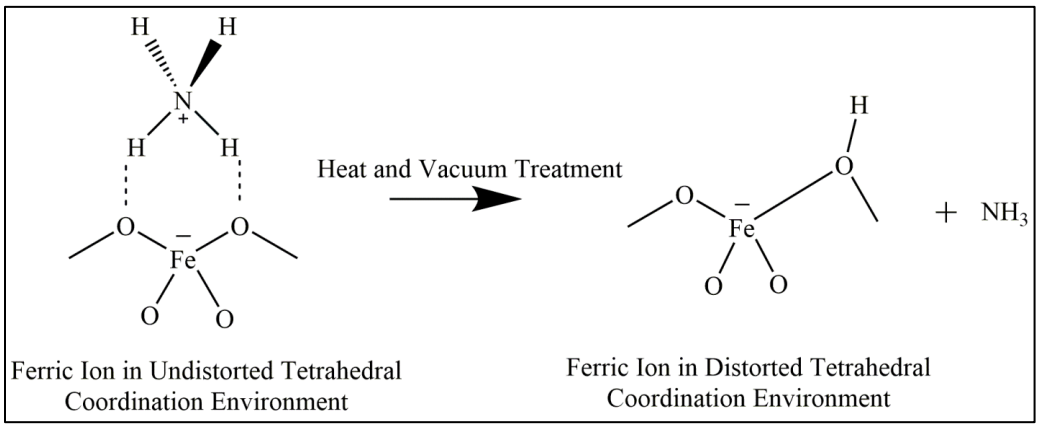

Scheme 1.5. Removal of adsorbed NH_3 (NH_4^+) on iron-silica material by heat and vacuum treatment.

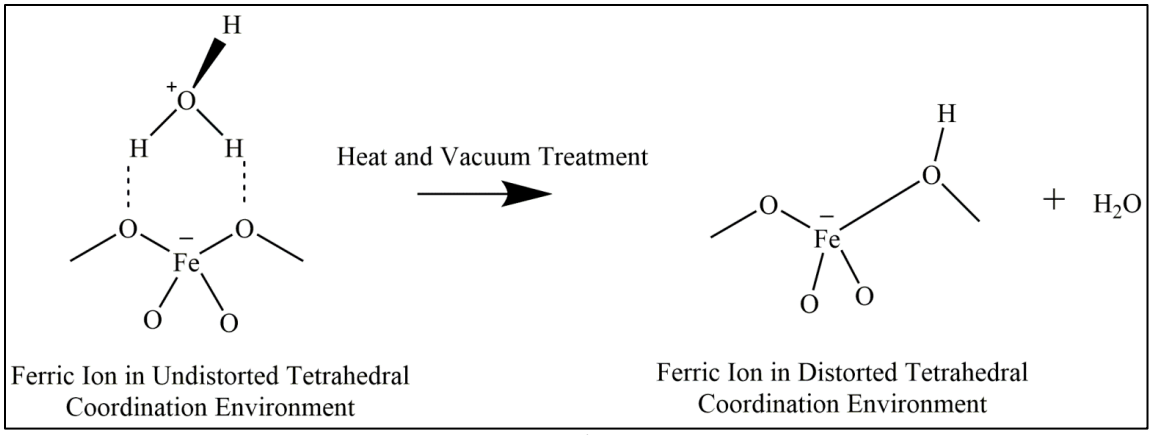

Scheme 1.6. Removal of adsorbed H_2O (H_3O^+) on iron-silica material by heat and vacuum treatment.

Furthermore, a water dehydration and rehydration effect was observed in zeolites (aluminosilicate minerals) with iron, analogous to the PM surrogates. Lin and coworkers reported three kinds of ferric ion sites from EPR spectroscopy, but only detected two from Mössbauer spectroscopy data. The first identified ferric ion site exhibited a distorted tetrahedral coordination environment caused by Brønsted acid sites and yielded an EPR signal with a *g*-factor of 4.3. It was suggested that the other ferric ion sites yield EPR signals with *g*-factors of 2.3 and 2.0 (broad) and correspond to undistorted tetrahedral coordination environments for different charges on silica and iron. As noted earlier, the Mössbauer spectroscopy data only found two iron sites, one of tetrahedral coordination and the other distorted tetrahedral coordination, so the two EPR signals with *g*-factors at 2.3 and 2.0 (broad) both appear to exhibit tetrahedral coordination (Lin et al., 1989). The dehydration and rehydration effect is further supported by other literature and describes the process as reversible (Tuel et al., 1998). Overall, it is important to investigate the dehydration and rehydration effect in the PM surrogate (iron-silica) because it has similar components to the materials used in previous studies and may help to explain changes in observed EPR signals.

On the other hand, others reported that the *g*-factor signal at 2.3 could correlate to "iron aggregates" as a result of excess iron precursor in materials with higher iron concentrations (Berlier et al., 2002; Goldfarb et al., 1994). The iron sites yielding an EPR signal with a *g*-factor of 2.3 were not found when iron content was lowered to 1% (Berlier et al., 2002). A combination of low iron content and heating temperatures on an already synthesized iron-silica material increases bond breaking of ferric ion sites leading to the formation of small iron oxide nanoparticles or isolated ferric ions in extra-frameworks both of which exhibit octahedral coordination and may be attributed to a narrow EPR signal with a *g*-factor around 2.0 (Berlier et al., 2002). A conflicting study reported higher iron content yielded less tetrahedral coordination and more octahedral coordination environments (Amama et al., 2005). Some of the PM surrogates will be using iron concentrations less than 1% in this study. Therefore, it is important to note any EPR signals with a *g*-factor at 2.3 or 2.0 and their changes.

In a different case, the decomposition of methane on a 2% iron-silica material identified two EPR signals with *g*-factors at about 2.0030. It was suggested that narrow one of the EPR signals corresponded to carbon radicals that followed the Curie-Weiss law (where ferromagnetic properties transition to a paramagnetic state), while the other (broad EPR signal), associated with the Brønsted acid sites, did not (Weckhuysen et al., 1997). This reveals the literature views for the identification of the EPR signals with *g*-factors at 2.3 and 2.0 slightly differ.

In addition, effects of solvent treatment on the extra-framework iron species/iron oxide particles have also been previously investigated. Samples prepared prior to calcination treatment, without using solvent extraction to remove amine groups exhibited a brown color consisting of the iron species in an octahedral coordination. Thus, solvent extraction could avoid formation of isolated ferric ions in extra-framework sites/iron oxide particles (Tuel et al., 1998). However, as

discussed earlier, using solvents is not ideal for simulating ambient $PM_{2.5}$ formation and so, for the purpose of this work, it should be avoided. Also, isolated ferric ions in extra-framework sites/iron oxide particles could be present in the ambient $PM_{2.5}$ and have not yet been investigated.

Interestingly, iron-silica materials were not the only metal-silica materials with observed changes in the coordination environments. Studies on copper oxide-silica materials exhibited changes in coordination environments yielding an EPR signal with a *g*-factor of 2.0030 (Gervasini et al., 2006; Loktev et al., 1976; Sagar, 2015). Both square planar and octahedral coordination were reported for the copper sites (Sagar, 2015).

Overall, the isolated ferric ions in extra-framework sites or iron oxide nanoparticles (i.e., ferric ions associated with superparamagnetic nanoparticles) yielding a narrow EPR signal with a *g*-factor around 2.0 can led to an observation of radical EPR signals that appear like the EPFR/organic radicals. Depending on preparation conditions and what one is trying to learn about radical stability and presence, it may be very hard to determine radical concentrations using the narrow EPR signal with a *g*-factor at ~2.003. Thus, examining how simulated sunlight may affect the narrow EPR signal with a *g*-factor at ~2.003 may be unfeasible. To identify EPR signals attributed to free radicals and ferric ions associated with superparamagnetic nanoparticles examining EPR signals with *g*-factors at 4.3, 2.0 (broad and narrow), and 2.3 and their changes under experimental treatments can be used.

CHAPTER 2. MATERIALS AND METHODS

2.1. Collection of ambient $PM_{2.5}$

2.1.1. PQ200 ambient air particulate air sampler

The PQ200 particulate air sampler equipped with a very sharp cut cyclone from BGI Instruments by Mesa Labs was used for collecting ambient $PM_{2.5}$ (Kenny et al., 2000). The PQ200 is an approved federal reference method by the U.S. Environmental Protection Agency with approved procedures defined in the Code of Federal Regulations Title 40 Part 50. Approved federal reference methods are preferred over non-federal reference methods because the approved methods have been tested to ensure the accuracy and dependability of the pollutant ($PM_{2.5}$) collected. It is important to note that the median particle size range is not used for this type of sampling collection because it would introduce bias. However, it is possible that particles (> 2.5 μm) could get on the filter, before or after collecting ambient $PM_{2.5}$, because the filter is exposed to the ambient atmosphere. Furthermore, using federal reference methods provides consistency with sampling in other locations. The ambient $PM_{2.5}$ was collected on top of a building located in Baton Rouge, Louisiana at the Recreation and Park Commission for the Parish of East Baton Rouge (BREC) Memorial Sports Complex. Ambient $PM_{2.5}$ was collected for 23 hrs/day on a 46.2-mm diameter polytetrafluoroethylene (PTFE) Whatman filter with a pore size of 2 μm (product number 7592-104). Collection periods that are longer can affect the flow rate, thereby causing variation in particle sizes. The flow rate of the PQ200 was set to 16.7 L/min and was calibrated using a deltaCal air flow calibrator from BGI Instruments by Mesa Labs. Verifications of the flow were conducted weekly in accordance with manual operation procedures (Labs).

After collection, sampled filters were stored and sealed in a labelled antistatic plastic bag and kept at 0 °C until use. Sample weights were < 0.8 mg. No extraction techniques were performed to remove ambient $PM_{2.5}$ from the filters. Before experiments were conducted on ambient $PM_{2.5}$, the sampled filters were handled carefully with PTFE tweezers and were cut to remove the support ring on the filter using PTFE-coated razors so that the sampled filters could be easily placed in small EPR tubes. Experiments conducted on ambient $PM_{2.5}$ were used from this sampling method unless specified.

2.1.2. Tisch environmental high-volume air sampler

A high-volume ambient air sampler from Tisch Environmental (TE-6070V-2.5) was also used for the collection of ambient $PM_{2.5}$. However, the TE-6070V-2.5 ambient air sampler is a non-federal reference method. The shim plate in the high-volume ambient air sampler was coated with Molykote 316 silicon release spray. The silicon-greased shim plate removes the larger particles greater than 2.5 μm in diameter. The silicon-greased shim plate was cleaned once a week. Ambient $PM_{2.5}$ was collected on an 8 by 10-inch binder-free Whatman glass microfiber filters (grade GF/A) for three to four weeks at a raised platform located on Aster Street across from the West Campus apartments on Louisiana State University's campus in Baton Rouge, Louisiana. The TE-6070V-2.5 ambient air sampler flow rates were maintained at 1,100 L/min and calibrated weekly using a TE-5028 variable flow calibration kit. After collection, sampled filters were stored in a labelled bag and kept at 0 °C until extraction experiments. The ambient $PM_{2.5}$ on the filter was extracted in 50 mL of 18 MΩcm water and then shaken and sonicated for 20 min in a beaker. Large filter pieces were removed, and the remaining solution was transferred to glass tubes and centrifuged. The top portion of the solution was transferred to ceramic

crucibles and dried at 102 °C in an oven for 5 h (Gehling, 2013). The dried ambient $PM_{2.5}$ was then transferred to sealed glass vials and kept at 0 °C under ambient atmosphere until analysis.

2.2. Total organic carbon analysis

A Costech 1040 CHNOS (carbon, hydrogen, nitrogen, oxygen, and sulfur) elemental combustion system was used to measure total weight % of nitrogen and carbon in samples.

2.3. X-ray diffraction

A PANalytical Empyrean x-ray diffractometer was used to analyze samples. X-ray diffraction (XRD) parameters were set to the following: copper for anode material, scan range 5–90 degrees, continuous scan type, scan step size of 0.026 degree/step, time per step of 46.665 sec/step, and 3,237 number of points.

2.4. X-ray photoelectron spectroscopy

A Kratos/AXIS 165 XPS/AES using a monochromatic-aluminum X-ray beam was used to analyze samples. The PM surrogate samples were pressed into a 1 mm pellet and placed on carbon tape. X-ray photoelectron spectroscopy (XPS) parameters were set to the following: 700–742 eV scan range, 0.1 eV step, 157.5 ms dwell time, 2 scans, and pass energy of 40 eV.

2.5. X-ray fluorescence spectroscopy

X-ray fluorescence (XRF) spectroscopy was used to analyze samples. XRF was conducted at the Center for Advanced Microstructures and Devices (CAMD) in Baton Rouge, Louisiana. XRF parameters were set to the following: 9 keV gain, 300 s integration time, 14,353 eV excitation energy, 15 cm distance, and 1.5 cm^2 active area.

2.6. Transmission electron microscopy

The samples were imaged using a JEM-1011 high-resolution transmission electron microscope. All samples were placed on a 400-mesh holey-carbon-coated copper grid from SPI Supplies. The ImageJ software program was used to measure any observed lattice spacings.

2.7. Diffuse reflectance ultraviolet-visible/near-infrared spectroscopy

A Cary 5000 ultraviolet-visible/near-infrared (UV-Vis/NIR) spectrophotometer with an internal diffuse reflectance accessory (Internal DRA 900) was utilized to take measurements of the samples. A small powder cell kit from Agilent (catalog number 9910111400) was used for sample loading. The advantage to using the DRA is that it allows solid samples like the PM surrogates to be analyzed. The DRA measures the light reflected from the surface of particles. UV-Vis/NIR is useful when color changes are observed because the color of the material affects the spectral reflectance. UV-Vis/NIR parameters were set to the following: double beam mode double, reduced slit height, 1 s average time, 2 nm data interval, 120 nm/min scan rate, 2 nm slit band width, 800 nm grating change wavelength, and 900 nm for the detector change wavelength.

2.8. Thermogravimetric analysis

A thermogravimetric analyzer (TA Instruments, Q500 V6.7) was utilized to measure the weight loss of sample at high temperatures. The temperature range started at room temperature going up to 600 °C at 10 °C/min.

2.9. Scanning electron microscopy

The samples were imaged using a JSM-6610 LV scanning electron microscopy (SEM) at room temperature in the secondary electron imaging mode. All samples were placed on conductive adhesive Kapton tape. Energy dispersive spectroscopy (SEM-EDS) was attempted on ambient $PM_{2.5}$ but was unsuccessful due to the PTFE filter burning in analytical mode.

2.10. Electron paramagnetic resonance spectroscopy

A Bruker EMX–10/2.7 electron paramagnetic resonance (EPR) spectrometer was used to measure samples at room temperature. All samples were placed into a 10 mm Suprasil EPR tube purchased from Wilmad (product number 733-3PQ-7). EPR spectrometer settings were set to the following: 9.76 GHz microwave frequency, 100 kHz modulation, 2.05 mW attenuation power, 4.0 G modulation amplitude, 100-G or 5000-G scan range, 40.96 ms time constant, 163.84 ms conversion time, 167.77 s sweep time, 3.56×10^4 receiver gain, and 1 scan at a resolution of 1024 points. Empty cavity measurements were taken to ensure the cavity was clean from any contamination. In addition, a solid 2,2-diphenyl-1-picrylhydrazyl (DPPH) standard sealed under vacuum was measured daily prior to sample measurements. The DPPH standard was used to detect deviations in the measured *g*-factor values (Eaton GR, 2010).

The *g*-factor values were reported because it provides information about the chemical properties of an electron interaction with the electronic structure. For an unpaired electron there are two possible spin states and when applied in a magnetic field a difference in energy can be measured (absorption of energy) by the following equation: $\Delta E = g\mu_B B_0$. The g represents the *g*-factor value, μ_B is a physical constant for the electron magnetic moment referred to as the Bohr magneton, and B_0 is the applied external magnetic field strength. These absorption spectra were then plotted as the first derivative. In continuous-wave EPR, spectra are reported in the first derivative because of the phase-sensitive detector. The phase-sensitive detector measures the amplitude that is dependent on the slope of the absorption signal (Eaton GR, 2010).

Any changes in a sample's EPR signal intensity was examined. It is important to note that EPR signal intensities can increase or decrease depending on the partial pressure of oxygen

because oxygen is a paramagnetic gas (Tian et al., 2009). Therefore, it is essential to report the conditions the sample is placed under, such as vacuum, during the EPR measurement.

2.11. Fourier-transform infrared spectroscopy

A Bruker Alpha Fourier-transform infrared (FT-IR) spectrometer equipped with a PT-diamond analyzer was used to measure samples. The sample holder (Pike Miracle attenuated total reflection [ATR]) was cleaned with acetone and dried before placing the powdered sample on the holder. FT-IR spectrometer settings were set to the following: scan range of 400–4000 cm^{-1}, averaging 3 scans, and a resolution of 4 cm^{-1}.

2.12. Thermal treatment on ambient $PM_{2.5}$

Ambient $PM_{2.5}$ collected on PTFE filters (using the collection method from Section 2.1.1) was placed in 10 mm Suprasil EPR tubes from Wilmad (product No. 733-3PQ-7) and heated to 120 °C in a ceramic cylinder heater purchased from OMEGA Engineering (product number CRFC-756/60A) under ambient atmosphere. Samples were then cooled down to room temperature under ambient atmosphere. EPR measurements were taken before and after thermal treatment under ambient atmosphere.

2.13. Synthesis of PM surrogates

2.13.1. Synthesis of 0.5% and 3% iron oxide-silica PM surrogates

Iron(III) nitrate nonahydrate ($Fe(NO_3)_3 \bullet 9H_2O$) had a 99%+ purity and was purchased from Acros Organics. The certificate of analysis for iron(III) nitrate nonahydrate detected the following elements: chloride (Cl), sulfate (SO_4^{2-}), copper (Cu), zinc (Zn), manganese (Mn), lead (Pb), calcium (Ca), sodium (Na), potassium (K), and arsenic (As). Fumed silica (SiO_2), or also referred to as CAB-O-SIL EH5, had a 99.9%+ purity and was donated from Cabot Corporation, Boston, Massachusetts. 0.5% and 3% iron-silica particles (i.e., PM surrogates) were prepared

using the incipient wetness impregnation method. Approximately 0.013 g (0.5%) or 0.078 g (3%) of iron(III) nitrate nonahydrate (Acros Organics, 99%+) was dissolved in 5 mL of 18 MΩ cm water in a beaker. The 18 MΩ cm water was obtained from a Barnstead NANOpure Diamond water purification system. Approximately 1 g of CAB-O-SIL EH-5 was added to the solution. The amount of grams of the iron(III) nitrate nonahydrate was calculated using the molecular weight and number of moles of Fe_2O_3. The beaker was covered with parafilm and placed in a hood for 24 h at ambient conditions. The sample was then transferred to a quartz combustion boat and placed in a tube furnace (Thermo Scientific, Lindberg/Blue M). The sample was heated to 120 °C for 12 h and calcined at 450 °C for 5 h under ambient atmosphere. The calcined material was then grinded using an agate mortar and pestle. After grinding, particles were then sieved to 63 μm using a stainless-steel fine test sieve from Sigma-Aldrich (catalogue number Z400165). Particles were also prepared without the iron(III) nitrate nonahydrate, hereinafter referred to as silica. An assessment of the bulk 0.5% iron-silica PM surrogates was carried out by an inductively coupled plasma optical emission spectrophotometer Varian-MPX. Samples were digested in nitric acid at 110 °C for 16 h. The measured amount was 1,745 ± 14 mg/kg of Fe (0.498 weight %). Also, the measured amount for Cu was 13.4 ± 0.3 mg/kg (0.00017 weight %) and for Al was 848 ± 31 mg/kg (0.000832 weight %).

2.13.2. Synthesis of soot and iron-soot PM surrogates

Soot and 0.5% iron-soot were generated using a dual zone reactor (Herring et al., 2013). A 2 mM solution of generation 4 polyproylenimine tetra-hexacontaamine dendrimer, methanol and iron(III) nitrate nonahydrate ($Fe(NO_3)_3 \bullet 9H_2O$) was used to prepare iron oxide-soot PM surrogates. Iron (III) nitrate nonahydrate ($Fe(NO_3)_3 \bullet 9H_2O$) had a 99%+ purity and was purchased from Acros Organics. The generation 4 polypropylenimine tetra-hexacontaamine

dendrimer was purchased from Sigma Aldrich. As shown in Figure 2.1, the 2 mM solution was injected into Zone 1 to generate iron oxide nanoparticles and then exposed to 1-methylnaphthalene at Zone 2. The 1-methylnaphthalene had ≥99.5% purity and was purchased from Sigma Aldrich. Samples were collected on fumed silica. The fumed silica (SiO_2), or also referred to as CAB-O-SIL EH5, had a 99.9%+ purity and was donated from Cabot Corporation.

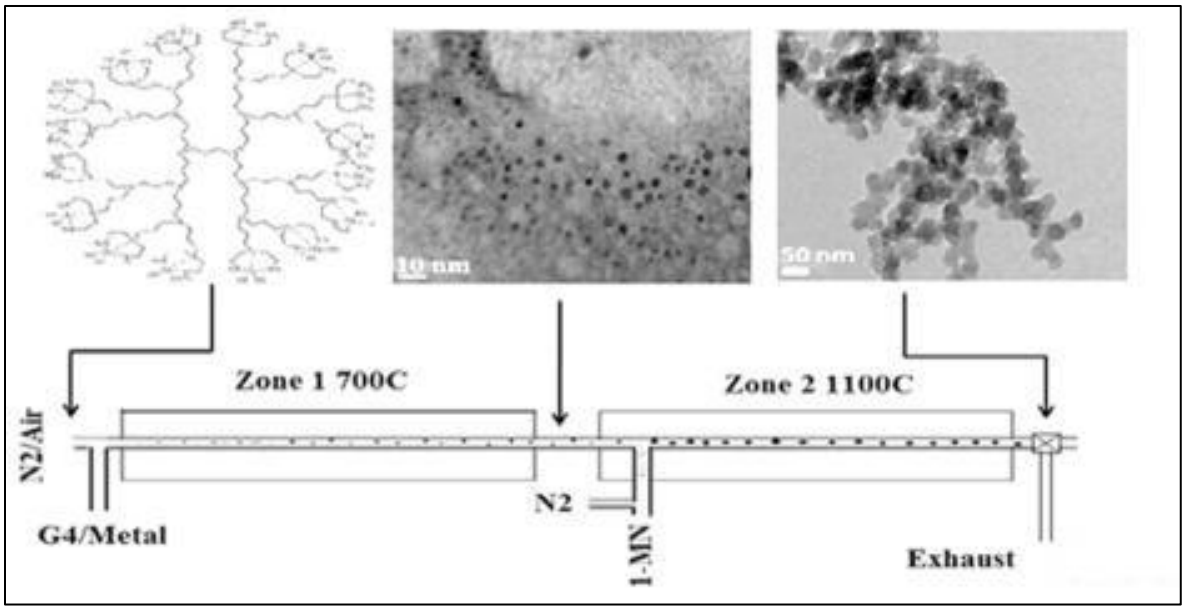

Figure 2.1. Dual zone reactor system showing TEM images of iron-soot particles (Herring, 2013). Reprinted from Proceedings of the Combustion Institute, 34, Fe_2O_3 nanoparticle mediated molecular growth and soot inception from the oxidative pyrolysis of 1-methylnaphthalene, 1749-1757. Copyright (2013), with permission from Elsevier.

2.14. Thermal and vacuum treatment on PM surrogates

As-prepared PM surrogates were placed in a 10 mm Suprasil EPR tube from Wilmad (product No. 733-3PQ-7) and heated under vacuum at 450 °C for 1 h while maintaining a pressure of 0.1–0.01 Torr. As shown in Figure 2.2, a custom designed apparatus was used to conduct experiments and is similar to what was used in previous EPFR formation studies (Vejerano, 2011). The as-prepared PM surrogates were then cooled to room temperature while maintaining a pressure of 0.1–0.01 Torr. EPR measurements were taken before experimental treatment under ambient atmosphere and after thermal/vacuum treatment under vacuum (*P* =

0.1–0.01 Torr) and then under ambient atmosphere. Furthermore, some thermal/vacuum treated PM surrogates were then heated to 120 °C for 1 h using a ceramic cylinder heater purchased from OMEGA Engineering (product number CRFC-756/60A) under ambient atmosphere.

2.15. Exposure of phenol to PM surrogates and ambient $PM_{2.5}$

The following steps were conducted using the custom-designed apparatus (Figure 2.2): as-prepared PM surrogates were placed in a 10 mm Suprasil EPR tube purchased from Wilmad (product number 733-3PQ-7), heated to 450 °C for 1 h while maintaining a pressure of 0.1–0.01 Torr, and cooled to room temperature while maintaining the pressure of 0.1–0.01 Torr. The valve to the phenol was then opened and the valve to the vacuum was closed. The PM surrogates were exposed to vapor-phase phenol while maintaining the pressure of 0.1–0.01 Torr for ~5 min at room temperature. After exposure, the valve to the vacuum was opened and the valve to the phenol was closed. The PM surrogates were maintained at a pressure of 0.1–.01 Torr for 1 h at room temperature to remove excess phenol. EPR measurements were taken before experimentation under ambient atmosphere, after thermal and vacuum treatment under vacuum (P = 0.1–0.01 Torr) at room temperature, and then after exposure to phenol under vacuum and ambient atmosphere. Some dosed-phenol PM surrogates were then followed up with additional thermal treatment under ambient atmosphere. Exposure of vapor-phase phenol to ambient $PM_{2.5}$ (using the collection method from Section 2.1.1) was conducted the same as the PM surrogates, but without the 450 °C treatment. The melting point of PTFE is 326.8 °C so the 450 °C would have melted the PTFE filter.

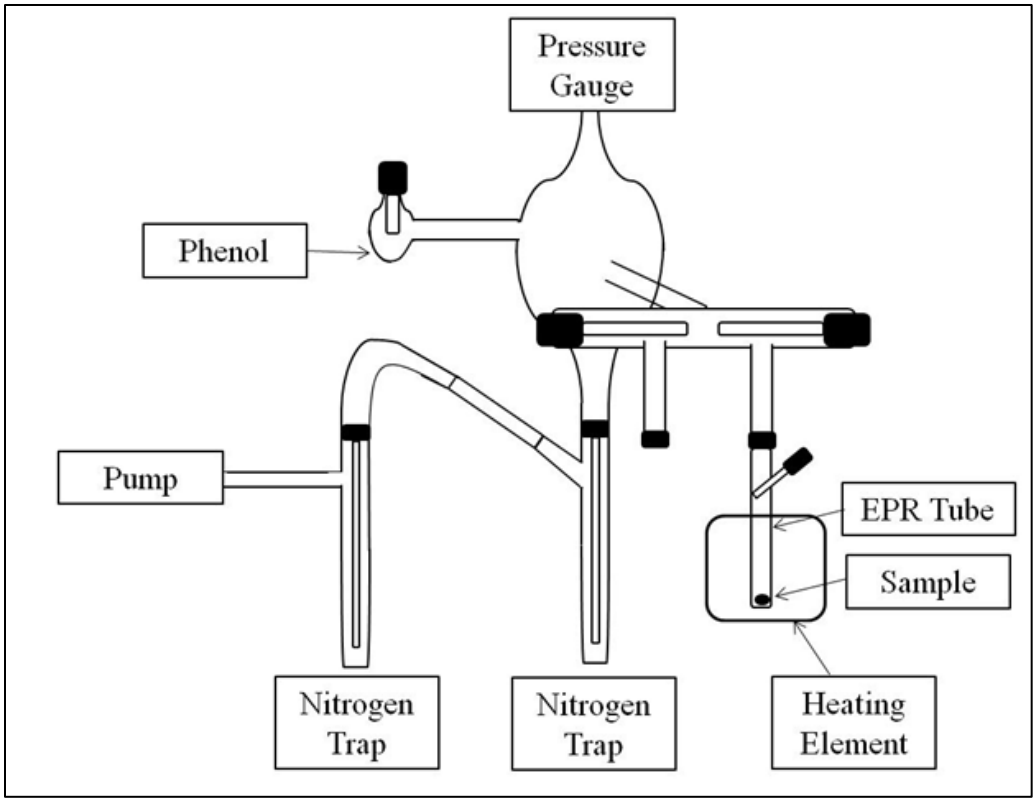

Figure 2.2. Custom designed apparatus used for conducting thermal/vacuum treatments and phenol exposure experiments.

2.16. Simulated sunlight exposures

Ambient $PM_{2.5}$ (Section 2.1.1 and 2.1.2) was transferred to a 10 mm Suprasil EPR tube from Wilmad (product No. 733-3PQ-7) and placed in a Forma environmental chamber (Thermo Fisher Scientific Model 3940) shown in Figure 2.3 to study sunlight effects. The chamber was kept at a temperature of 25 °C and humidity between 70–80 %. Samples were exposed to simulated sunlight from a universal xenon arc lamp from Newport with wavelength range of 185–2000 nm. The light produced from the xenon lamp was filtered using an air mass (AM) 1.5 filter from Campbell Scientific, which corresponds to a zenith angle of 48.2°. A LP02 pyranometer from Campbell Scientific was utilized to measure solar radiation from the filtered light. Simulated sunlight experiments were conducted with a solar radiation of 950 W/m^2 that represents Baton Rouge's average during midday. Temperature measurements taken during

exposure of simulated sunlight for 1 h showed the samples could reach between temperatures between 50–80 °C. EPR measurements were taken at 30 minutes and 60 minutes exposure periods followed by decay measurements.

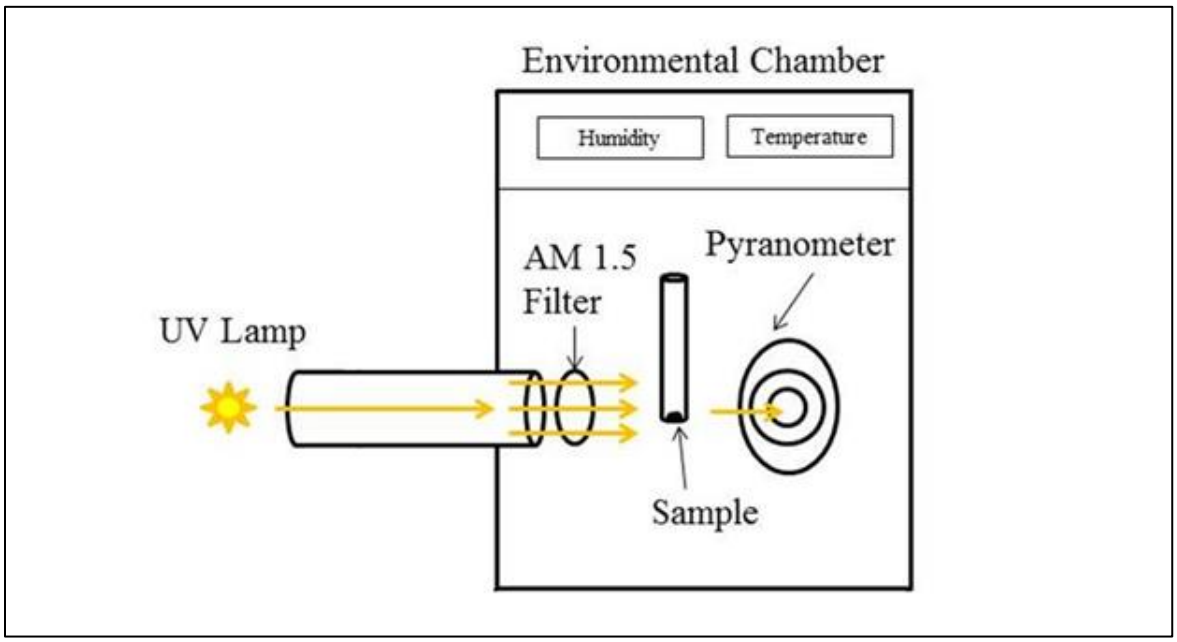

Figure 2.3. Design of simulated sunlight exposure experiments conducted in an environmental chamber to control temperature and humidity.

CHAPTER 3. CHARACTERIZATION OF PM SURROGATES AND AMBIENT $PM_{2.5}$

Various forms of iron oxides and hydroxides/oxyhydroxides such as hematite, magnetite, goethite, lepidocrocite, and ferrihydrite can exist in iron-containing materials like ambient $PM_{2.5}$ and PM surrogates. Iron hydroxides/oxyhydroxides are known to be present around temperatures below 200 °C and can transform into different forms of iron oxides during heating (Balek et al., 1995; Bernal, 1959; Dixon et al., 1989; Goss, 1987; Schwertmann et al., 1983). To help examine the forms of iron and particles sizes, XPS, XRD, XRF, TEM, and SEM characterization techniques were utilized. Ambient $PM_{2.5}$ discussed in this chapter used samples collected using the method described in Section 2.1.1.

3.1. Characterization of PM surrogates

3.1.1 Total organic carbon studies of PM surrogates

A total organic carbon (TOC) analyzer was used to determine the amount of carbon in the silica and 3% iron-silica PM surrogate. The total organic carbon present was 0.069 wt% and 0.256 wt% for the silica and 3% iron-silica PM surrogate, respectively. The addition of the iron(III) nitrate nonahydrate increased the carbon content in the PM surrogates.

3.1.2. X-ray diffraction studies of PM surrogates

XRD was conducted on the 0.5% and 3% iron-silica PM surrogates to determine the phase of iron and silica. The XRD data on 0.5% iron-silica PM surrogate presented in Figure 3.1 indicated an XRD pattern for amorphous silica, but not for iron (Alcalá et al., 2006). The absence of sharp Bragg peaks in the XRD pattern of the 0.5% iron-silica PM surrogate indicates amorphous iron particles or the low metal concentrations were below the detection limits of the XRD instrument (Machala et al., 2007).

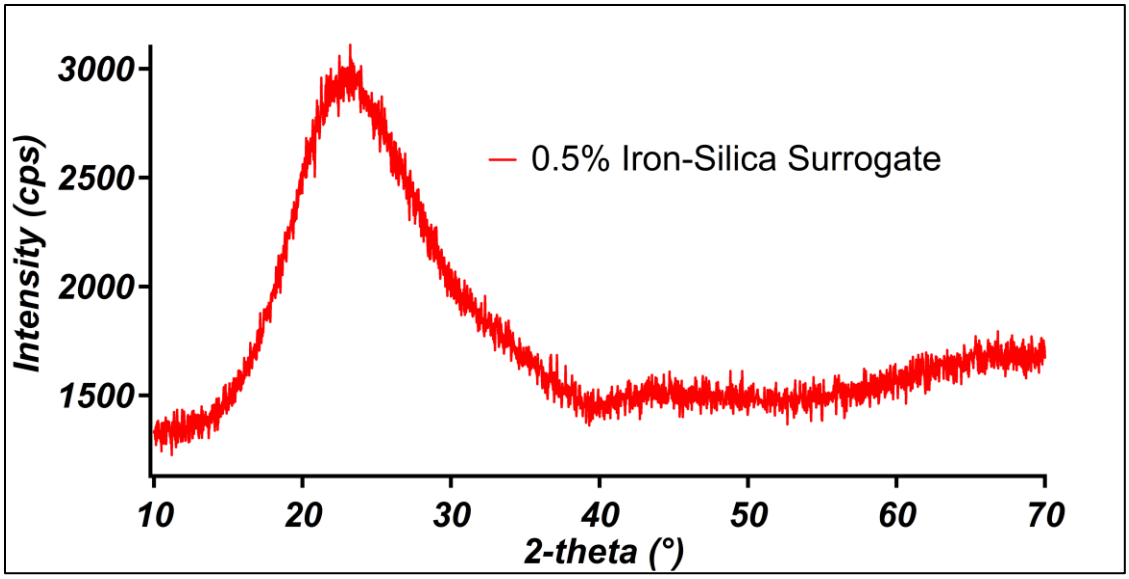

Figure 3.1. XRD spectrum 0.5% iron-silica PM surrogate.

As for the 3% iron-silica PM surrogate, the XRD pattern for amorphous silica was also observed, as shown in Figure 3.2. In addition, two low intense Bragg peaks in the XRD pattern, that indicate low crystallinity in the PM surrogate, around 33.0° and 35.6° were detected (Figure 3.2). The Bragg peaks at 33.0° and 35.6° in the XRD pattern are characteristic of hematite (α-Fe_2O_3) (Alcalá et al., 2006; Bourlinos et al., 2001; Li et al., 2016; Palomares-Sánchez et al., 2002; Yi et al., 2019). Calculated by the Scherrer equation, the particle diameter of hematite was ~0.014 μm. It was previously described that hematite forms at calcination temperatures of 400 °C, which is reasonably close to the 450 °C calcination temperature used to synthesize the iron-silica PM surrogates (Alcalá et al., 2006; Bourlinos et al., 2001). Furthermore, hematite is colored red, which agrees with the color observed in the 0.5% and 3% iron-silica PM surrogates (Hosseini-Zori et al., 2008).

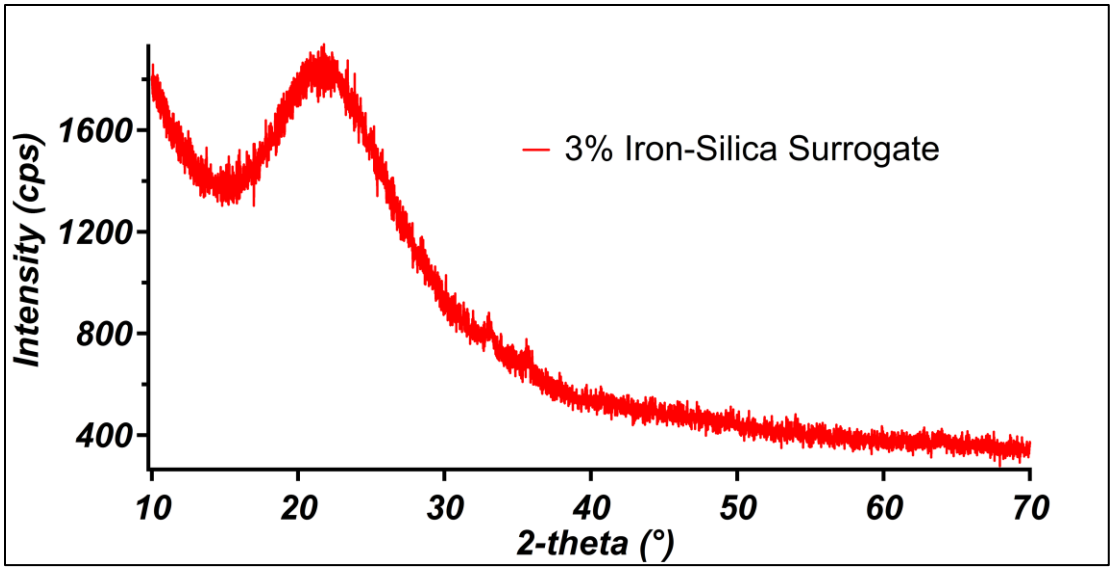

Figure 3.2. XRD spectrum of 3% iron-silica PM surrogate.

3.1.3. X-ray photoelectron spectroscopy studies of PM surrogates

XPS was conducted on the 0.5% iron-silica PM surrogates to identify any electron configurations of the elements silicon and iron. The XPS is a surface selective technique. It is important to examine particle surfaces by XPS because EPFRs were proposed to form stable radicals on iron surfaces (Dellinger et al., 2000; Lomnicki et al., 2008). As presented in Figure 3.3, a peak at ~102.2 eV was observed and corresponds to the 2p subshell for silicon (Bywalez et al., 2012).

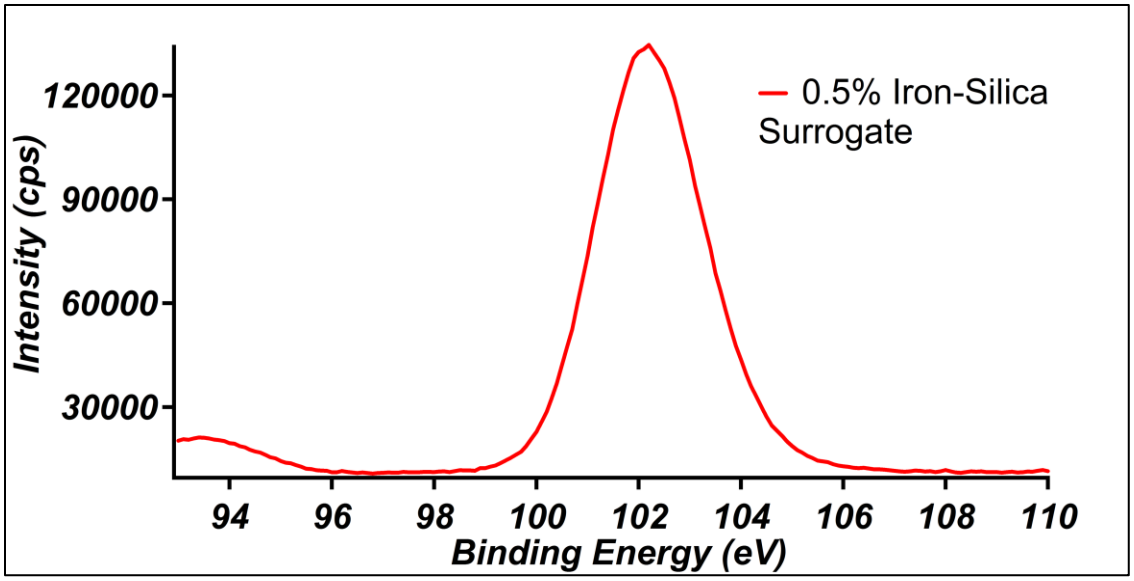

Figure 3.3. X-ray photoelectron spectrum of the silicon region in the 0.5% iron-silica PM surrogate.

Figure 3.4 shows two low intense peaks detected at ~708.5 and ~724.6 eV, which correlate to iron's $2p_{3/2}$ and $2p_{1/2}$ subshells, respectively (Wang et al., 2016). Due to the absence of satellite features from iron's 2p subshells, the iron oxidation state(s) could not be determined. Because silicon was observed in the X-ray photoelectron spectrum, surfaced silica could also affect the EPFR formation on the iron-silica PM surrogates. Also, the spectral interpretation of the reported peaks in the XPS data could correspond to other elements. An internal binding energy reference is not available to accurately calibrate the XPS (Greczynski et al., 2020).

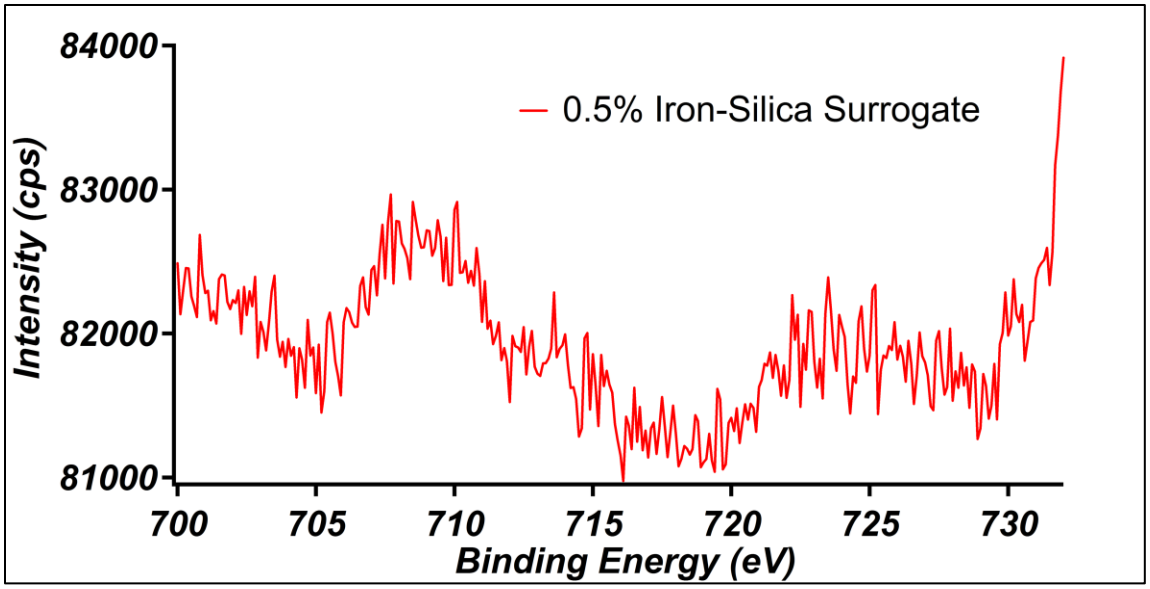

Figure 3.4. X-ray photoelectron spectrum of the iron region in the 0.5% iron-silica PM surrogate.

3.1.4. X-ray fluorescence spectroscopy studies of PM surrogates

XRF was conducted on the 3% iron-silica PM surrogates and silica to demonstrate the presence of higher iron concentrations in the PM surrogates. As shown in Figure 3.5, the counts per second (cps) for iron's K-alpha emission at about 6.5 keV in the 3% iron-silica PM surrogate was higher than the silica. The other elemental signals in Figure 3.5 are from the instrument's support used to hold the sample during the analysis. The signal intensities from the instrument's support were consistently below 150 cps. Therefore, any signals observed above 150 cps were considered present in the material (i.e., only iron).

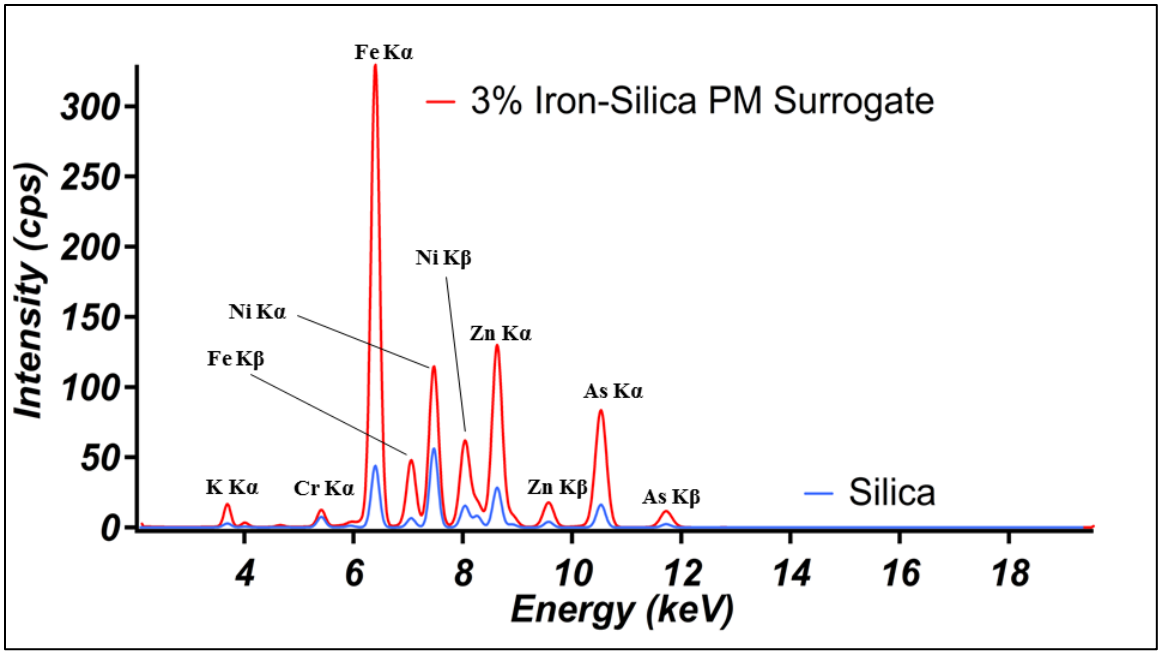

Figure 3.5. XRF spectra of silica and 3% iron-silica PM surrogate.

3.1.5. Transmission electron microscopy studies of PM surrogates

To examine the presence of electron diffraction patterns, TEM was utilized on the 0.5% and 3% iron-silica PM surrogates. As displayed in Image 3.1, silica (Panels A–B) and 0.5% iron-silica PM surrogates (Panels C–D) did not reveal any electron diffraction patterns. However, the 3% iron-silica PM surrogates shown in Image 3.2 did reveal electron diffraction patterns. It is important to note that the electron diffraction patterns reported for the 3% iron-silica PM surrogates was challenging to find by TEM. Not all areas of the 3% iron-silica PM surrogates exhibited electron diffraction patterns. The *d*-spacing of the electron diffraction patterns (Image 3.2) were measured to 0.225 nm (2.25 Å), which correlates to the *d*-spacing of ferrihydrites, also referred to as hydrous ferric oxyhydroxides (Jones, 1986). Also, the presence of ferrihydrites is further supported by the observed colors. Ferrihydrites are generally not as red as hematite and the iron-silica PM surrogates exhibited a reddish-tan color (Schwertmann et al., 1983). To conclude, small amounts of ferrihydrites could exist in the iron-silica PM surrogates. Since it was

not possible to obtain a chemical analysis of the detected electron diffraction pattern, it is possible the measured *d*-spacing could correspond to other materials.

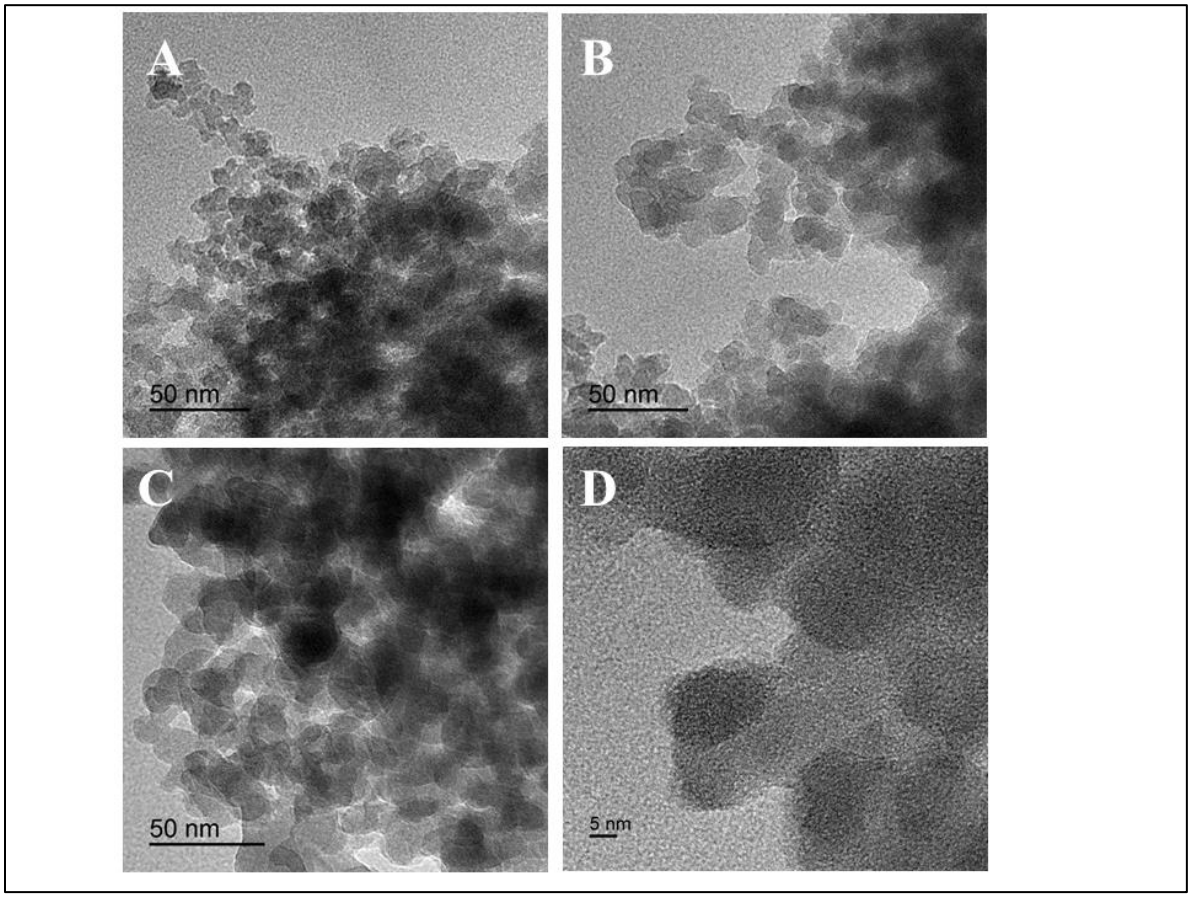

Image 3.1. TEM images of silica (A–B) and 0.5% iron-silica PM surrogate (C–D).

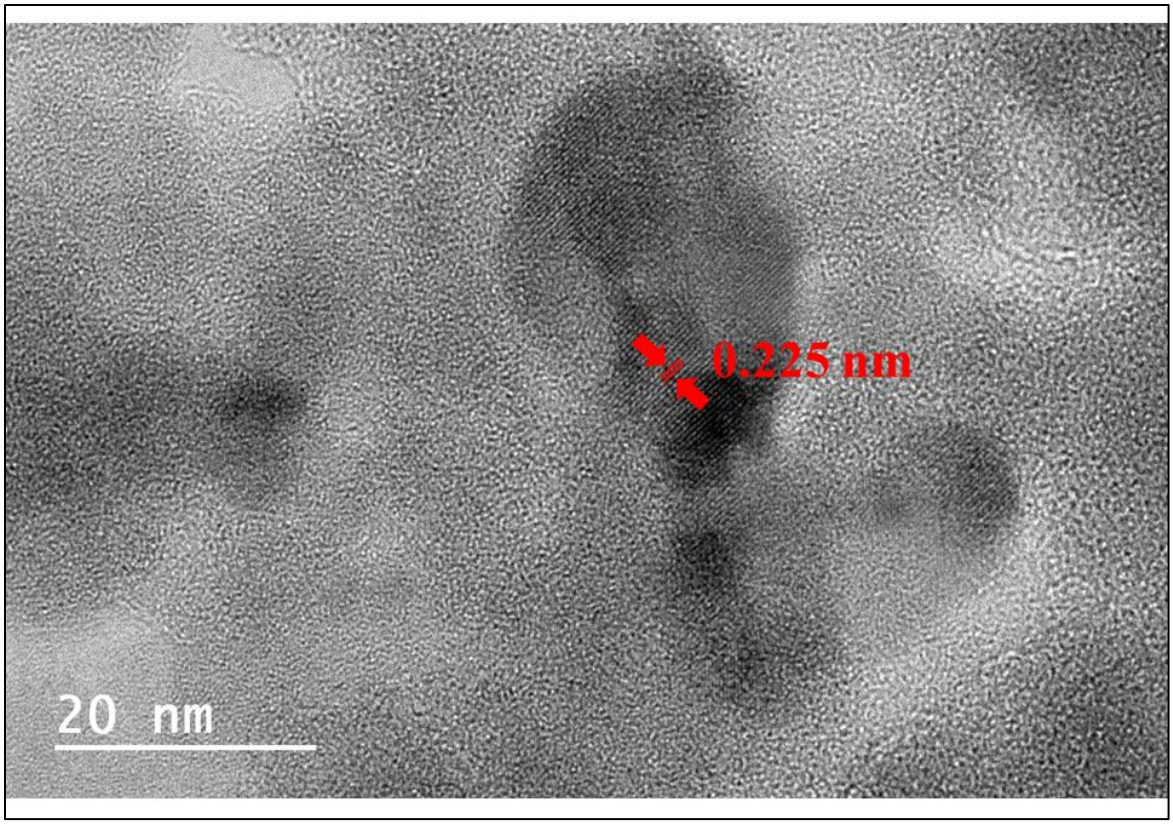

Image 3.2. TEM image of 3% iron-silica PM surrogate with measured lattice spacing.

3.1.6. Diffuse reflectance ultraviolet-visible/near-infrared spectroscopy studies of PM surrogates

Diffuse reflectance UV-vis/NIR spectroscopy was conducted on the 0.5% iron-silica surrogates to investigate the coordination environments of the material. Ferric (iron(III)) ions can exhibit different coordination environments depending on experimental conditions. The as-prepared 0.5% iron-silica surrogates were measured prior to any vacuum and thermal treatments. As displayed in Figure 3.6, UV-vis/NIR on the 0.5% iron-silica surrogates detected a strong absorption band around 260 nm. The absorption band around 260 nm is characteristic of a charge transfer from the ferric ions to the silicate framework in tetrahedral coordination environments. The silica, which was prepared the same way as the iron-silica PM surrogates, did not exhibit any significant absorption bands.

Other studies consistently reported bands around 220, 245, 260, and 200–333 nm (Bordiga et al., 1996; Lin et al., 1989; Tuel et al., 1998; Xin et al., 2008). Therefore, 0.5% iron-silica surrogates compose mostly of ferric ions covalently bonded to the silicate framework in tetrahedral coordination environments. The weakly intense and broad absorption band from 320–600 nm corresponds to isolated ferric ions in extra-framework sites or iron oxide nanoparticles (less than 4 nm in diameter) both exhibiting octahedral coordination environments (Amama et al., 2005; Bhaumik et al., 2005; Geinguenaud et al., 2015; Goldfarb et al., 1994; Lassoued et al., 2017).

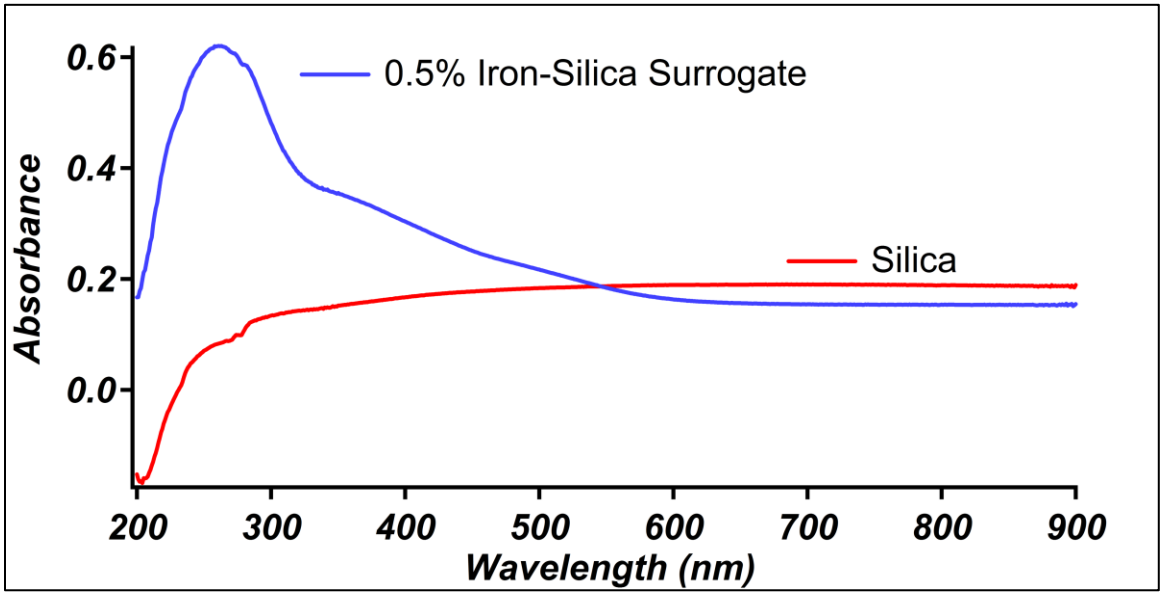

Figure 3.6. Diffuse reflectance UV-vis/NIR spectra on the silica (red curve) and 0.5% iron-silica PM surrogate (blue curve) measured under ambient conditions.

3.1.7 Thermogravimetric studies of PM surrogates

TGA was carried out on the 3% and 0.5% iron-silica PM surrogates to examine mass loss that could be caused by dehydration, decomposition, or oxidation. As shown in Figure 3.7, the loss of water occurred between the temperatures of 27 °C and 120 °C in all PM surrogates and silica. The mass loss was about 3% of the total weight.

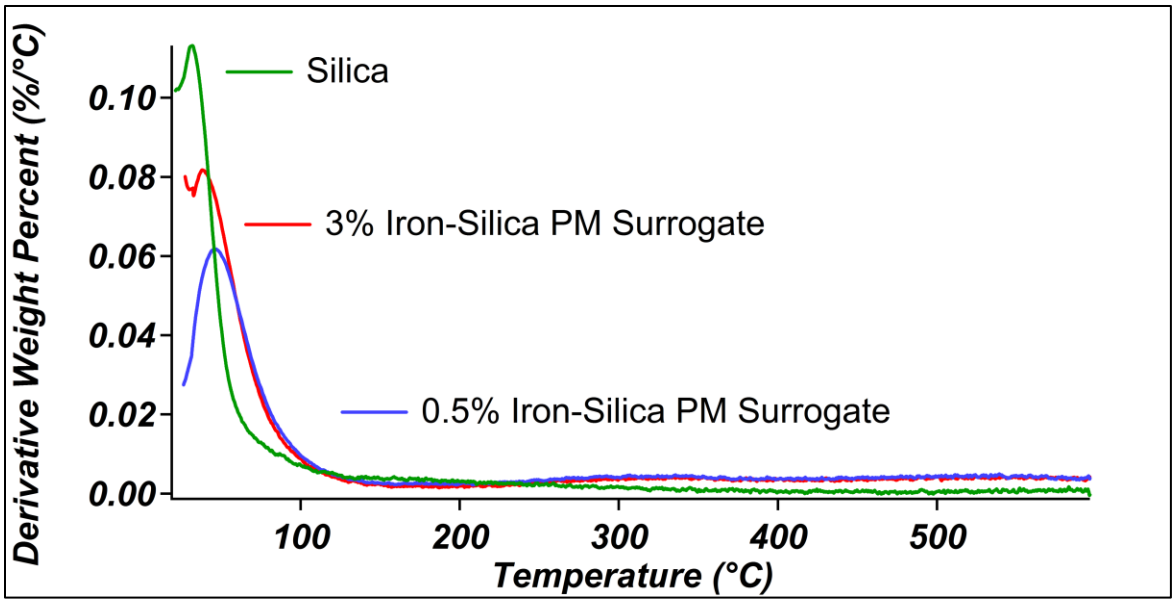

Figure 3.7. Thermogravimetric analysis of silica (green curve), 3% (red curve) and 0.5% (blue curve) iron-silica PM surrogates.

3.2. Characterization of ambient $PM_{2.5}$

3.2.1. Scanning electron microscopy studies of ambient $PM_{2.5}$

SEM was conducted on ambient $PM_{2.5}$ to reveal the particle sizes. As shown in Image 3.3, the web-like material is from the PTFE filter and center of the images are small aggregated particles of ambient $PM_{2.5}$, measuring less than 2 μm in diameter, can be seen. In the PM surrogates aggregation was also observed (Image 3.1). An average particle size was found to be ~ .309 μm out of twelve measurements. However, it was difficult to take measurements of the particle sizes due to irregular shapes, aggregation behavior, and charging effects on the quality of the image.

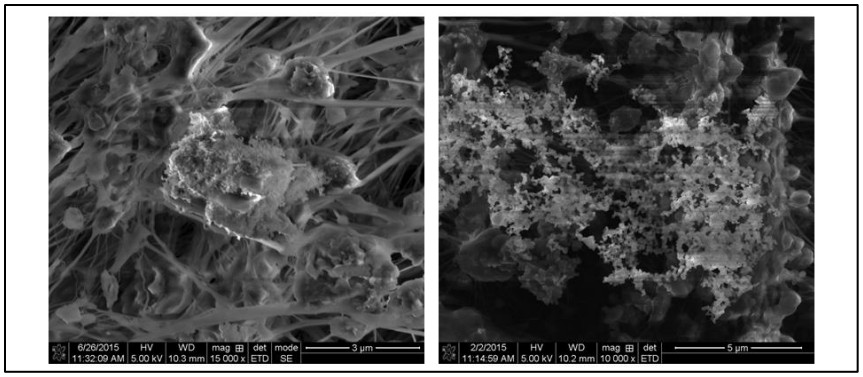

Image 3.3. SEM images of ambient $PM_{2.5}$ collected on a PTFE filter (Sample ID P2920556).

3.2.2 X-ray diffraction studies of ambient $PM_{2.5}$

XRD was conducted on ambient $PM_{2.5}$ to determine the phase of iron present. As shown in Figure 3.8, the detected Bragg peaks at about 33°, 36°, 49°, 53°, 57°, and 66° are characteristic of the XRD pattern for hematite (Alcalá et al., 2006; Bourlinos et al., 2001; Li et al., 2016; Palomares-Sánchez et al., 2002; Yi et al., 2019).

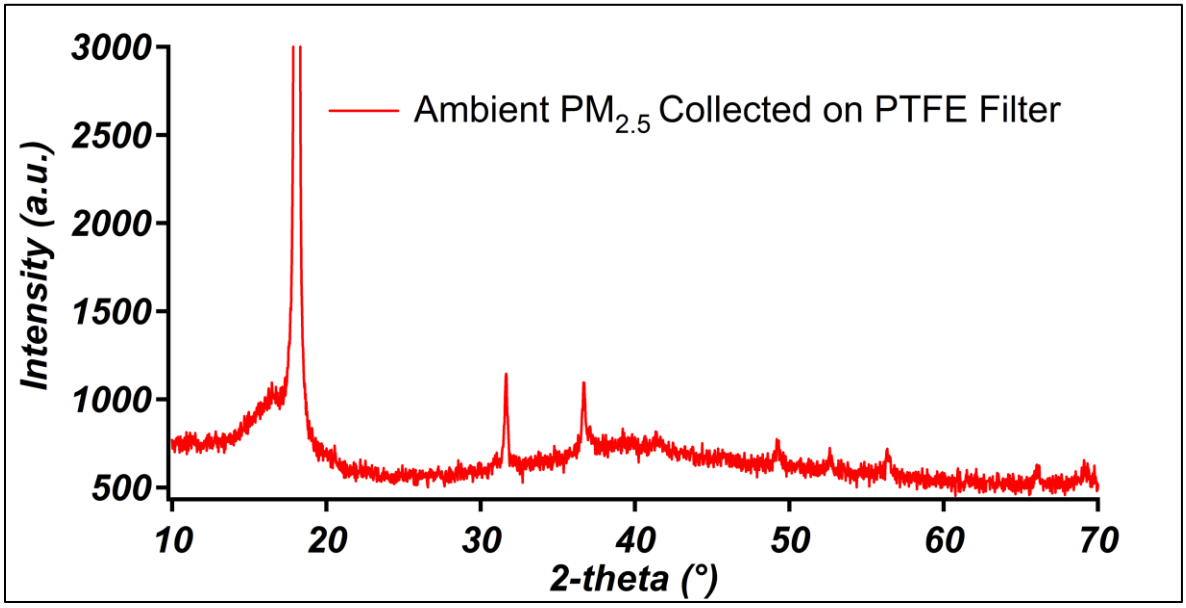

Figure 3.8. XRD spectrum of ambient $PM_{2.5}$ collected on PTFE filter (Sample ID P2916126).

Using the Scherrer equation the calculated particle diameter of hematite was 0.379 μm, which is less than 2.5 μm for $PM_{2.5}$. The crystallinity (identified by the sharp and more intense peaks) in ambient $PM_{2.5}$ is higher in comparison with the PM surrogate (see Section 3.1.2).

However, both ambient $PM_{2.5}$ and the PM surrogates are heterogeneous so crystallinity will vary in each sample.

3.2.3 X-ray photoelectron spectroscopy studies of ambient $PM_{2.5}$

XPS was conducted to detect the presence of iron on the particle surfaces of ambient $PM_{2.5}$. A XPS survey spectrum shown in Figure 3.9 did not discover any metals in significant amounts.

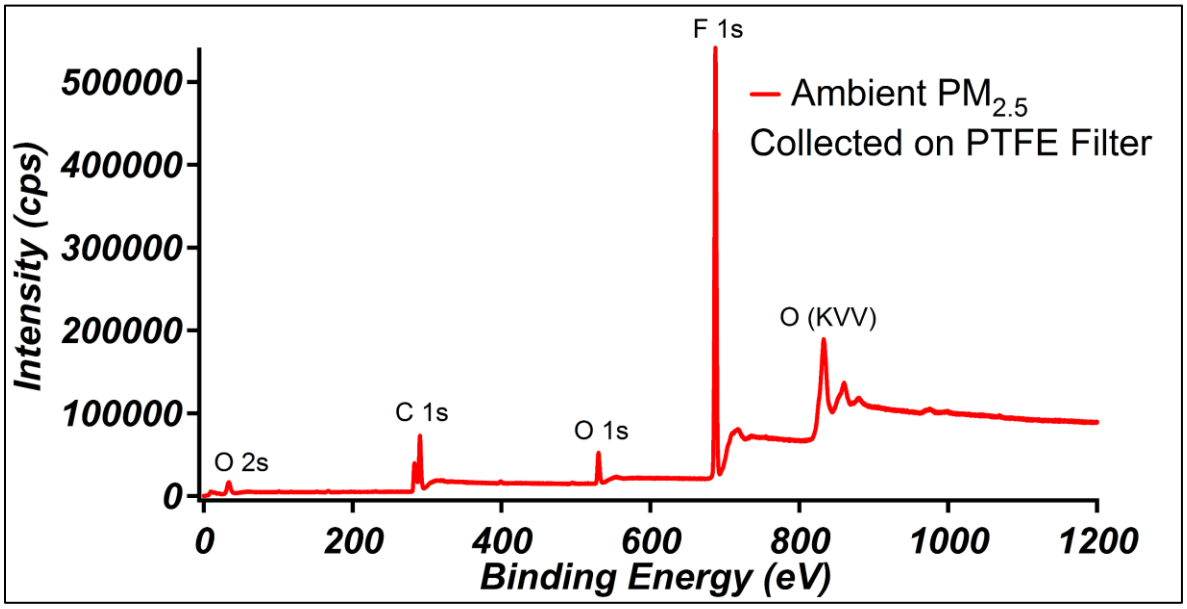

Figure 3.9. X-ray photoelectron spectrum (survey scan) of ambient $PM_{2.5}$ collected on PTFE filter (Sample ID P2920556).

The iron and silicon 2p shells were determined to have a mass concentration of 9.42% and 0.65%, respectively. A high resolution XPS scan spectrum on the iron region detected two peaks (Figure 3.10) at 711.0 and 719.8 eV, which correlate to iron's $2p_{3/2}$ and $2p_{1/2}$ subshells, respectively (Wang et al., 2016). Also, the spectral interpretation of the reported peaks in the XPS data could correspond to other elements. As it was discussed in Section 3.1.3, an internal binding energy reference is not available to accurately calibrate the XPS (Greczynski et al., 2020).

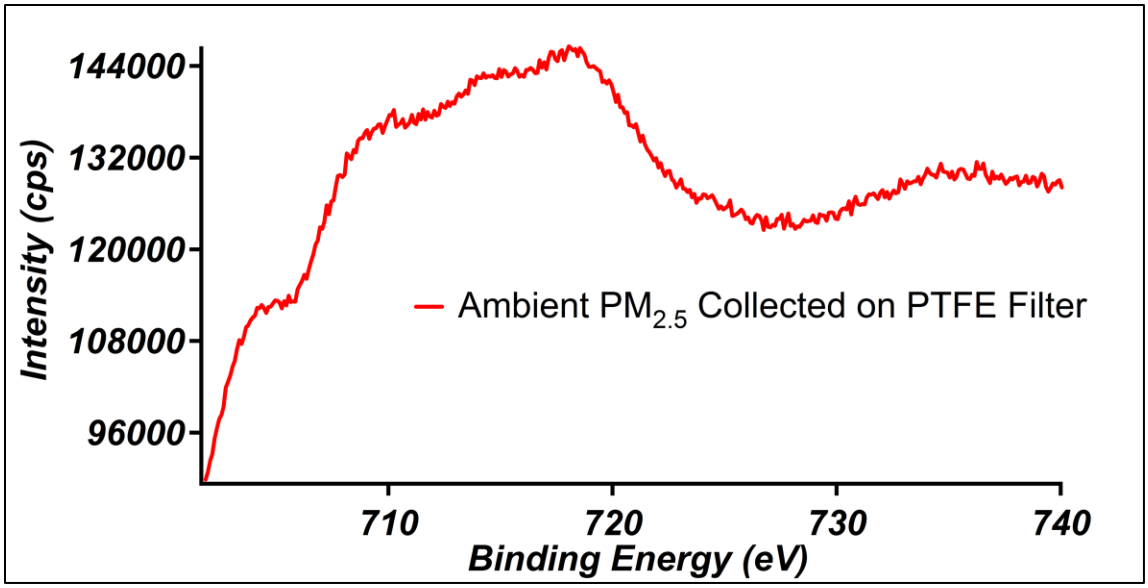

Figure 3.10. X-ray photoelectron spectrum of the iron region for ambient $PM_{2.5}$ collected on PTFE filter (Sample ID P2920556).

3.2.4 X-ray fluorescence spectroscopy studies of ambient $PM_{2.5}$

XRF was conducted to examine if iron and other metals were present in ambient $PM_{2.5}$. The filter number (i.e. P number) was used to label the various samples measured by XRF (Figure 3.11). As displayed in Figure 3.11A, the XPS spectra of the clean PTFE filters identified elemental signal intensities below 150 cps. These signals come from the instrument's support used to hold the sample during the analysis. Any elemental signal intensities above 150 cps were considered present in the material. In Figure 3.11B, elemental signal intensities above 150 cps were detected in ambient $PM_{2.5}$ collected on PTFE filters. Various elemental signal intensities were observed among the different samples. For example, zinc's K-alpha emission at about 8.6 keV for sample P2919718 (yellow curve in Figure 3.11B) was significantly above 150 cps, but then low in all other samples. However, the intensity of iron's K-alpha emission at about 6.5 keV was above 150 cps in all ambient $PM_{2.5}$ samples. To conclude, iron was consistently detected in ambient $PM_{2.5}$ and so the best metal to use in the PM surrogates.

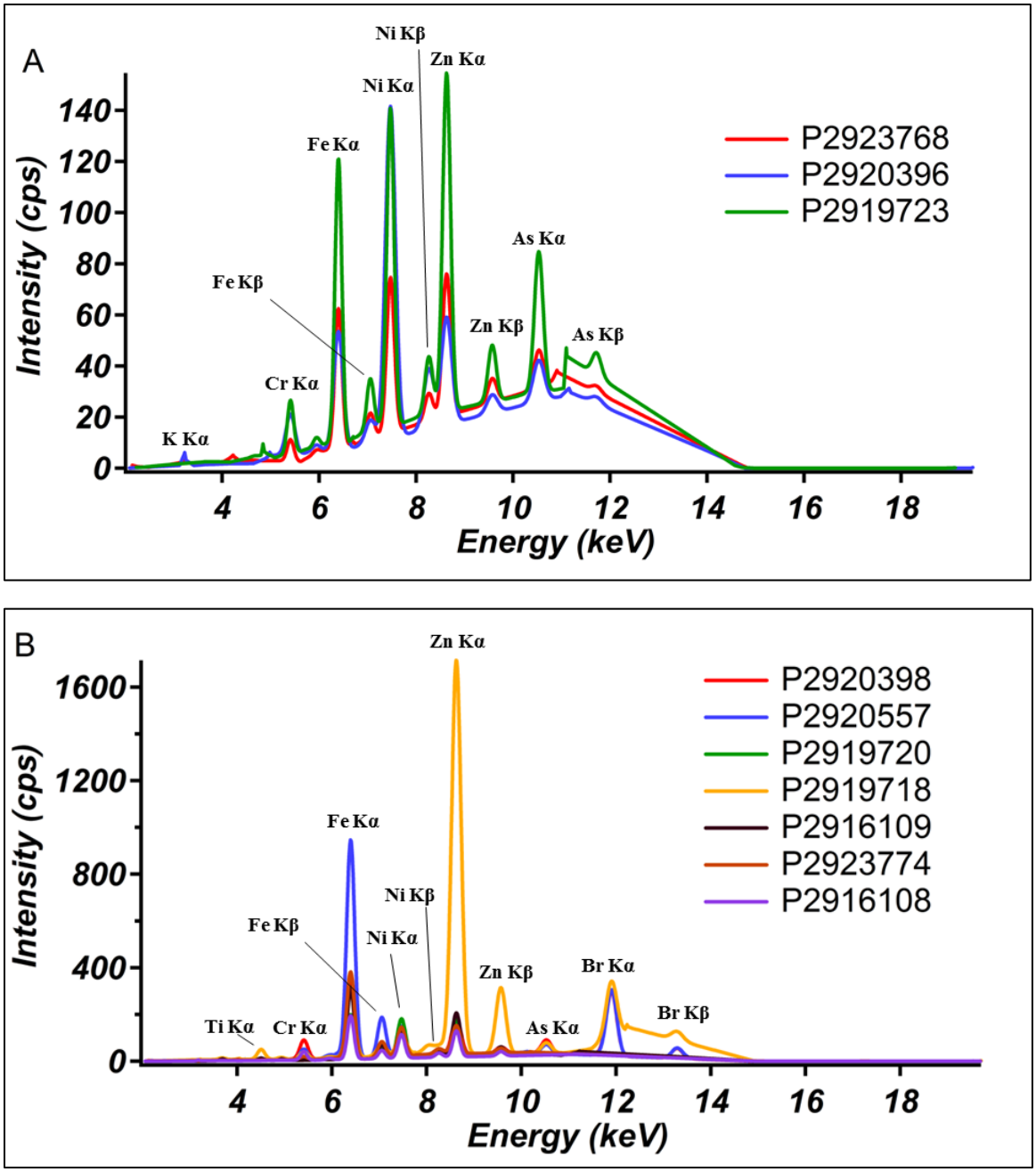

Figure 3.11. XRF spectra; (A, top) clean PTFE filters exposed to ambient conditions and (B, bottom) ambient $PM_{2.5}$ collected on different PTFE filters.

CHAPTER 4. IRON COORDINATION IN PM SURROGATES AND AMBIENT $PM_{2.5}$

Using EPR spectroscopy, previous studies have demonstrated that iron-silica materials yield EPR signals with *g*-factor values of 4.270 and 2.141 (broad) that correspond to ferric ions in distorted and undistorted tetrahedral coordination environments (or isolated ferric ions in extra-frameworks or iron oxide nanoparticles in octahedral environments), respectively. No previous studies on EPFR formation in iron-silica materials made reference to these coordination environments (Vejerano et al., 2011). The purpose of this chapter was to examine the effects of thermal and vacuum treatment on the EPR signals in PM surrogates and compare their behavior with EPR signals detected in ambient $PM_{2.5}$.

4.1. Iron coordination in PM surrogates

Heat (T = 450 °C) and vacuum (P = 0.1–0.01 Torr) treatment is conducted prior to exposing the PM surrogate to a precursor organic compound. This is a consistent procedural step described in the EPFR formation experiments (Kiruri et al., 2014; Vejerano et al., 2011). The heat (T = 450 °C) and vacuum (P = 0.1–0.01 Torr) treatment on the iron-silica PM surrogates helps remove water and expose the particle surfaces that are needed for EPFR formation. As shown by thermogravimetric analysis (Figure 3.7) loss of water occurs between the temperatures of 27 °C and 120 °C. By EPR, Lin and coworkers identified that after applying a heat treatment the intensity of the broad g = 2.141 EPR signal decreased and the intensity of the g = 4.270 EPR signal increased (Lin et al., 1989). As depicted in Figure 4.1A, those same observations were seen when heat (T = 450 °C) and vacuum (P = 0.1–0.01 Torr) treatment was applied for 1 h to the 0.5% iron-silica PM surrogate. The detected g = 4.270 ± 0.030 and broad g = 2.141 ± 0.100 EPR signals have peak to peak ($\Delta H_{p\text{-}p}$ = differences between maximum points of peaks with x-axis in Gauss) values of 98 ± 38-G and 1251 ± 80-G, respectively. These experiments were

reproducible six times. The silica control experiments (silica prepared without the iron(III) nitrate nonahydrate) did not yield any EPR signals as demonstrated in Figure 4.1B. Therefore, confirming the observed g = 4.270 and broad g = 2.141 EPR signals are attributed to the addition of the iron. However, a small intense EPR signal at g = 2.003 was observed in the PM surrogates and silica control samples, as indicated in Figure 4.2. Though it is unclear what exactly the signal is, it is suggested to be adventitious carbon (see Section 5.4 for more supporting information) (Castle, 2008; deVries et al., 1994; Piao et al., 2002). As it was revealed earlier by the TOC analysis (see Section 3.1.1) carbon was present in both silica and PM surrogates. The iron-containing PM surrogates (Figure 4.2A) exhibited a higher EPR signal intensity at g = 2.003 than silica (Figure 4.2B) because carbon was more abundant in iron-containing PM surrogates. Other possible explanations for the small intense EPR signal at g = 2.003 could be a result of contamination, superparamagnetic nanoparticles, water, or humidity effects.

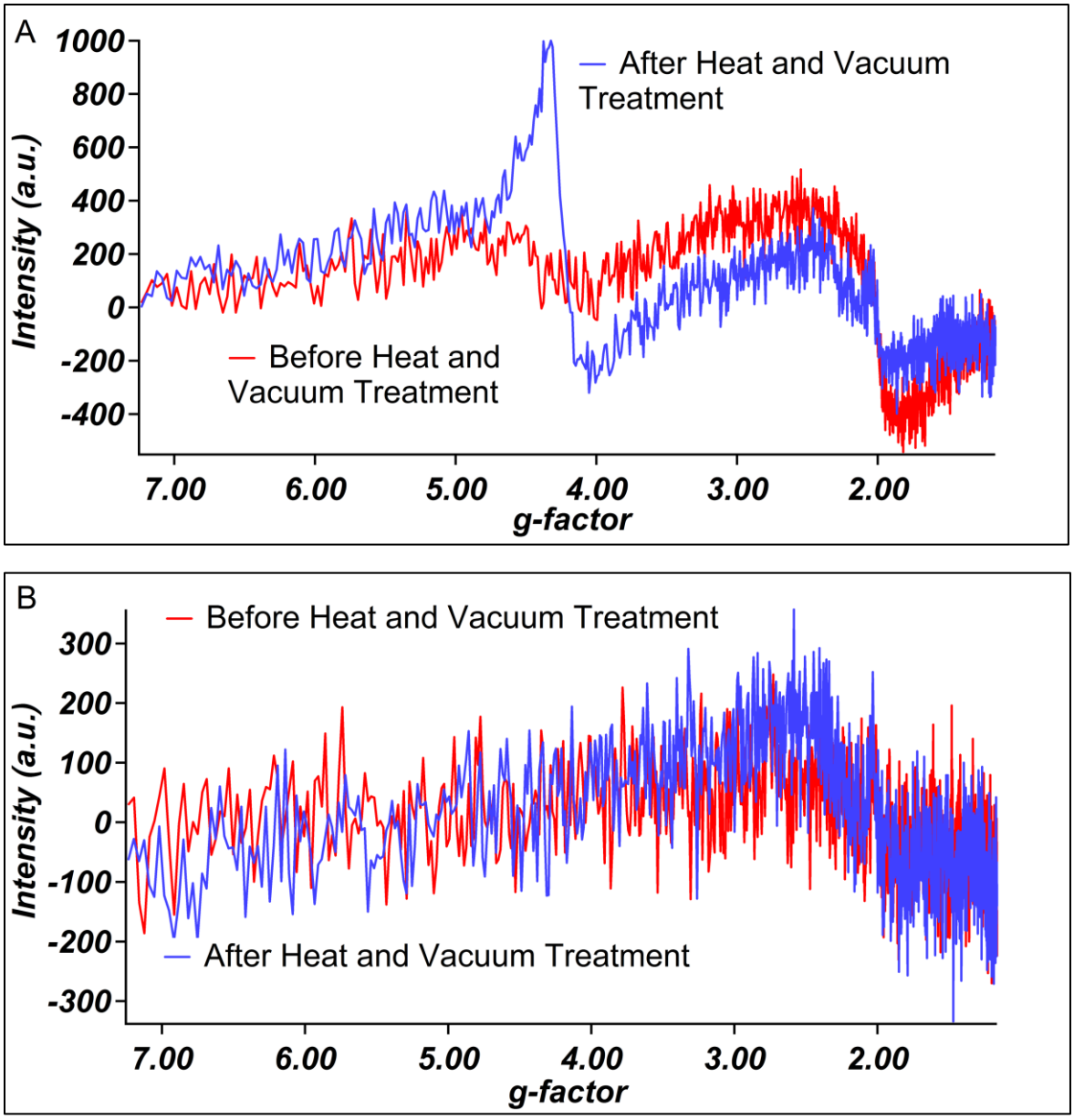

Figure 4.1. 5000-G scans derivative-of-absorption EPR spectra before (red curve) and after heat and vacuum treatment (blue curve) measured under vacuum; (A, top) 0.5% iron-silica PM surrogate and (B, bottom) silica.

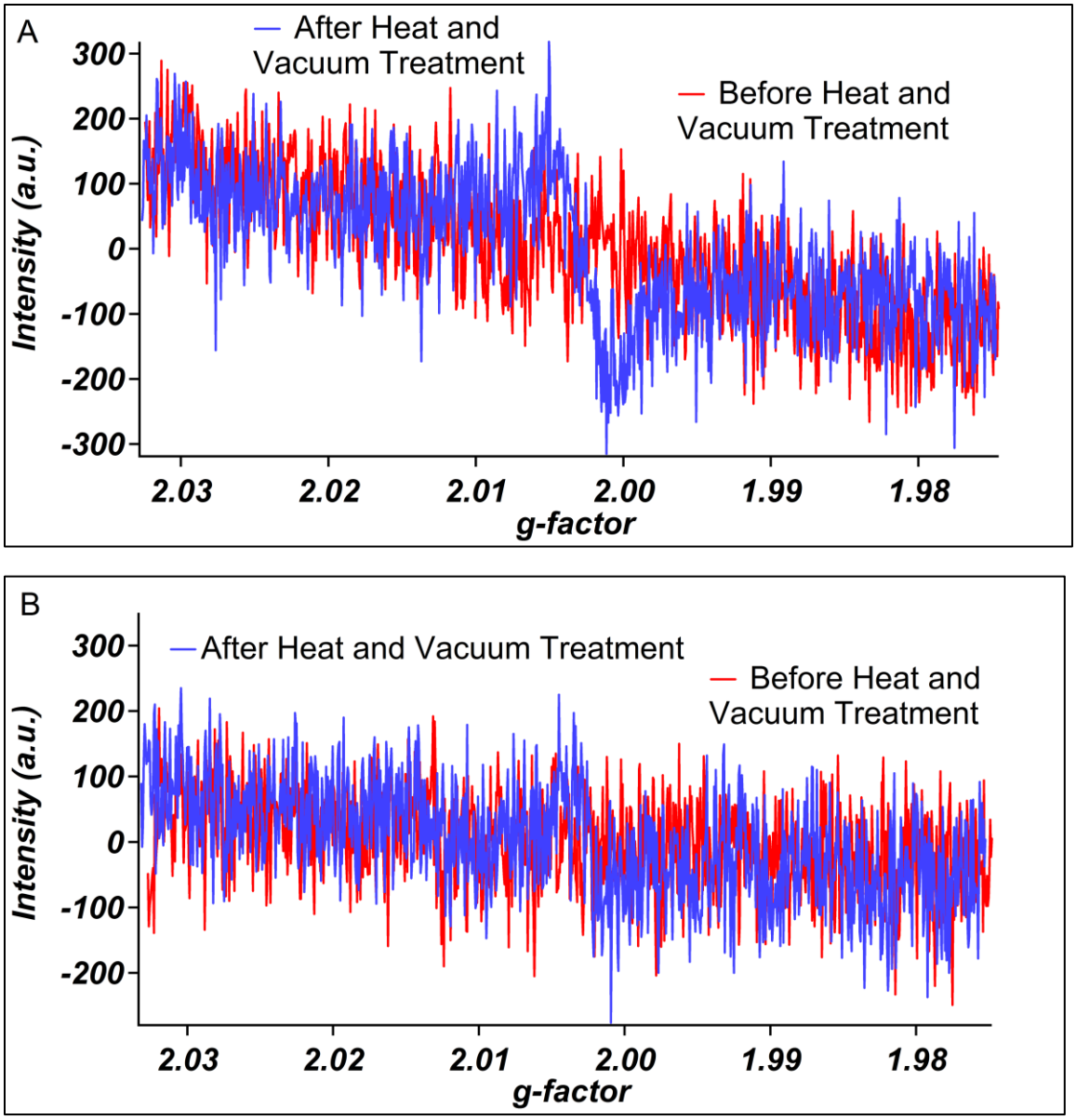

Figure 4.2. 100-G scans derivative-of-absorption EPR spectra before (red curve) and after heat and vacuum treatment (blue curve) measured under vacuum; (A, top) 0.5% iron-silica PM surrogate and (B, bottom) silica.

4.1.1. Brønsted acid sites within framework in PM surrogates

Next, the thermally/vacuum treated 0.5% iron-silica surrogate was then exposed to ambient atmosphere causing atmospheric water to saturate the surrogate and decrease the g = 4.270 EPR signal intensity, as shown in Figure 4.3A. The intensity changes observed at g = 4.270 EPR signal indicate the presence of Brønsted acid sites because the g = 4.270 signal

increased after being thermally/vacuum treated and then decreased upon exposure to ambient atmosphere for the 0.5% iron-silica surrogate (Bordiga et al., 1996). These Brønsted acid sites appear when water is removed because the hydronium ions (H_3O^+) in water donate protons to oxygen atoms associated with the iron atoms. Thus, causing ferric ions in octahedral or undistorted tetrahedral coordination environments to shift to distorted tetrahedral coordination environments (see Scheme 1.6) (Bordiga et al., 1996; Tuel et al., 1998). Therefore, the g = 4.270 EPR signal corresponds to ferric ions in distorted tetrahedral coordination environments from protonated bridged oxygen atoms (Brønsted acid sites) either between the silicon atoms of the silica and iron atoms or between different iron atoms (Berlier et al., 2002; Bordiga et al., 1996; Tuel et al., 1998). The broad, g = 2.141 EPR signal (Figure 4.3A) corresponds to ferric ions in undistorted tetrahedral coordination environments from ferric ions covalently bounded by either oxygen atoms of the silica framework or oxygen atoms between other iron atoms. It could also correspond to isolated ferric ions in extra-framework sites (octahedral coordination) or iron oxide nanoparticles less than 4 nm in diameter (octahedral coordination) (Berlier et al., 2002; Bordiga et al., 1996; Cannas et al., 1998; Geinguenaud et al., 2015; Lassoued et al., 2017; Tuel et al., 1998). The presence of Brønsted acid sites is further supported by previous ammonia experiments. Ammonia also consists of positive charges (NH_4^+) like water (H_3O^+). According to the literature, adsorption of ammonia to similar iron-silica materials also demonstrated undistorted/octahedral and distorted tetrahedral coordination environments and their reversibility through other techniques, such as UV-Vis/NIR and Mössbauer spectroscopy (Bordiga et al., 1996; Tuel et al., 1998).

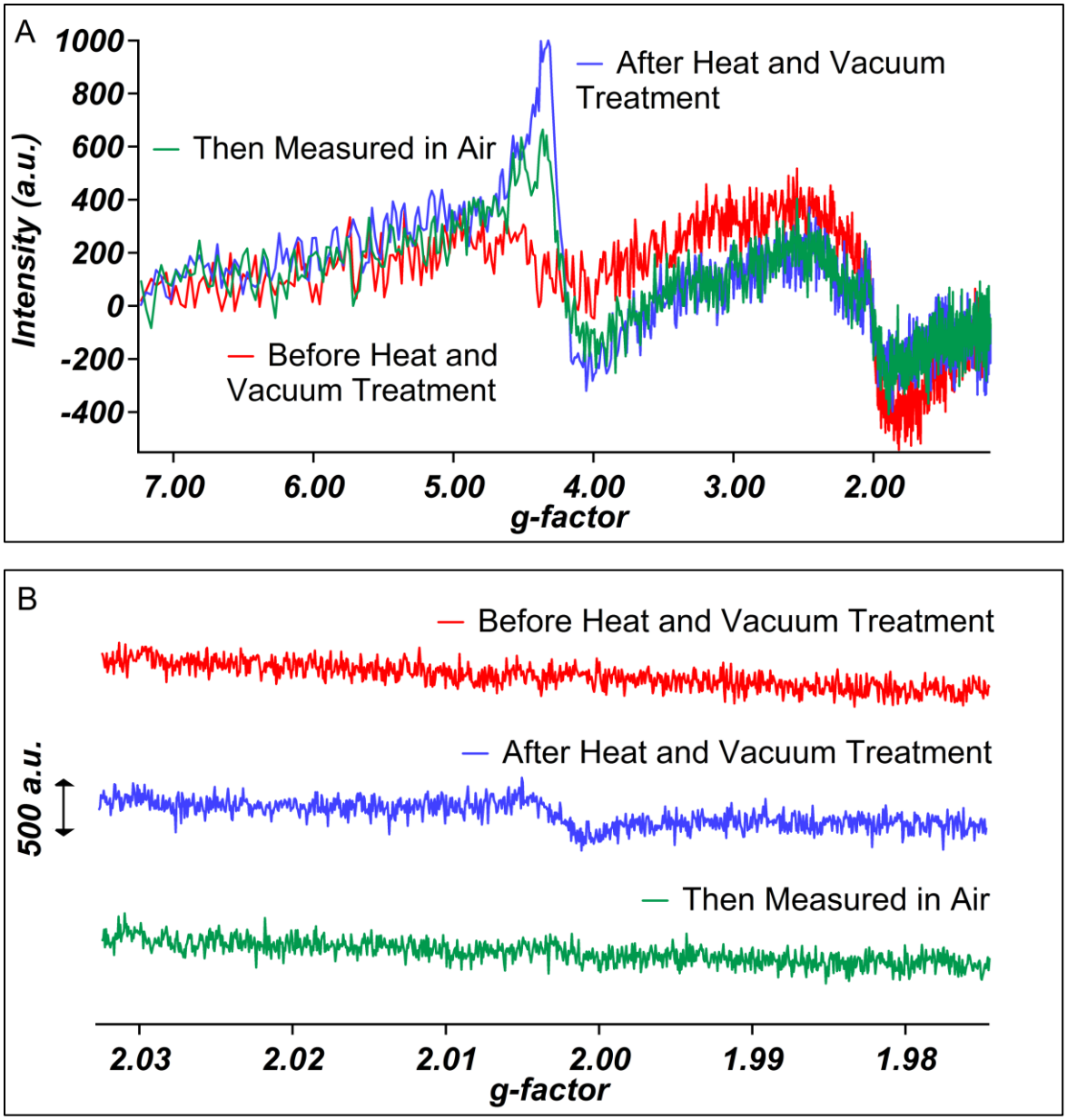

Figure 4.3. Derivative-of-absorption EPR spectra of 0.5% iron-silica PM surrogate before (red curve), after heat and vacuum treatment (blue curve) measured under vacuum, and then measured in air (green curve); (A, top) 5000-G scans and (B, bottom) 100-G scans.

Evaluation of the 0.5% iron-silica PM surrogates by FT-IR could provide evidence for the existence of Brønsted acid sites. Usually, Brønsted acid sites and hydrogen-bonded silanols (R-Si-OH) yield a 3620 cm^{-1} band and 3414 cm^{-1} band, respectively (Bordiga et al., 1996; Goldfarb et al., 1994). Figure 4.4 (red curve) revealed the signal-to-noise ratio was not sufficient to observe the 3620 cm^{-1} band for Brønsted acid sites. However, it should be noted the 3414

cm^{-1} band was detected (Figure 4.4, red curve) and decreased (Figure 4.4, blue curve) upon heat (T = 450 °C) and vacuum (P = 0.1–0.01 Torr) treatment for 1 h. Thus, demonstrating the hydrogen-bonded silanols (R-Si-OH) were dehydroxylated to siloxanes (R-Si-O-Si-R) after treatment.

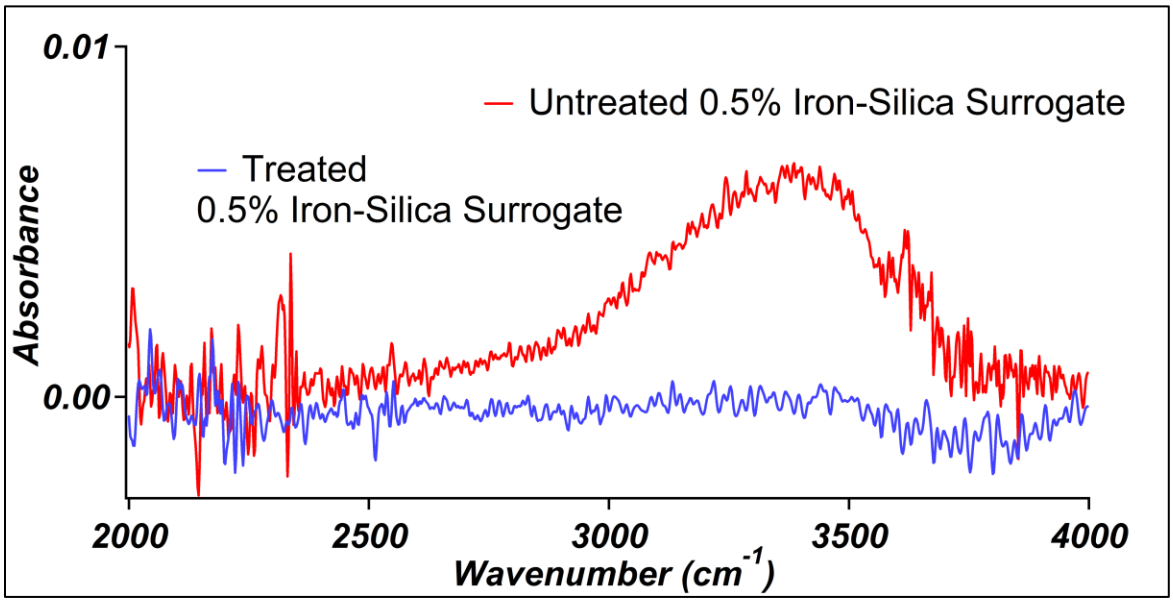

Figure 4.4. FT-IR spectra of 0.5% iron-silica PM surrogate before (red curve) and after heat and vacuum treatment (blue curve) measured at ambient conditions.

Additionally, when the broad g = 2.141 EPR signals of the 0.5% and 3% iron-silica PM surrogates were compared at ambient conditions, the signal intensity for 3% was higher than 0.5% as shown in Figure 4.5. This suggests the higher iron concentrations increased the number of ferric ions in undistorted tetrahedral or octahedral coordination environments. These findings are consistent with previous studies (Amama et al., 2005; Goldfarb et al., 1994). As for the intensity of the g = 4.270 EPR signal, it appears unaffected (Figure 4.5) by the higher iron concentrations at ambient conditions. Amana and coworkers reported a decrease in intensity for the g = 4.270 EPR signal with higher iron concentrations (Amama et al., 2005). The differences are likely due to the timing of when the measurement was taken after preparing the iron-silica materials, preparation techniques, or measuring conditions. Furthermore, the ferric ions in

distorted tetrahedral coordination environments yielding the g = 4.270 EPR signal will decrease depending on the amount of time it takes for atmospheric water to adsorbed on the iron-silica PM surrogate as it was shown in Figure 4.3A.

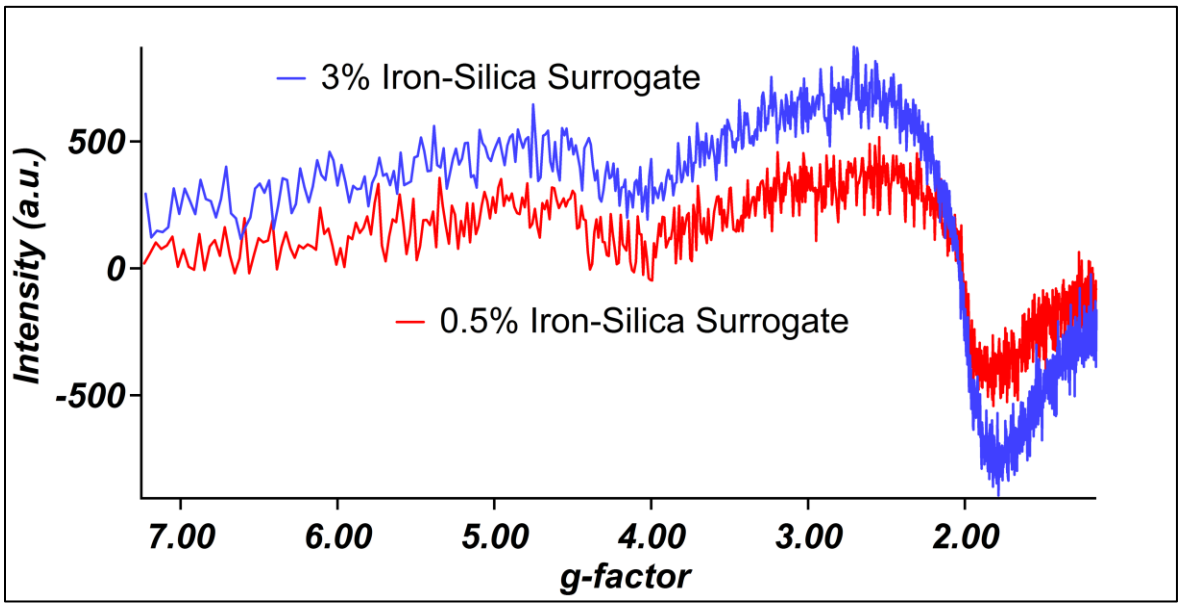

Figure 4.5. 5000-G scans derivative-of-absorption EPR spectra of 0.5% (red curve) and 3% (blue curve) iron-silica PM surrogates measured at ambient conditions.

4.2. Iron coordination in ambient $PM_{2.5}$

The observed changes of the EPR signals in the 0.5% iron-silica PM surrogates were compared to ambient $PM_{2.5}$. Unfortunately, the heat treatment at 450 °C needed to observe intensity changes of the g = 4.270 and broad g = 2.141 EPR signals for the 0.5% iron oxide-silica PM surrogates could not be accomplished with the ambient $PM_{2.5}$ supported on poly(tetrafluoroethylene) (PTFE) filters. This is because the melting point of the PTFE is 327 °C, it would have melted if heated to 450 °C. Nonetheless, a broad EPR signal as presented in Figure 4.6 was consistently observed at g = 2.128 ± 0.100 ($\Delta H_{p\text{-}p}$ = 70 ± 10-G) in all ambient $PM_{2.5}$ collected on different PTFE filters.

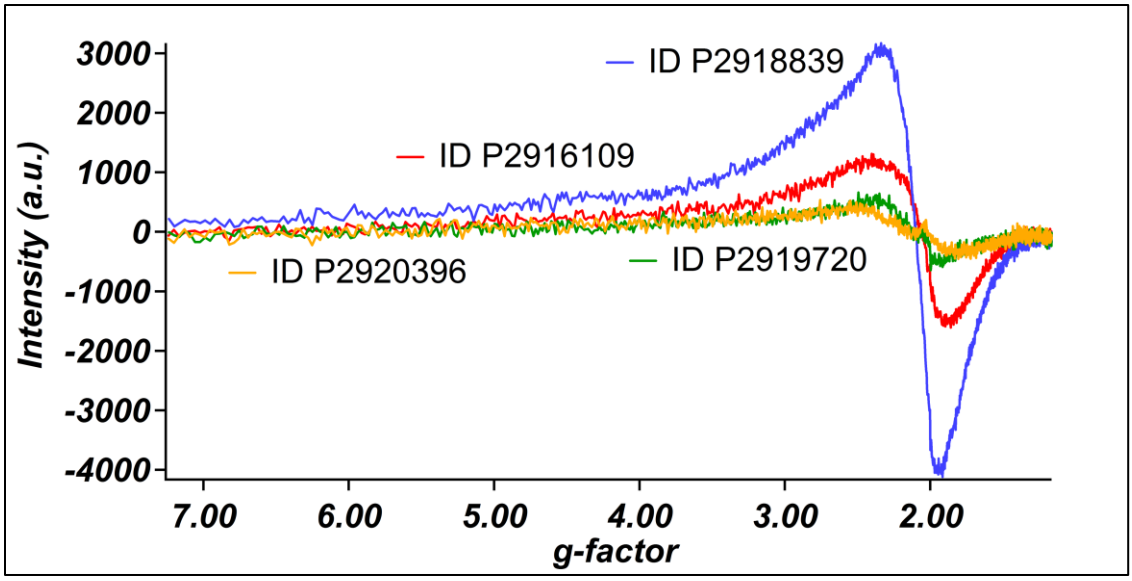

Figure 4.6. 5000-G scans derivative-of-absorption EPR spectra of $PM_{2.5}$ collected on different PTFE filters.

To ensure that these signals were not from the filters, a clean PTFE filter was measured and showed no signals, as demonstrated in Figure 4.7.

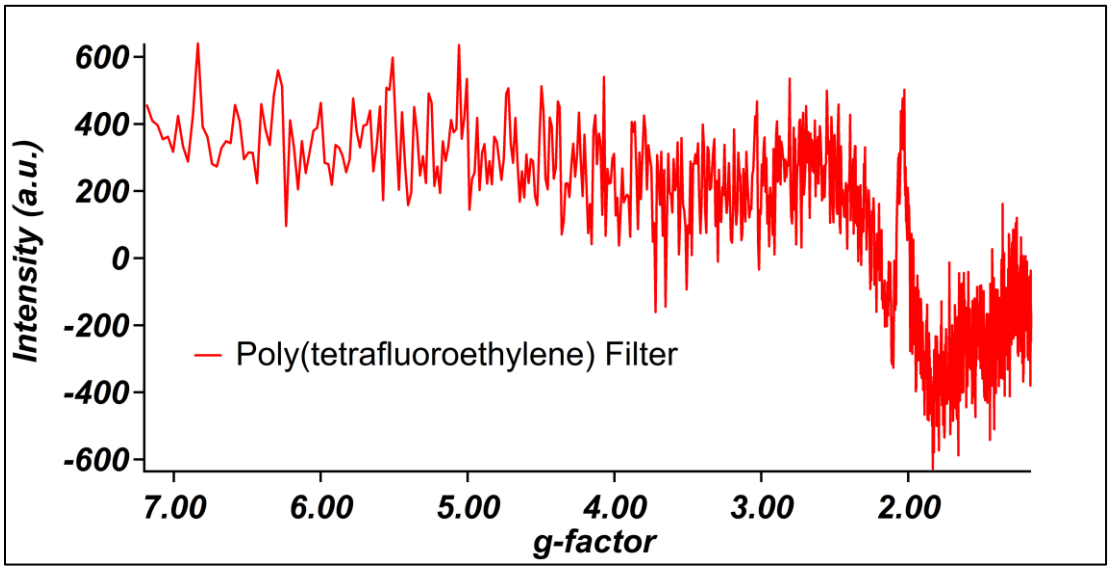

Figure 4.7. 5000-G scan derivative-of-absorption EPR spectrum of a PTFE filter. This scan is consistent with the background of the empty EPR cavity.

The g = 2.128 EPR signal observed in ambient $PM_{2.5}$ does not appear to correspond to ferric ions in undistorted tetrahedral or octahedral coordination environments that were observed in PM surrogates at broad g = 2.141 for two reasons. First, the g = 4.270 EPR signal (distorted

tetrahedral coordination) was not observed. Second, the intensity of the g = 2.128 EPR signal of the ambient $PM_{2.5}$ samples increased upon heat treatment to 120 °C for 1 h, unlike the broad g = 2.141 EPR signal behavior in PM surrogates, as shown in Figure 4.8 for both $PM_{2.5}$ samples. Thus, with support from literature, it is proposed that particle aggregation between iron and other paramagnetic species yield the g = 2.128 EPR signal (Herring, 2013; Ledoux et al., 2002; Ledoux et al., 2004). SEM images (Image 3.3) of ambient $PM_{2.5}$ collected on PTFE filter demonstrated particle aggregation. The increased intensity in the g = 2.128 EPR signal is due to the removal of adsorbed water.

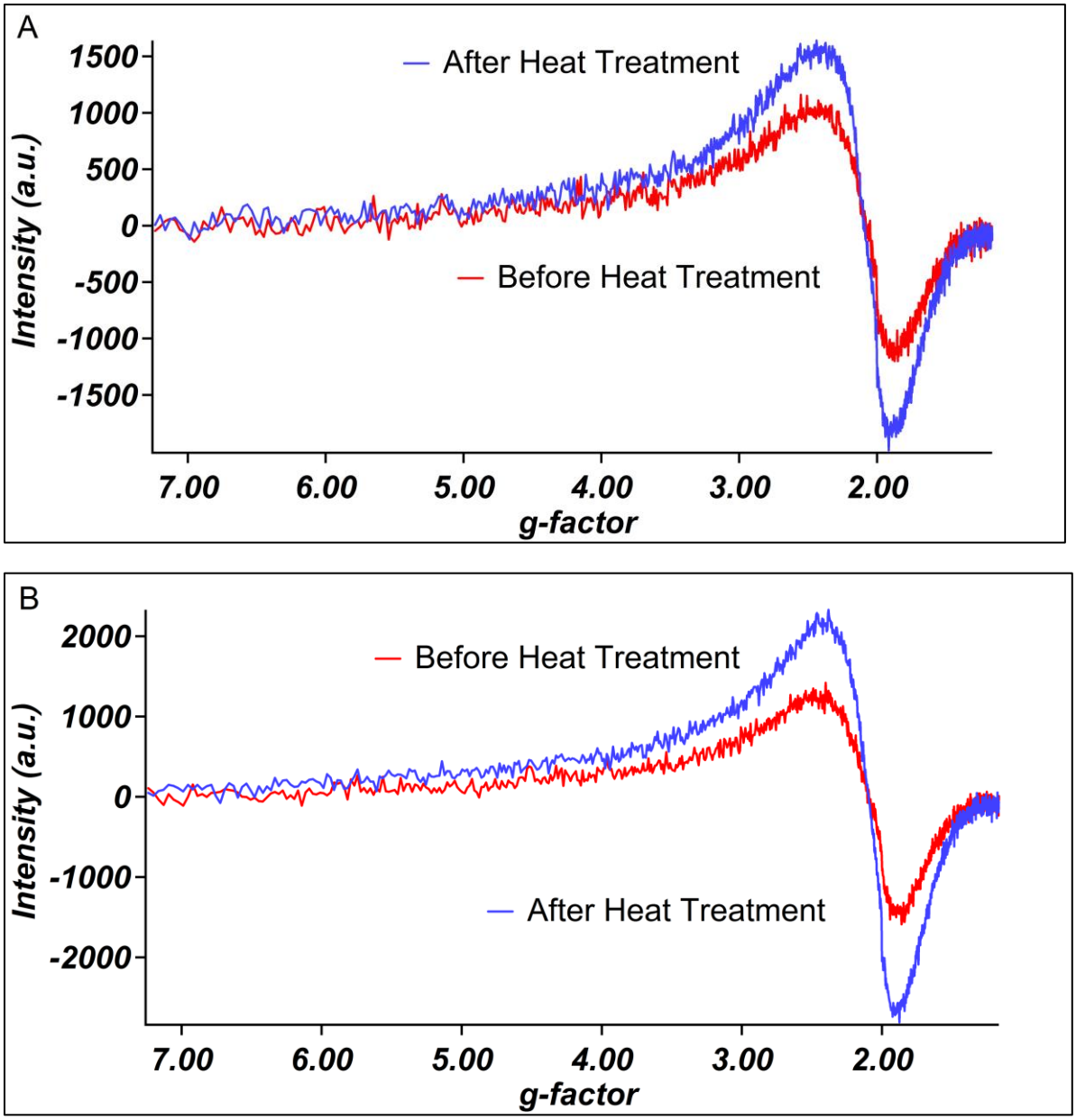

Figure 4.8. 5000-G scans derivative-of-absorption EPR spectra of ambient $PM_{2.5}$ before (red curve) and after 120 °C treatment for 1 h in ambient atmosphere (blue curve) measured at ambient conditions; (A, top) ambient $PM_{2.5}$ collected on PTFE filter (Sample ID P2923773) and (B, bottom) ambient $PM_{2.5}$ collected on PTFE filter (Sample ID P2920557).

CHAPTER 5. ISOLATED FERRIC IONS IN PM SURROGATES AND AMBIENT $PM_{2.5}$

In addition to the previously identified EPR signals in PM surrogates, other observed EPR signals with *g*-factor values of 2.300 and 2.003 (narrow EPR signal shapes) were examined. The objective of this chapter was to rationalize a possible explanation for the nature of the narrow $g = 2.003$ EPR signal in the PM surrogates. Heat/vacuum cycled treatment on the PM surrogate can yield a narrow $g = 2.003$ EPR signal. The data strongly supports ferric iron associated with superparamagnetic nanoparticles yielded a narrow $g = 2.003$ EPR signal. However, the occurrence of the narrow $g = 2.003$ EPR signal could be a result of contamination, adventitious carbon, water, or humidity effects. Results were compared to EPR signals found in ambient $PM_{2.5}$.

5.1. Iron aggregates in PM surrogates

As noted in Section 3.1.6, diffuse reflectance UV-Vis/NIR (Figure 3.6) detected isolated ferric ions in extra-framework sites or iron oxide nanoparticles less than 4 nm in diameter both exhibiting ferric ions in octahedral coordination environments in the 0.5% iron-silica PM surrogates (Amama et al., 2005; Bhaumik et al., 2005; Geinguenaud et al., 2015; Goldfarb et al., 1994; Lassoued et al., 2017). A previous study's diffuse reflectance UV-Vis/NIR data on 2% and 3% iron-silica materials agreed with the 0.5% iron-silica PM surrogates diffuse reflectance UV-Vis/NIR data (Amama et al., 2005). However, the previous study reported ferric ions in octahedral coordination environments in 2 and 3% iron concentrations but not in the 1% iron concentration materials. One must carefully consider differences in sample preparation and treatment. One notable difference in sample preparation from Amama and coworkers was an anti-foaming agent used to prepare the catalyst which was not used in this work to prepare the 0.5% iron-silica PM surrogates (Amama et al., 2005).

Investigations on the 3% iron-silica PM surrogates were conducted in addition to the 0.5% iron-silica PM surrogates. It was found higher concentrations of iron can cause a saturation of the surface coordination sites of the silica; therefore, reducing the formation of isolated ferric ions in extra-framework sites or small iron oxide nanoparticles. The presence of excess iron causes iron particles to coalesce which can create larger aggregated particles greater than 4 nm in diameter (Berlier et al., 2002; Bordiga et al., 1996; Goldfarb et al., 1994). A previous study demonstrated 1% or more of iron concentrations in the material, after being calcined at 550 °C, consist of "iron aggregates" that exhibit a unique EPR signal at g = 2.3 (Berlier et al., 2002). The 3% iron-silica PM surrogates, depicted in Figure 5.1, yielded a g = 2.300 ± 0.100 EPR signal with a $\Delta H_{p\text{-}p}$ of 357 ± 20-G, whereas the 0.5% iron-silica surrogates did not. Thus, the absence of the g = 2.300 signal in 0.5% iron-silica PM surrogates supports the presence of small iron oxide nanoparticles. Furthermore, after heat (T = 450 °C) and vacuum (P = 0.1–0.01 Torr) treatment for 1 h the g = 2.300 EPR signal decreased and the g = 4.270 EPR signal increased. This confirms there was a decrease in particle aggregation and more migration of ferric ions.

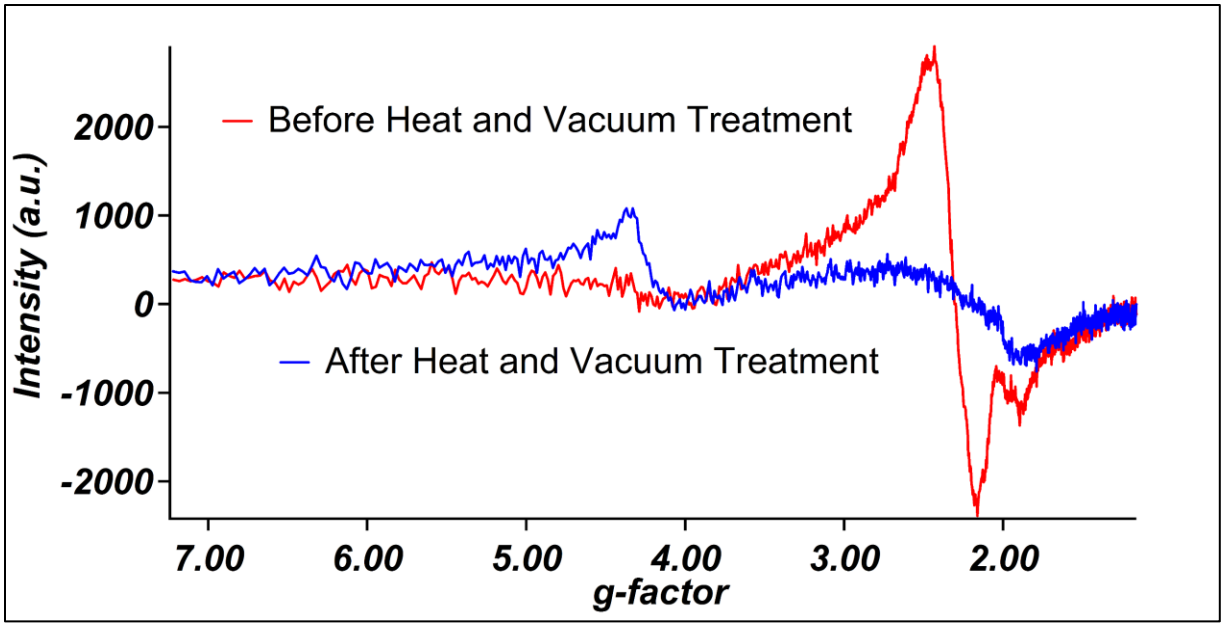

Figure 5.1. 5000-G scan derivative-of-absorption EPR spectrum of 3% iron-silica PM surrogate before (red curve) and after heat and vacuum treatment (blue curve) measured under vacuum.

5.2. Iron aggregates in ambient $PM_{2.5}$

Previous reports identified that iron aggregates yielded a broad g = 2.100 EPR signal in ambient $PM_{2.5}$ and particulate aerosols (Gehling et al., 2013; Ledoux et al., 2002; Ledoux et al., 2004). However, the 3% iron-silica PM surrogate demonstrated iron aggregates yield an EPR signal at g = 2.300, which is slightly different than the ambient $PM_{2.5}$ samples that yielded a signal at g = 2.141 (Figure 4.6). It is proposed the g = 2.141 EPR signal in ambient $PM_{2.5}$ consist of iron aggregates interacting with other paramagnetic species (see Section 4.2). Ambient $PM_{2.5}$ will vary in composition so the amount of other paramagnetic species present will cause it to have slightly different g-factor values. Thus, iron aggregates can yield the g = 2.300 EPR signal observed in the 3% iron-silica PM surrogates and the g = 2.141 EPR signal in ambient $PM_{2.5}$.

5.3. Ferric ions associated with superparamagnetic nanoparticles in PM surrogates

Formation of the iron aggregates in the 3% iron-silica PM surrogates interferes with the formation of isolated ferric ions within extra-framework sites and iron oxide nanoparticles less than 4 nm in diameter but it may not in lower iron concentrations like 0.5%. After the 0.5% iron-

silica PM surrogate was cycled with heat (T = 450 °C) and vacuum (P = 0.1–0.01 Torr) treatment for 1 h, a narrow g = 2.003 EPR signal with a $\Delta H_{p\text{-}p}$ of 9.8 ± 0.1-G appeared including the as-expected increased intensity at the g = 4.270 EPR signal, as shown in Figure 5.2. The thermally/vacuum cycled treated silica (control) did not detect a narrow g = 2.003 EPR signal (Figure 4.2) indicating the signal was generated due to the added iron(III) nitrate nonahydrate. These heterogeneous PM surrogates do not uniformly disperse the metal on the silica surface and therefore the number of repeated heat/vacuum treatments may vary.

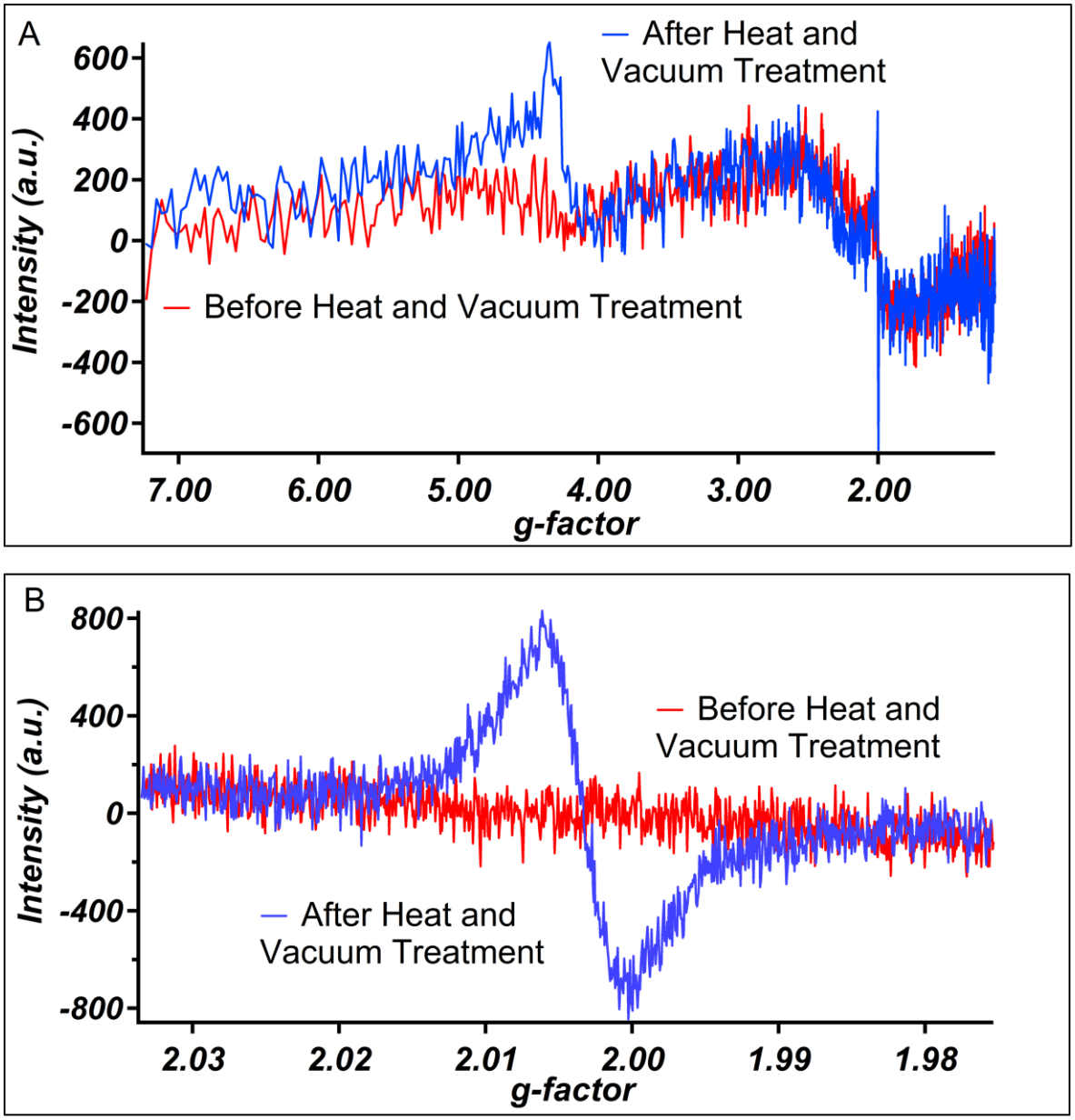

Figure 5.2. Derivative-of-absorption EPR spectra of 0.5% iron-silica PM surrogate before (red curve) and after heat and vacuum treatment (blue curve) measured under vacuum; (A, top) 5000-G scans and (B, bottom) 100-G scans.

Further experimentation on the PM surrogates revealed other important changes. The thermally/vacuum cycled treated 0.5% iron-silica PM surrogate (in Figure 5.2) was then exposed to ambient atmosphere for seven days and then heated to 120 °C for 1 h under ambient atmosphere. An increased intensity in the narrow g = 2.003 EPR signal was observed and is presented in Figure 5.3. Water loss was observed in the TGA samples (Figure 3.7) at around 50–

110 °C and iron hydroxides/oxyhydroxides are known to lose physisorbed water and experience phase transitions in this region (Balek et al., 1995; Bernal, 1959; Dixon et al., 1989; Goss, 1987). The 120 °C temperature was selected to remove water. Also, exposure of ambient $PM_{2.5}$ samples to simulated sunlight for 1 h can heat samples to 50–80 °C. This increased intensity in the narrow g = 2.003 EPR signal (Figure 5.3) and no changes in the intensity at the g = 4.270 and g = 2.141 signals confirms the narrow g = 2.003 EPR signal is independent of the coordination environments of ferric ions. The data strongly suggests magnetism changes from nanoparticles yielded an increased intensity of the narrow g = 2.003 EPR signal that follows the Curie-Weiss Law (Berger et al., 2001; Ferretti et al., 2002). The Curie-Weiss Law describes ferromagnetic properties, like what was found in the PM surrogates, become paramagnetic. This is measurable by EPR. Paramagnets with a greater magnetic susceptibility are considered superparamagnetic. Ferromagnetic iron oxide nanoparticles are known to exhibit superparamagnetic behavior when heated above its "blocking temperature" (Berger et al., 2001). The smaller the particles are the lower the blocking temperature will be. Therefore, the 120 °C treatment is proposed to trigger the ferromagnetic nanoparticles to transition to the superparamagnetic state.

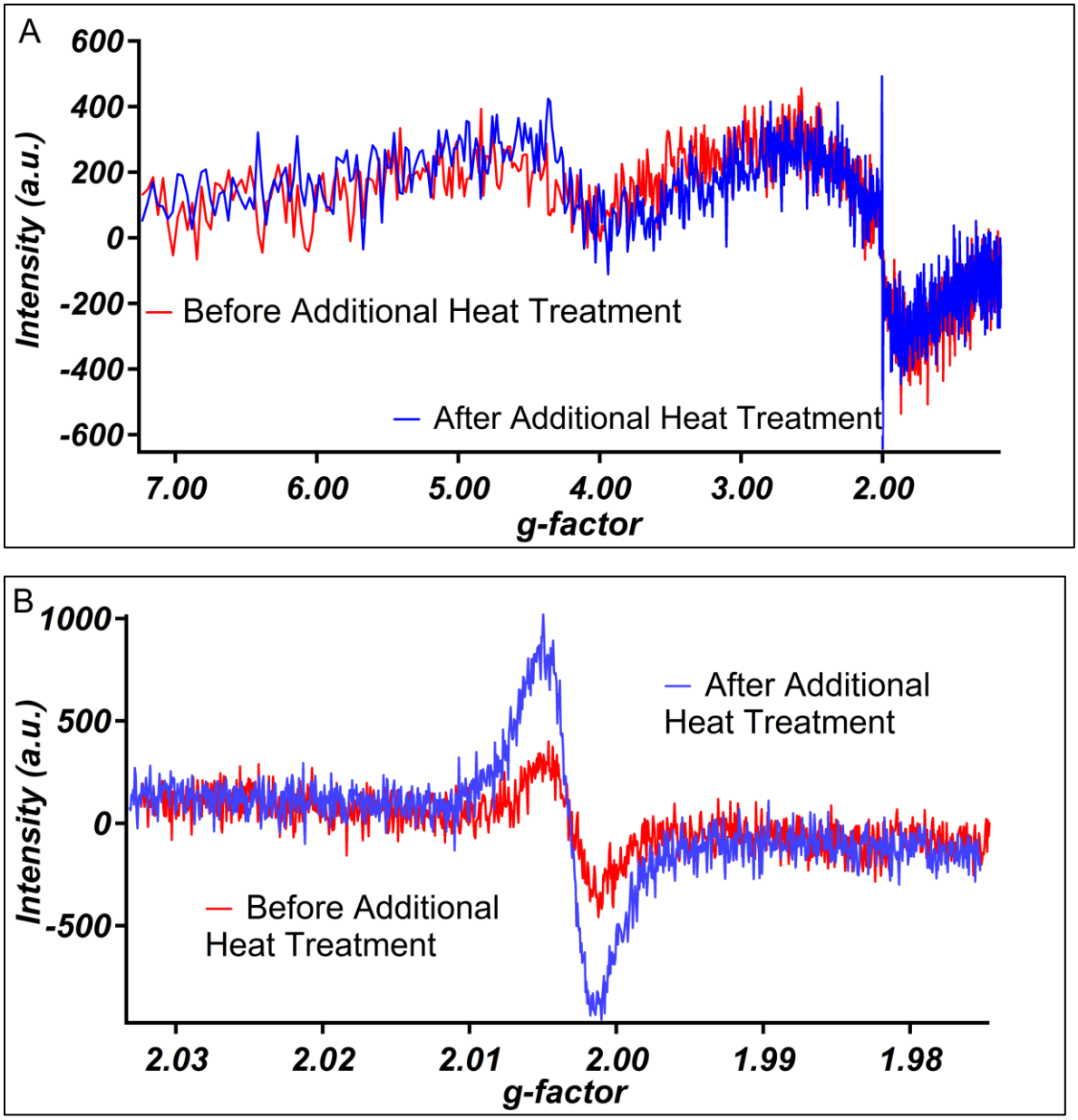

Figure 5.3. Derivative-of-absorption EPR spectra of thermally/vacuum treated 0.5% iron-silica PM surrogate and then exposed to ambient conditions for seven days (red curve) and after 120 °C treatment for 1 h in air (blue curve) measured at ambient conditions; (A, top) 5000-G scans and (B, bottom) 100-G scans.

Previous reports had different evidence about the chemistry that yielded the narrow g = 2.003 EPR signal (Dyrek, 1973; Goldfarb et al., 1994). In one case, superparamagnetic oxygen species was found to yield a narrow g = 2.003 EPR signal, but this is not the case here (Dyrek, 1973). Dyrek explained that adsorption of oxygen leads to an increase in the narrow g = 2.003

EPR signal by oxidation of Fe(II) to Fe(III), which should cause an increased intensity at the g = 4.270 EPR signal upon exposure to ambient conditions. However, this study observed a decreased intensity at g = 4.270 EPR signal upon exposure to ambient conditions.

Changes to the EPR data during treatments were not the only changes observed. A color change in the 0.5% iron-silica PM surrogates was also observed during heat (T = 450 °C) and vacuum (P = 0.1–0.01 Torr) treatment for 1 h. Initially, the 0.5% iron-silica surrogates were a reddish-tan color and then changed to a pale gray. Upon cooling to room temperature under vacuum, the color reverted back to reddish-tan. Because no chemical characterization analyses such as diffuse reflectance UV-vis/NIR could be taken during heat (T = 450 °C) and vacuum (P = 0.1–0.01 Torr) treatment at the time, it is difficult to prove any chemical transformation. It is postulated that a phase transition from γ-Fe_2O_3 (reddish-tan color) to α-Fe_2O_3 (pale gray color) to γ-Fe_2O_3 (reddish-tan color) occurred (Iraj et al., 2014). During heating and cooling, phase transitions of the iron material to hydroxides like goethite, lepidocrocite, and ferrihydrite could occur as they have been observed in weathered minerals and low temperature environments. The presence of water is key to the transformation of iron oxides like hematite to hydroxides and have been observed in other studies (Campbell et al., 1984; Schwertmann, 1971). It is also possible the color changed due to migration of ferric ions to other sites (Amama et al., 2005; Bordiga et al., 1996).

To summarize, the combination of the low iron concentration in the 0.5% iron-silica PM surrogates and vacuum/heat cycled treatment can yield a narrow g = 2.003 EPR signal. It is suggested that under these conditions ferric ions associated with superparamagnetic nanoparticles less than 4 nm in diameter are produced.

5.4. Superparamagnetic nanoparticles in ambient $PM_{2.5}$

If present, ferric ions associated with superparamagnetic nanoparticles less than 4 nm in diameter that yield the narrow g = 2.003 EPR signal should be observable in complex real-world samples like ambient $PM_{2.5}$. Figure 5.4 shows a narrow g = 2.003 EPR signal with a $\Delta H_{p\text{-}p}$ of 9.8 ± 0.3-G was detected after ambient $PM_{2.5}$, supported on a PTFE filter, was heated to 120 °C for 1 h. Some ambient $PM_{2.5}$ samples were also heated to 50 °C for 1 h under ambient atmosphere and experienced a slight increased intensity in the narrow g = 2.003 EPR signal. Because the ambient $PM_{2.5}$ samples vary in composition, concentration, and its sources, some ambient $PM_{2.5}$ samples did not consistently observe the narrow g = 2.003 EPR signal. However, these results not only demonstrate how sensitive the narrow g = 2.003 EPR signal is to temperature, but how easy it is to observe it in samples with low sample weights (weight of ambient $PM_{2.5}$ for all samples were < 0.8 mg). EPR is a valuable instrument to use for future studies on ambient $PM_{2.5}$. Ambient $PM_{2.5}$ can consist of ferric ions associated with superparamagnetic nanoparticles that yield a narrow g = 2.003 EPR signal. When a clean PTFE filter was heated to 120 °C for 1 h under ambient atmosphere a small EPR signal at g = 2.003 was observed as shown in Figure 5.5. Because the silica (control) also exhibited a small signal at g = 2.003 (see Section 4.1) after heat and vacuum treatment, it is suspected the PTFE filter was also contaminated by adventitious carbon (Castle, 2008; deVries et al., 1994; Piao et al., 2002).

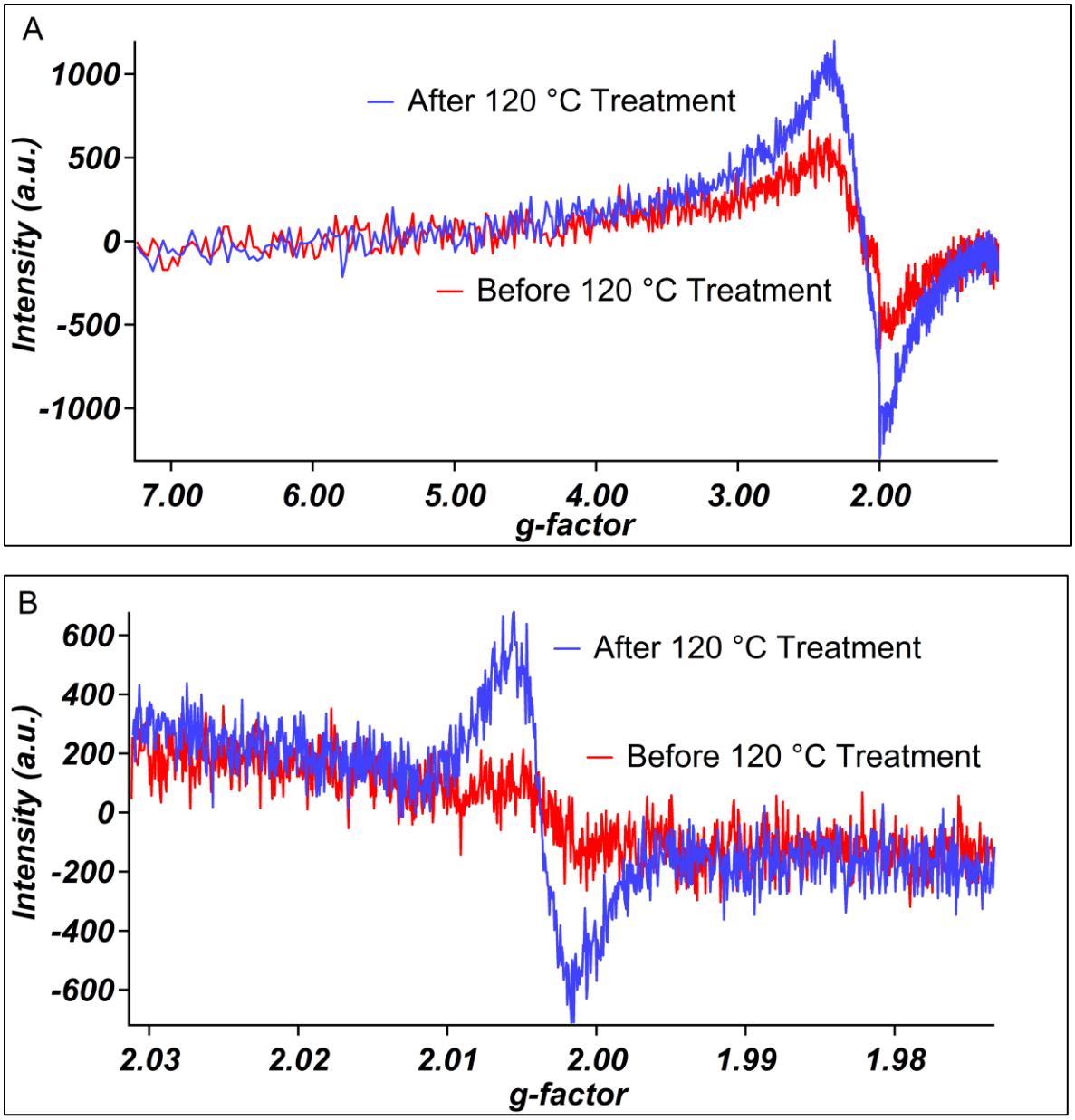

Figure 5.4. Derivative-of-absorption EPR spectra of ambient $PM_{2.5}$ before (red curve) and after 120 °C treatment for 1 h in air (blue curve) measured at ambient conditions. Ambient $PM_{2.5}$ collected on PTFE filter (Sample ID P2919720); (A, top) 5000-G scans (B, bottom) 100-G scans.

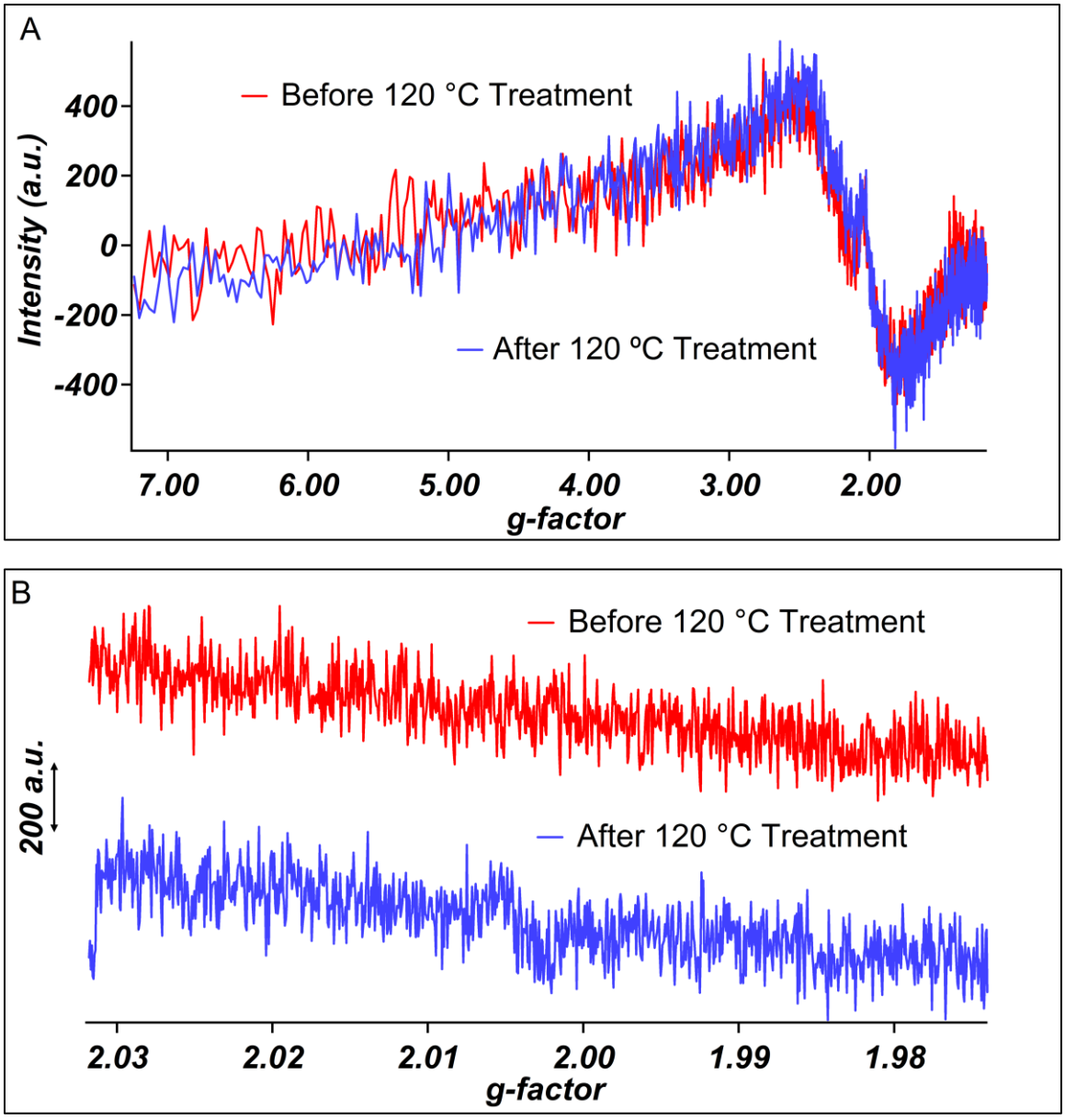

Figure 5.5. Derivative-of-absorption EPR spectra of PTFE filter before (red curve) and after 120 °C treatment for 1 h in air (blue curve) measured at ambient conditions; (A, top) 5000-G scans (B, bottom) 100-G scans.

CHAPTER 6. FREE RADICAL BEHAVIOR IN PM SURROGATES AND AMBIENT $PM_{2.5}$

A previous study shown that phenol-exposed iron-silica materials yield EPFRs with a significantly longer lifetime than copper-silica materials (Vejerano et al., 2012). In order to examine EPFR formation, the 0.5% iron-silica PM surrogates were exposed to vapor-phase phenol. After heat (T = 450 °C) and vacuum (P = 0.1–0.01 Torr) treatment for 1 h is applied (this experimental step was assessed in Chapters 4 and 5), the next step was to expose the PM surrogate to an organic precursor (phenol) under vacuum to form EPFRs that yield a g = 2.003 EPR signal. Most of the previous EPFR formation studies used heat during the exposure step (Kiruri et al., 2014; Vejerano et al., 2011; Vejerano et al., 2012). In this work, the exposure step was carried out at room temperature to mimic atmospheric conditions.

6.1. Phenol-exposed PM surrogates

The 0.5% iron-silica PM surrogate was treated with heat (T = 450 °C) and vacuum (P = 0.1–0.01 Torr) for 1 h, cooled to room temperature under vacuum (P = 0.1–0.01 Torr), and then exposed to phenol vapor under vacuum (P = 0.1–0.01 Torr) for 5 min at room temperature. As displayed in Figure 6.1, no changes were observed in the intensity of existing EPR signals after being exposed to phenol. It was hypothesized that PM surrogates exposed to vapor-phase phenol will produce higher concentrations of radicals, but no radicals/EPFR formed at g = 2.003. Additionally, formations of EPFRs were proposed to result in a decrease in irons oxidation state from ferric ions to ferrous ions. No changes in the intensity of the g = 4.270 EPR signal confirms there were no changes in the oxidation state of iron. Silica (control) treated the same as above also had no intensity changes in the g = 2.003 EPR signal as shown in Figure 6.2. The observed g = 2.003 EPR signal with low intensity in Figures 6.1 and 6.2 was discussed in Section 4.1 and not associated with phenol.

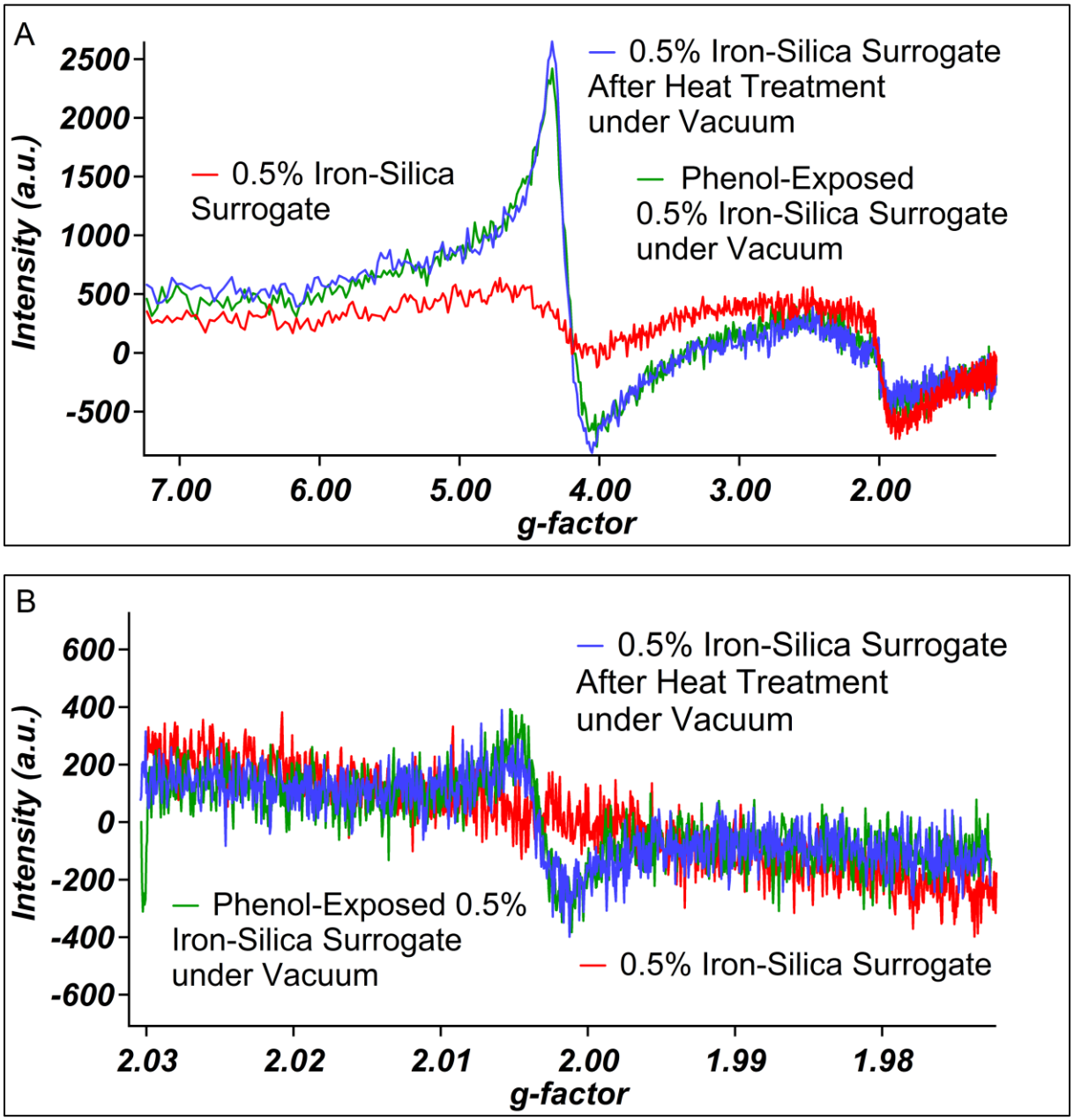

Figure 6.1. Derivative-of-absorption EPR spectra of 0.5% iron-silica PM surrogate before (red curve) and after heat and vacuum treatment (blue curve) and then exposed to phenol vapor at room temperature (green curve) measured under vacuum; (A, top) 5000-G scans and (B, bottom) 100-G scans.

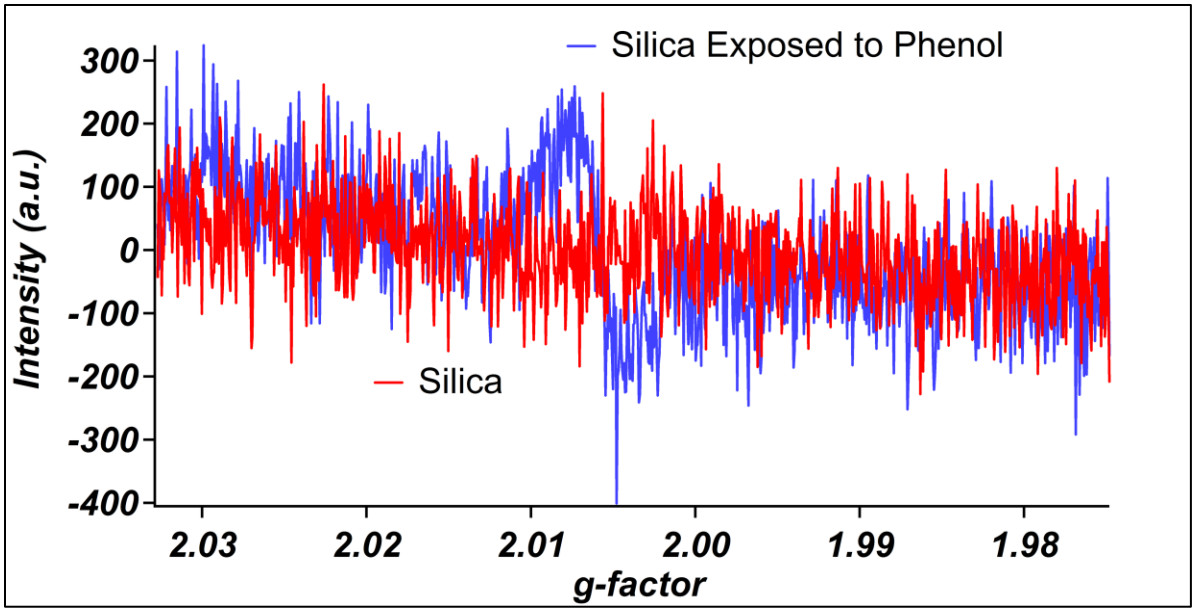

Figure 6.2. 100-G scans derivative-of-absorption EPR spectra of silica before (red curve) and after heat and vacuum treatment and then exposed to phenol vapor at room temperature (blue curve) measured under vacuum.

To confirm the adsorption of phenol occurred, diffuse reflectance UV-Vis/NIR was conducted. As displayed in Figure 6.3, phenol adsorbed to the thermal/vacuum treated silica. The two bands at 219 and 268 nm are characteristic of $n \rightarrow \sigma^*$ (phenol) and $\pi \rightarrow \pi^*$ (aromatic) electron transitions, respectively (Fan et al., 2018). Prior to thermal/vacuum treatment and phenol exposure the 0.5% iron-silica PM surrogates yielded a maximum adsorption peak at 274 nm (green curve, Figure 6.3). After thermal/vacuum treatment followed by phenol exposure, there was a shift in the maximum adsorption peak to 283 nm and broadening of the band greater than 300 nm (yellow curve, Figure 6.3). In short, both the silica and 0.5% iron-silica PM surrogates can indeed adsorb vapor-phase phenol at room temperature.

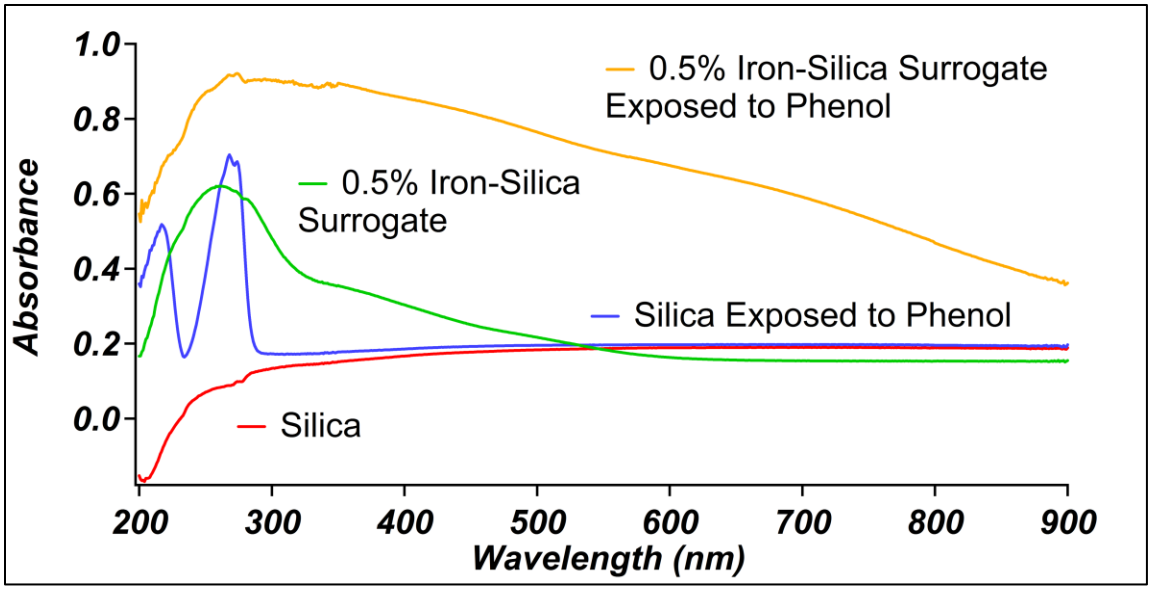

Figure 6.3. Diffuse reflectance UV-Vis/NIR spectra of silica unexposed (red curve) and exposed to phenol vapor (blue curve) and 0.5% iron-silica PM surrogate unexposed (green curve) and exposed to phenol vapor (orange curve).

The broad adsorption band greater than 300 nm indicates polymeric behavior because conjugated polymers are known to adsorb in the 400–800 nm region (Su, 2013). These observations agree with Church and coworkers who reported quinone and hydroquinone polymers in cigarette smoke (Church et al., 1985). Generation of ROS was shown to be triggered by EPFRs (Scheme 1.3), whereas others reported quinone/hydroquinone polymers generated ROS (Church et al., 1985).

Because the characterization of the iron formed could not be determined it is unclear exactly the reason(s) for phenol's adsorption on the 0.5% iron-silica PM surrogate. However, a previous report did indicate phenol's adsorption on a hematite material (McBride et al., 1991). Heating hematite at temperatures between 340–950 °C releases chemisorbed water (Breeuwsma, 1973). The 0.5% iron-silica PM surrogate was treated with heat (T = 450 °C) and vacuum (P = 0.1–0.01 Torr) for 1 h prior to phenol exposure. It is suggested that the heat/vacuum treatment removed amounts of chemisorbed water (hydroxides at Brønsted acid sites) and by maintaining the 0.5% iron-silica PM surrogate under vacuum (P = 0.1–0.01 Torr) at room temperature,

prevented amounts of water molecules to re-adsorb. As shown in Scheme 6.1, these sites allowed vapor-phase phenol to chemisorb. For silica the UV-Vis/NIR data (Figure 6.3) demonstrated phenol adsorbed through hydrogen bonding between the hydroxyl groups of the silica and phenol (Djebbar et al., 2012; Naono et al., 1980).

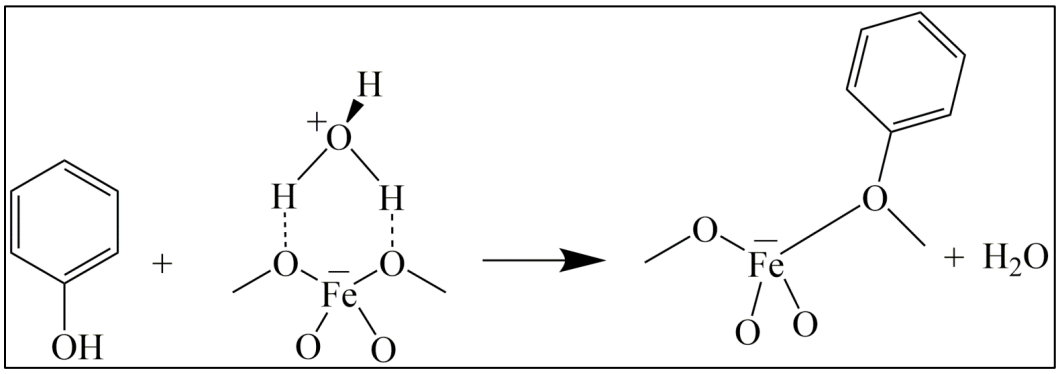

Scheme 6.1. Chemisorption of vapor-phase phenol on iron (Fe(III)) particle surface.

It is also important to note the color change. Initially, the as-prepared 0.5% iron-silica PM surrogates exhibited a reddish-tan color. After, the 0.5% iron-silica PM surrogates were treated with heat (T = 450 °C) and vacuum (P = 0.1–0.01 Torr) for 1 h, cooled to room temperature under vacuum, and then exposed to vapor-phase phenol under vacuum, a stable gray color was observed. The gray color was stable at ambient conditions. Scheme 6.2 reports the colors observed during the different experimental steps for the 0.5% iron-silica PM surrogates. These reported color changes further confirm the adsorption of phenol on 0.5% iron- silica PM surrogates at room temperature.

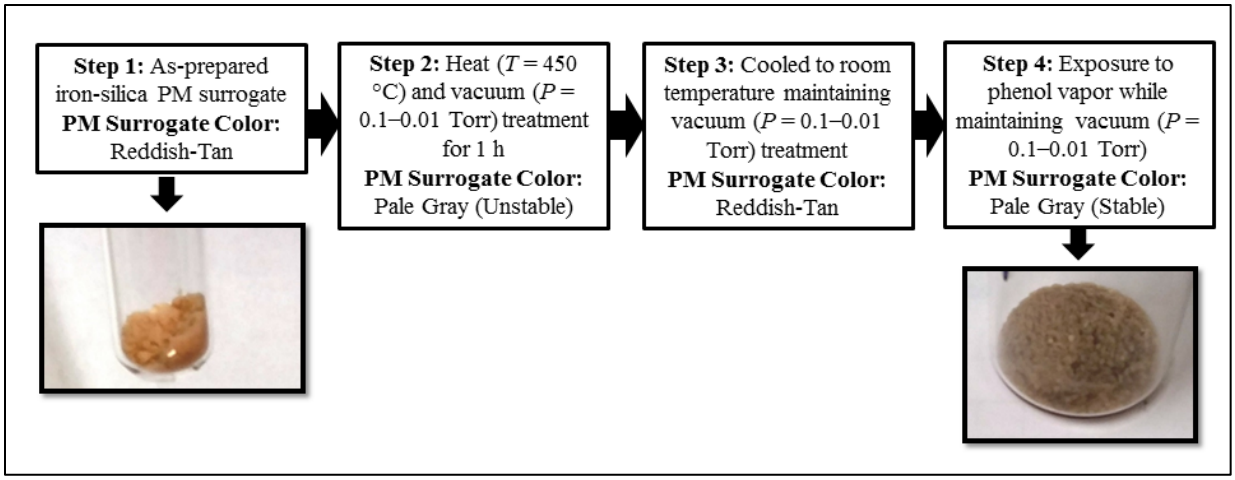

Scheme 6.2. Observed color changes for iron-silica PM surrogate during different experimental steps.

6.2. Heated phenol-exposed PM surrogates

The phenol-exposed 0.5% iron-silica PM surrogate used in Section 6.1 was then heated to 450 °C for 1 h under ambient conditions. This yielded an increased intensity in the g = 4.270 (distorted tetrahedral ferric sites) and narrow g = 2.003 ± 0.002 ($\Delta H_{p\text{-}p}$ = 9.8 ± 0.1-G) EPR signals, as shown in Figure 6.4. Organic radical formation is known to occur at temperatures above 300 °C (Church et al., 1985; Loktev et al., 1976; Sawhney et al., 1984; Weckhuysen et al., 1997). The increased response in the g = 2.003 EPR signal corresponds to the formation of organic radicals that follow the Curie-Weiss Law (Weckhuysen et al., 1997). Both the organic radicals and ferric ions associated with superparamagnetic nanoparticles (isolated ferric ions within extra-frameworks sites or iron oxide nanoparticles) obey the Curie-Weiss Law. However, when the phenol-exposed 0.5% iron-silica PM surrogate heated to 450 °C for 1 h under ambient conditions was exposed to ambient conditions for seven days and then heated at 120 °C for 1 h under ambient conditions, no intensity changes at the g = 2.003 EPR signal were observed as shown in Figure 6.5. This supports that the 120 °C temperature treatment can be used to indicate the presence of ferric ions associated with superparamagnetic nanoparticles in ambient $PM_{2.5}$.

The ferric ions associated with superparamagnetic nanoparticles (Figure 5.3) yielding the g = 2.003 EPR signal increased after being heated at 120 °C for 1 h under ambient conditions.

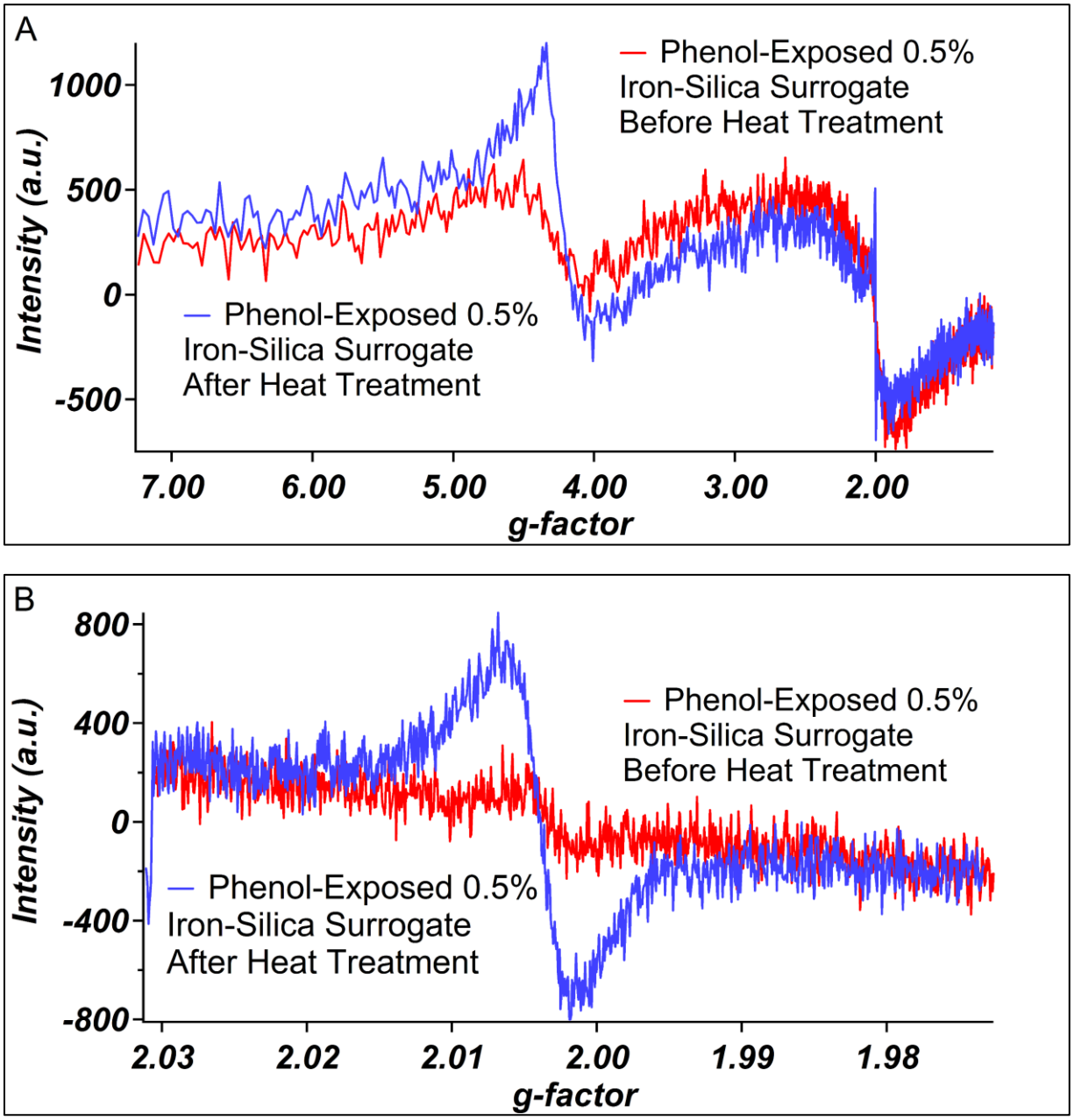

Figure 6.4. Derivative-of-absorption EPR spectra of 0.5% iron-silica PM surrogate after heat and vacuum treatment and exposed to phenol at room temperature (red curve) measured at ambient conditions, and then after being heated to 450 °C for 1 h in ambient atmosphere (blue curve); (A, top) 5000-G scans and (B, bottom) 100-G scans.

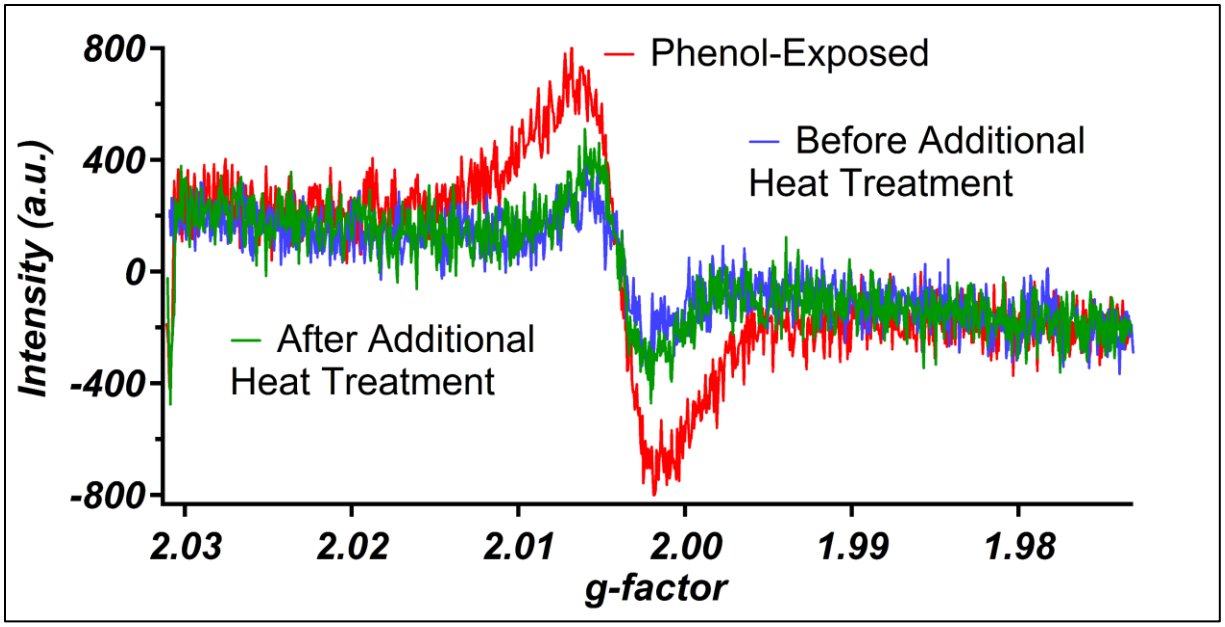

Figure 6.5. 100-G scans derivative-of-absorption EPR spectra of thermally treated phenol-exposed 0.5% iron-silica PM surrogate (red curve) and then exposed to ambient conditions for seven days (blue curve) and after 120 °C treatment for 1 h in ambient atmosphere (green curve) measured at ambient conditions.

To gain more chemical information on the phenol-exposed 0.5% iron-silica PM surrogates, thermogravimetric analysis was conducted. Figure 6.6 reveals there was a 1–2% weight loss at about 130 °C and 160 °C for both the phenol-exposed silica and 0.5% iron-silica PM surrogate, respectively. This indicates the loss of phenol because it has a boiling point of about 181 °C. Additionally, a 1% weight loss for the phenol-exposed 0.5% iron-silica PM surrogate was shown between the temperatures of 321–430 °C that is similar to the TGA results reported for poly(*p*-phenylene) in phenol-exposed clay systems (Nwosu et al., 2016). Polymer-type materials have been suspected to be present in PM surrogates before, but lacked adequate evidence (Li et al., 2016; Yi et al., 2019). Importantly, this study now provides that evidence by using diffuse reflectance UV-Vis/NIR. It is suggested that phenol adsorbs to the oxygen atoms associated with ferric ions in distorted tetrahedral sites (due to the g = 4.270 EPR signal increase in Figure 6.4) and polymerize to a poly(*p*-phenylene) material. At elevated temperatures, the poly(*p*-phenylene) material would oxidize and yield radicals stabilized by delocalization shown

in Scheme 6.3. These findings are further supported by Sawhney and coworkers who characterized the polymerization of 2,6-dimethylphenol in smectite materials and Yi and coworkers who identified dimer-type radicals by catechol degradation on hematite (Sawhney et al., 1984; Yi et al., 2019).

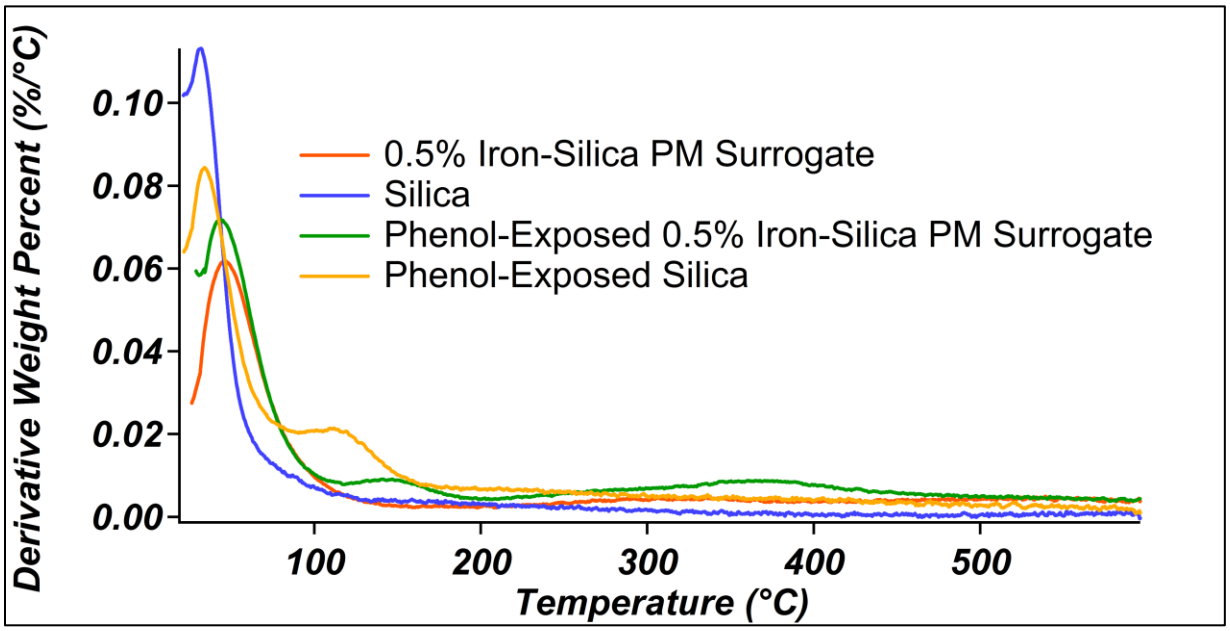

Figure 6.6. Thermogravimetric analysis plots of unexposed and phenol-exposed silica and 0.5% iron-silica PM surrogates.

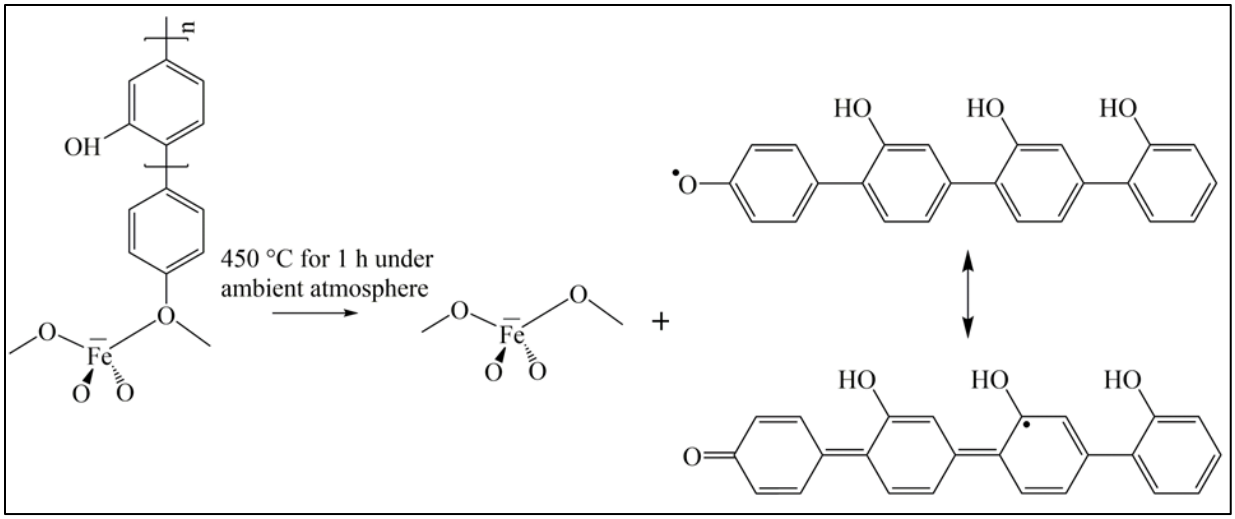

Scheme 6.3. Proposed reaction showing stable radicals formed from the oxidation of adsorbed poly(*p*-phenylene) material on PM surrogates.

To further support the presence of having both organic radicals and ferric iron associated with superparamagnetic nanoparticles, soot and soot-iron PM surrogates were generated from the dual zone reaction system (Herring, 2013). As shown in Figure 6.7, the oxidation of 1-methylnapthelene yielded a narrow g = 2.003 EPR signal ($\Delta H_{p\text{-}p}$ = 100-G). The oxidation of 1-methylnapathelene with iron also yielded a narrow g = 2.003 EPR signal ($\Delta H_{p\text{-}p}$ = 47-G) as displayed in Figure 6.8. Interestingly, when the soot and soot-iron PM surrogates were placed under vacuum the $\Delta H_{p\text{-}p}$ of soot decreased to 13-G while the soot-iron PM surrogate remained unaffected. The observed $\Delta H_{p\text{-}p}$ of 13-G reported for soot is closer in value to the $\Delta H_{p\text{-}p}$ of 9.8-G reported in the 0.5% iron-silica PM surrogates at the g = 2.003 EPR signal. The soot-iron PM surrogate $\Delta H_{p\text{-}p}$ was not affected by the vacuum treatment (P = 0.1–0.01 Torr) due to overlapping ~g = 2.003 EPR signals from the presence of organic radicals and iron oxide nanoparticles. The soot PM surrogate experienced a narrowing of the EPR signal when placed under vacuum that is possibly due to the removal of adsorbed organics (Ross et al., 1982). Previous studies on other materials with various iron concentrations also reported broadening effects around g = 2 during vacuum/heat treatments (Amama et al., 2005; Goldfarb et al., 1994; Tuel et al., 1998). Goldfarb and coworkers reported materials with 0.07% iron concentrations experienced broadening effects at g = 2 EPR signal due to the overlap of a narrow and broad EPR signal (Goldfarb et al., 1994). Also, particle size and number of iron oxide nanoparticles may influence the intensity and shape of the EPR signal at g = 2.003 but was not studied in this work.

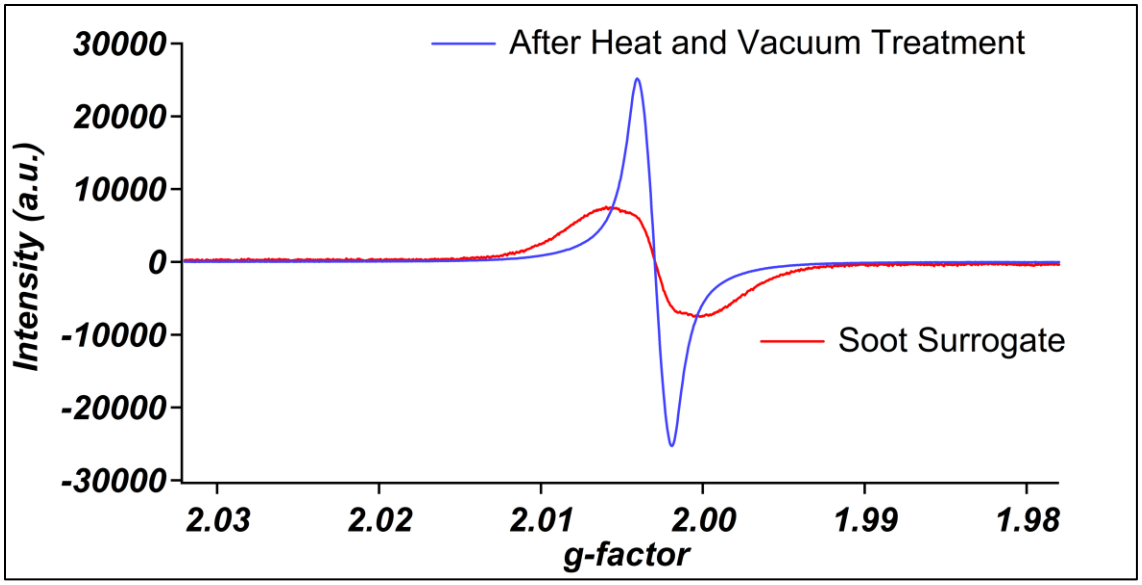

Figure 6.7. 100-G scans derivative-of-absorption EPR spectrum of soot PM surrogate before (red curve) and after heat and vacuum treatment (blue curve) measured under vacuum.

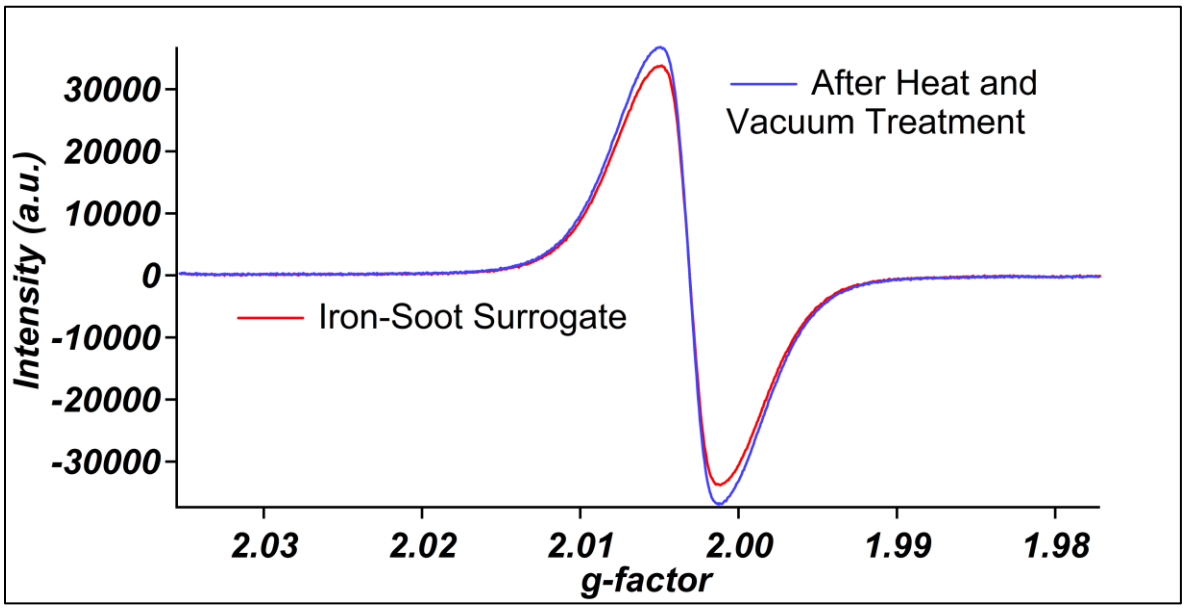

Figure 6.8. 100-G scans derivative-of-absorption EPR spectrum of soot-iron PM surrogate before (red curve) and after heat and vacuum treatment (blue curve) measured under vacuum.

6.3. Phenol-exposed ambient $PM_{2.5}$

The phenol-exposure experimental steps conducted on the 0.5% iron-silica surrogates could not be used on the ambient $PM_{2.5}$ supported on the PTFE filters. The melting point of the PTFE is 327 °C which is below the temperature used during heat treatment (T = 450 °C). So, the

ambient $PM_{2.5}$ supported on the PTFE filters were placed under vacuum treatment (P = 0.1–0.01 Torr) for 1 h at room temperature and then exposed to vapor-phase phenol while maintaining vacuum (P = 0.1–0.01 Torr) for 5 min. As depicted in Figure 6.9, an increase in intensity of the g = 2.003 EPR signal ($\Delta H_{p\text{-}p}$ = 9.8-G) was observed after vacuum treatment and a very small increase was observed after the samples were exposed to phenol. Like the soot PM surrogate (discussed in Section 6.2), the vacuum may have removed adsorbed organics that would yield an increased intensity in the g = 2.003 EPR signal.

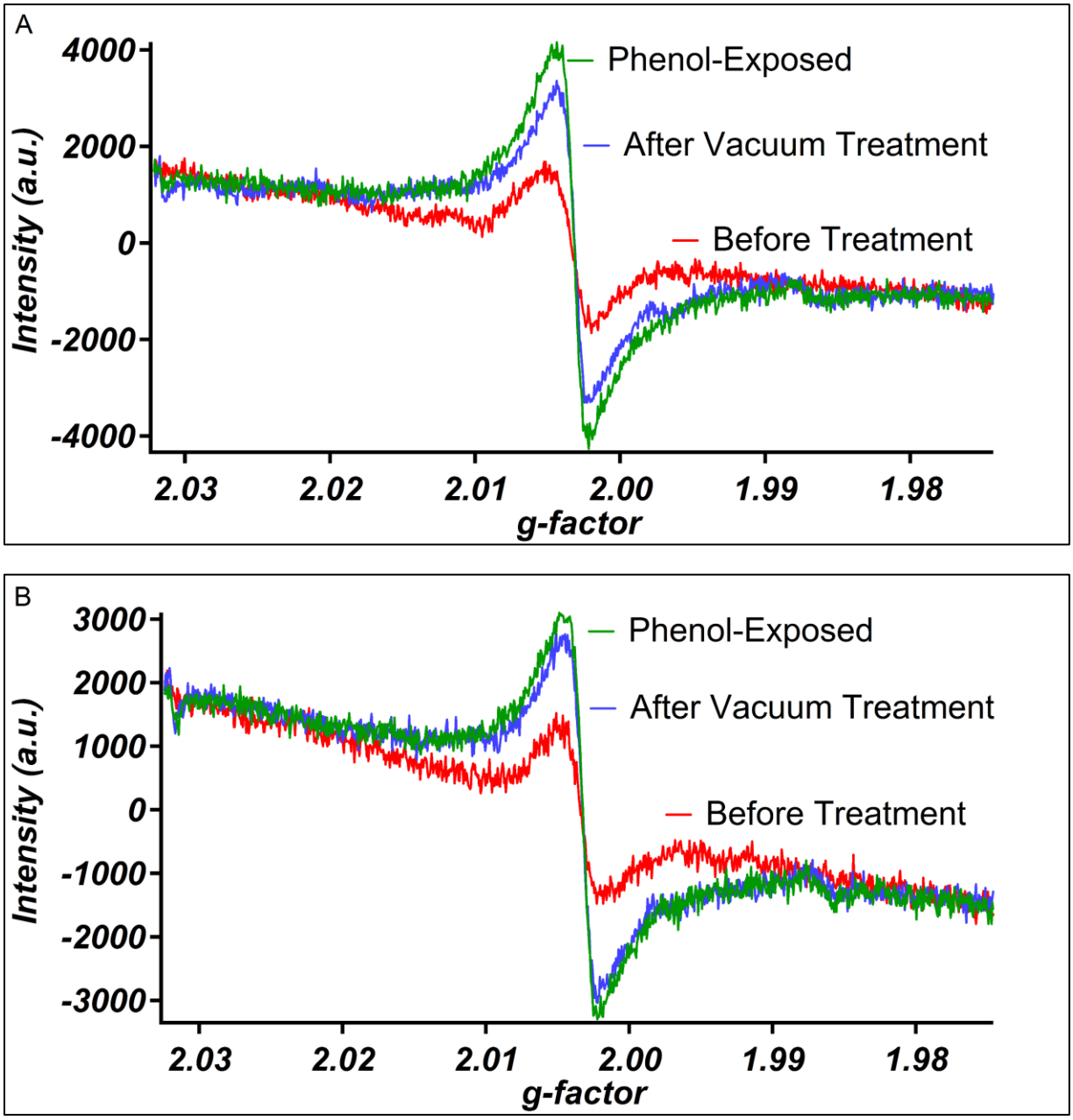

Figure 6.9. 100-G scans derivative-of-absorption EPR spectra of ambient $PM_{2.5}$ collected on PFTE filter before (red curve), after vacuum treatment (blue curve) measured under vacuum, and exposed to phenol (green curve) measured under vacuum; (A, top) Sample ID P2916124 and (B, bottom) Sample ID P2916127.

6.4. Simulated sunlight effects on ambient $PM_{2.5}$

It was previously reported that simulated sunlight treatment on ambient $PM_{2.5}$ yields an increased intensity at the g = 2.003 EPR signal (Gehling, 2013). First experimental treatment should be addressed. Gehling used an extraction technique to remove ambient $PM_{2.5}$ from a

microglass fiber filter (Gehling, 2013). The extracted ambient $PM_{2.5}$ was heated to 120 °C for 5 hours (referred to as treated $PM_{2.5}$) prior to conducting simulated sunlight experiments. As discussed earlier, ambient $PM_{2.5}$ collected on the PTFE filter (untreated $PM_{2.5}$) heated to 120 °C can have an increased intensity at the g = 2.003 EPR signal (Figure 5.4). Thus, heating extracted ambient $PM_{2.5}$ to 120 °C for 5 hours may not be the best approach.

When the treated ambient $PM_{2.5}$ was exposed to simulated sunlight, an increased intensity at g = 2.003 EPR signal was observed as shown in Figure 6.10. However, when the treated ambient $PM_{2.5}$ was stored at 0 °C for four weeks and then exposed to simulated sunlight there were no intensity changes at the g = 2.003 EPR signal as displayed in Figure 6.11. This suggests that the extraction procedures or storing method needs further investigation.

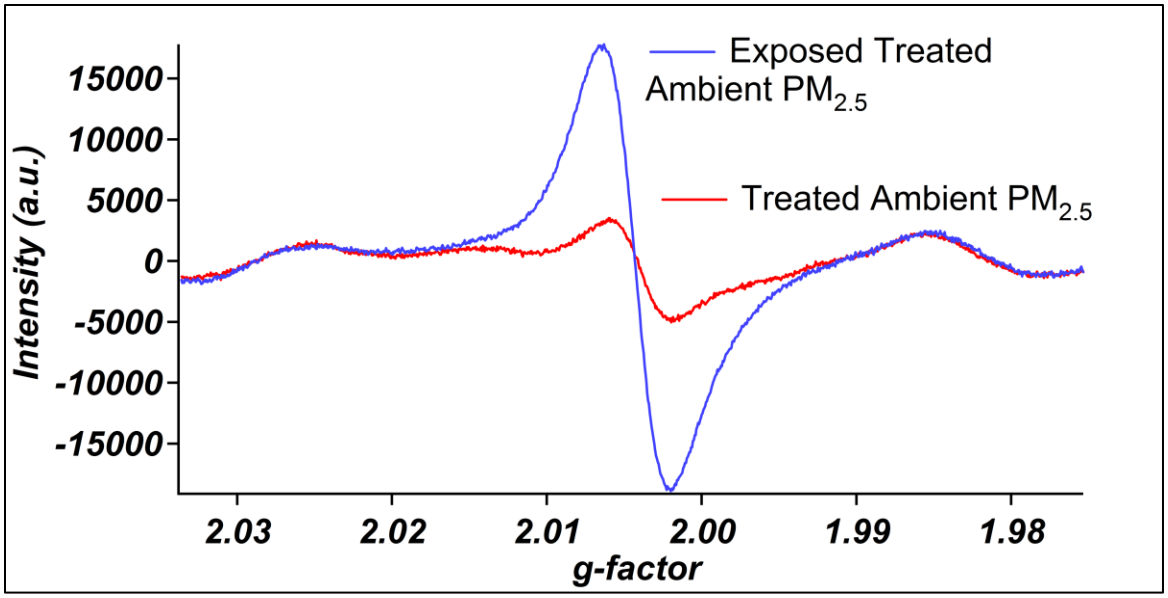

Figure 6.10. 100-G scans derivative-of-absorption EPR spectrum of treated ambient $PM_{2.5}$ before (red curve) and after exposure to simulated sunlight for 60 minutes (blue curve).

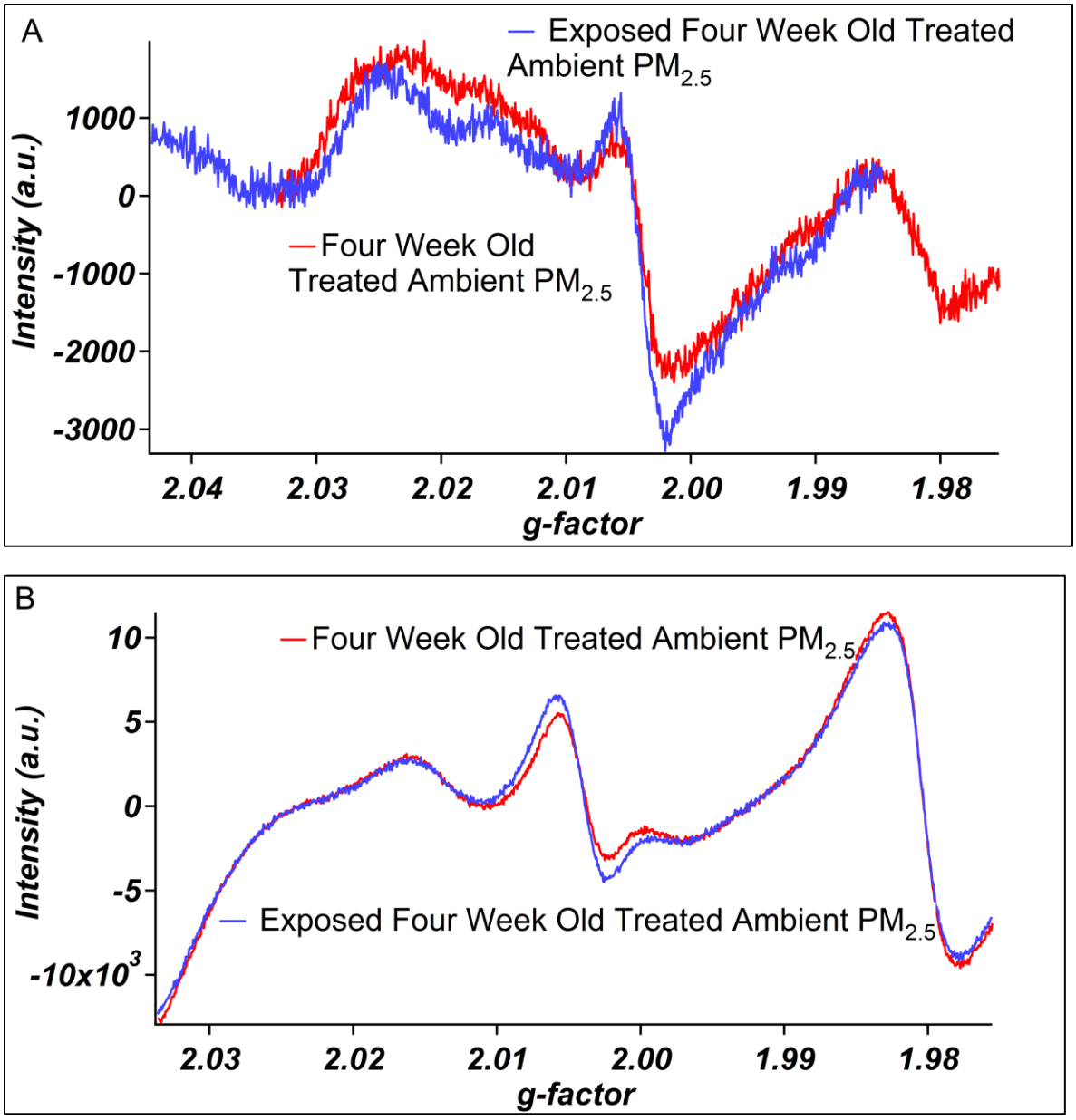

Figure 6.11. 100-G scans derivative-of-absorption EPR spectrum of four week old treated ambient $PM_{2.5}$ before (red curve) and after exposure to simulated sunlight (blue curve) for 60 minutes; (A, top) sample one and (B, bottom) sample two.

It was hypothesized that exposure of simulated sunlight will generate higher concentrations of radicals in ambient $PM_{2.5}$. This was not the case for ambient $PM_{2.5}$ collected on PTFE filters. Simulated sunlight treatment did not affect the intensity of the g = 2.003 EPR signal as show in Figure 6.12. Control experiments where ambient $PM_{2.5}$ was not exposed to simulated sunlight also showed no intensity differences at the g = 2.003 EPR signal, as depicted

in Figure 6.13. Furthermore, clean PTFE filters did not yield a g = 2.003 EPR signal during the experimental treatment, as shown in Figure 6.14. In conclusion, ambient $PM_{2.5}$ collected on PTFE filter was not affected by simulated sunlight for an exposure period of 60 minutes at the g = 2.003 EPR signal.

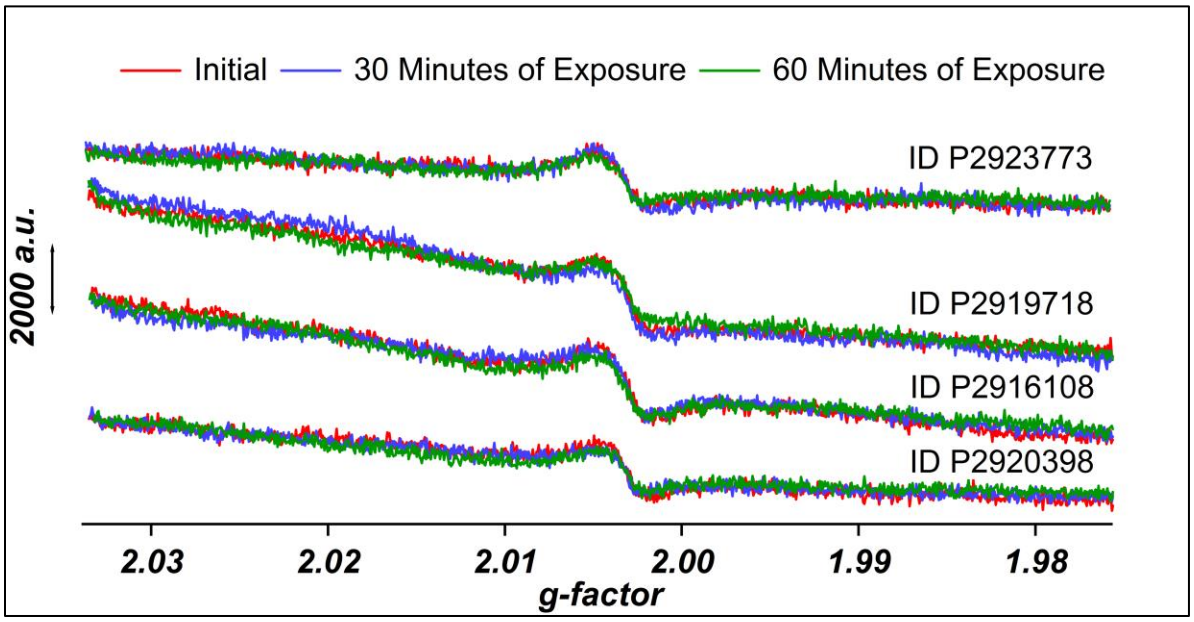

Figure 6.12. 100-G scans derivative-of-absorption EPR spectrum of different ambient $PM_{2.5}$ collected on PTFE filters before (red curve) and after exposure to simulated sunlight for 30 minutes (blue curve), and 60 minutes (green curve).

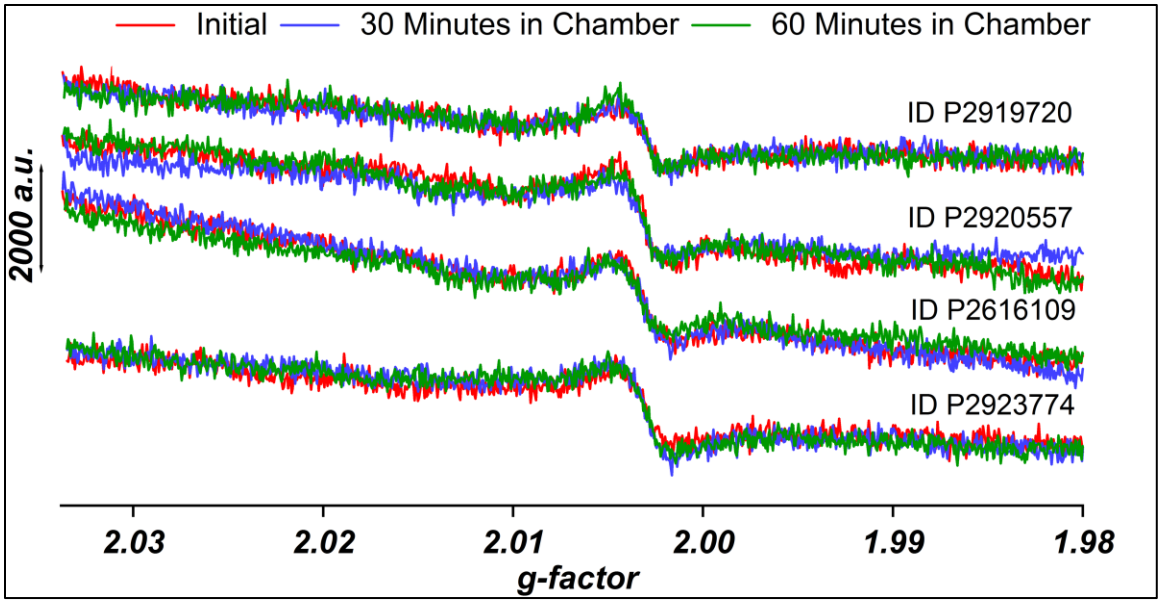

Figure 6.13. 100-G scans derivative-of-absorption EPR spectrum of different ambient $PM_{2.5}$ collected on PTFE filters before (red curve) and after 30 minutes (blue curve), and 60 minutes (green curve) in the environmental chamber.

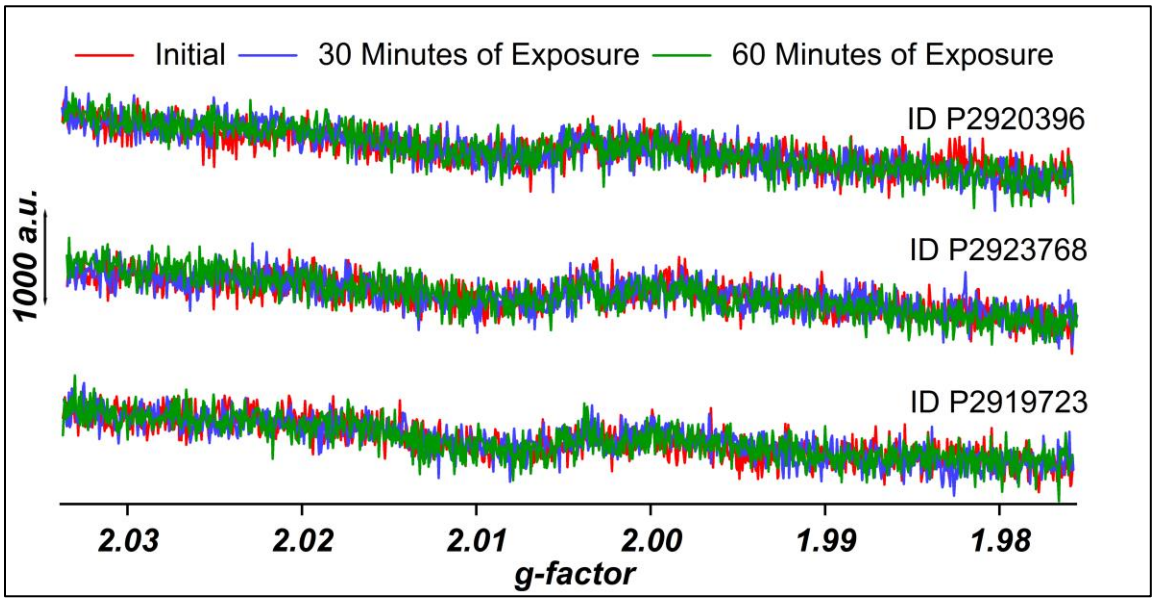

Figure 6.14. 100-G scans derivative-of-absorption EPR spectrum of different PTFE filters before (red curve) and after exposure to simulated sunlight for 30 minutes (blue curve), and 60 minutes (green curve).

Through imaging, differences in particle behavior were observed between the ambient $PM_{2.5}$ samples. As shown in Image 6.1, the treated ambient $PM_{2.5}$ did not exhibit aggregation behavior unlike the ambient $PM_{2.5}$ collected on the PTFE filter (see Image 3.3). When there is less aggregation more particle surface areas are exposed to the simulated sunlight. The increased intensity at the g = 2.003 EPR signal (Figure 6.10) after exposure to simulated sunlight for the treated ambient $PM_{2.5}$ could be due to an increase in the exposed particle surfaces. Also, the treated ambient $PM_{2.5}$ particles appear to have a shell thickness of ~0.8 μm from polydimethylsiloxane contamination (Image 6.1). Polydimethylsiloxane was used in the method discussed in Section 2.1.2. Also, the shell thickness is a concern because it may interfere with the free radical formation that occurs on surfaces of metal oxides.

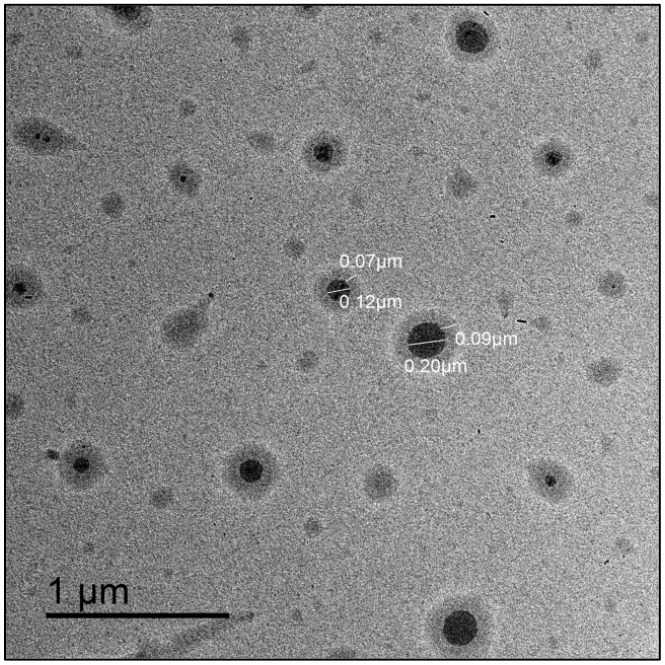

Image 6.1. TEM image of treated ambient $PM_{2.5}$ (see Section 2.1.2 for method).

CHAPTER 7. CONCLUSIONS

7.1. Summary and conclusions

Free radicals have been previously revealed to yield a narrow g = 2 EPR signal in ambient $PM_{2.5}$ and PM surrogates. To help understand the free radical behavior in ambient $PM_{2.5}$, samples were compared to synthetically prepared PM surrogates. Various vacuum and heating experiments were conducted to examine the EPR signals at g-factor values of 4.3, 2.3, 2.1, and 2 (narrow and broad EPR signal shapes).

The g = 4.270 and broad g = 2.141 EPR signals detected in the iron-silica PM surrogates are associated with ferric ions in distorted coordination environments and either undistorted tetrahedral or octahedral coordination environments, respectively. Hydration and dehydration of the Brønsted acid sites led to changes in the intensity of these two signals. In $PM_{2.5,}$ the g = 4.270 and broad g = 2.414 EPR signals were not observed because of $PM_{2.5}$'s complex composition. However, heat treatment on ambient $PM_{2.5}$ did yield an increased intensity in the narrow g = 2.003 EPR signal. This behavior was identical to observations reported for the 0.5% iron-silica PM surrogates. In the phenol-exposed 0.5% iron-silica surrogates, heating to 450 °C led to the formation of free radicals that yielded a narrow g = 2.003 EPR signal. The free radicals were stabilized by delocalization of an oxidized poly(*p*-phenylene) material. In unexposed 0.5% iron-silica PM surrogates ferric ions associated with superparamagnetic nanoparticles (isolated ferric ions in extra-frameworks or iron oxide nanoparticles less than 4 nm in diameter) also yielded a narrow g = 2.003 EPR signal. When the nanoparticles were heated to 120 °C in ambient atmosphere, the intensity of the g = 2.003 EPR signal increased, whereas no intensity changes were observed for the free radicals. This increase was due to ferromagnetic nanoparticles transitioning to a superparamagnetic state. Heating ambient $PM_{2.5}$ to 120 °C also yielded an

increased intensity of the narrow g = 2.003 EPR signal demonstrating the presence of superparamagnetic nanoparticles.

Additionally, the 3% iron-silica PM surrogates yielded a g = 2.300 EPR signal and ambient $PM_{2.5}$ yielded a g = 2.128 EPR signal. Both EPR signals correspond to the presence of iron aggregates. Finally, the PM surrogates, silica, and clean PTFE filters yielded a small narrow g = 2.003 EPR signal that indicates contamination from adventitious carbon.

The following hypotheses were assumed: (1) ambient $PM_{2.5}$ and PM surrogates with higher metal content will have higher concentrations of radicals; (2) ambient $PM_{2.5}$ and PM surrogates exposed to vapor-phase phenol will produce higher concentrations of radicals; and (3) exposure of simulated sunlight will generate higher concentrations of radicals in ambient $PM_{2.5}$. All these hypotheses were disproven. Exposure of vapor-phase phenol at room temperature to PM surrogates did not lead to the formation of free radicals/EPFRs even when metal content was increased. However, oxidation of the phenol-exposed PM surrogates led to the formation of free radicals. Evacuation of ambient $PM_{2.5}$ samples increased the narrow g = 2.003 EPR signal and another increase was observed upon exposure to vapor-phase phenol. However, it is unclear if the increase after exposure to vapor-phase phenol was due to free radical formation or removal of water/organics. Exposure of simulated sunlight did not increase the free radicals EPR signal at g = 2.003 for ambient $PM_{2.5}$ supported on PTFE filters.

The following conclusions were made as a result of the findings from the present study: (1) presence of adventitious carbon can yield a small narrow g = 2 EPR signal; (2) oxidized poly(*p*-phenylene) material led to free radical formation that yields a narrow g = 2 EPR signal; (3) phenol can adsorb at room temperature to the iron-silica PM surrogates, but absence from EPFR formation; (4) ferric ions associated with superparamagnetic nanoparticles also yield a

narrow g = 2 EPR signal and were detected in ambient $PM_{2.5}$ and 0.5% iron-silica PM surrogates; and (5) simulated sunlight had no effect on the narrow g = 2 EPR signal detected in ambient $PM_{2.5}$ supported on PTFE filters.

It should be noted that some of these conclusions were rationalized. Working with low metal concentrations and real-world particulate matter poses many challenges. Regardless, the present study has gained more insight in understanding these difficulties.

7.2. Future work

Future analyses should consider using another characterization technique like Mössbauer spectroscopy. Using both Mössbauer and diffuse reflectance UV-Vis/NIR spectroscopy would resolve some of the uncertainty if they were designed for in situ spectroscopic experiments. Diffuse reflectance UV-Vis/NIR spectroscopy can determine changes in coordination environments and Mössbauer spectroscopy can determine the oxidation state of iron in the PM surrogates. Determining whether iron is oxidizing or reducing at each of the experimental steps will explain or further support the chemical reaction(s) occurring on the particle surfaces. This present study was not able to confirm the PM surrogates chemical changes during heat (T = 450 °C) and vacuum (P = 0.1–0.01 Torr) treatment for 1 h. Only the color change of the PM surrogate from a reddish-orange color to an unstable pale gray color was observed. Diffuse reflectance UV-Vis/NIR spectroscopy could indicate if the color change was a result of ferric ions migrating during heat/vacuum treatment. Also, Mössbauer spectroscopy data could further confirm if the adsorption of phenol on the PM surrogates did not change the oxidation state of iron.

Measuring samples by EPR spectroscopy using low temperatures may also provide valuable information in the changes of the oxidation states (Herring et al., 2015). Splitting of the

energy levels increase at lower temperatures which helps to ensure the highest EPR signal intensities are achieved (Rouault, 2017). Freezing the sample also decreases the dielectric loss which will improve the sensitivity of the instrument (Rouault, 2017).

Another future work idea is to prepare PM surrogates with different iron concentrations and conduct TEM during in situ experiments. This might allow one to examine aggregation behavior of iron particles. However, the present study was not able to distinguish between the amorphous iron and silica particles by TEM. A homogeneous catalyst could be considered because the amorphous iron particles are less likely to aggregate, making it easier to identify their sizes by TEM. Also, a homogeneous catalyst would allow control on the particle sizes of iron. Thus, it could be demonstrated by creating particles less than 4 nm in diameter yields a narrow g = 2.003 EPR signal and particles greater than 4 nm in diameter does not. Furthermore, after heat (T = 450 °C) and vacuum (P = 0.1–0.01 Torr) treatment for 1 h on a homogeneous catalyst, TEM could confirm if this treatment led to smaller particle sizes of iron without needing to do in situ experiments. A previous study observed less aggregation and smaller particle sizes of cobalt after heat and vacuum treatment on a cobalt-silica catalyst (Zhou et al., 2011). After heat/vacuum experiments, the different particle sizes of the homogeneous catalysts could be exposed to the vapor-phase phenol and oxidized to observe if the smaller metal particle sizes generate more free radicals.

Further investigation conducting heat/vacuum treatments on other metals such as zinc-silica and copper-silica PM surrogates can help understand if the other metal ions associated with superparamagnetic nanoparticles can yield a narrow g = 2.003 EPR signal. If other types of metals can yield the narrow g = 2.003 EPR signal, then the observed narrow g = 2.003 EPR

signal after 120 °C treatment in ambient $PM_{2.5}$ may be influenced by the presence of those other metals.

Future work should also assess if the small narrow g = 2.003 EPR signal is due to contamination, water/humidity effects, or adventitious carbon. It would be best to maintain the silica, PM surrogates, and PTFE filters in a cleanroom to keep it away from any exposure of particulates from the laboratory. If contamination is not the reasons for the EPR signal then EPR measurements of the silica, PM surrogates, and PTFE filters should be conducted under nitrogen and the EPR instrument should be in a room with low levels of humidity. This will help to determine if the g = 2.003 EPR signal is an artifact of water/humidity. If the nature of the EPR signal is still unclear, then grinding techniques used to prepare the silica and PM surrogates should be examined. It has been shown that grinding silica produces radicals on the particle surface (Vallyathan et al., 1988). Increasing the amount of time of grinding may show increases in the intensity of the small narrow g = 2.003 EPR signal. Also, it could be possible that the grinding is charging particle surfaces that could attract charged particulates from the atmosphere (i.e., adventitious carbon). Preparing the PM surrogates without grinding may demonstrate if there is a correlation or not between grinding and the narrow g = 2.003 EPR signal.

APPENDIX. PERMISSION FORM

ELSEVIER LICENSE
TERMS AND CONDITIONS

May 05, 2020

This Agreement between Louisiana State University -- Cholena Ren ("You") and Elsevier ("Elsevier") consists of your license details and the terms and conditions provided by Elsevier and Copyright Clearance Center.

License Number	4656070384447
License date	Aug 25, 2019
Licensed Content Publisher	Elsevier
Licensed Content Publication	Proceedings of the Combustion Institute
Licensed Content Title	Fe2O3 nanoparticle mediated molecular growth and soot inception from the oxidative pyrolysis of 1-methylnaphthalene
Licensed Content Author	M. Paul Herring,Phillip M. Potter,Hongyi Wu,Slawomir Lomnicki,Barry Dellinger
Licensed Content Date	Jan 1, 2013
Licensed Content Volume	34
Licensed Content Issue	1
Licensed Content Pages	9
Start Page	1749

End Page	1757
Type of Use	reuse in a thesis/dissertation
Portion	figures/tables/illustrations
Number of figures/tables/illustrations	1
Format	both print and electronic
Are you the author of this Elsevier article?	No
Will you be translating?	No
Original figure numbers	Fig. 1.
Requestor Location	Louisiana State University 136 Ansley Place Ct. HOUMA, LA 70360 United States Attn: Louisiana State University
Publisher Tax ID	98-0397604
Total	0.00 USD

Terms and Conditions

INTRODUCTION

1. The publisher for this copyrighted material is Elsevier. By clicking "accept" in connection with completing this licensing transaction, you agree that the following terms and conditions apply to this transaction (along with the Billing and Payment terms and conditions

established by Copyright Clearance Center, Inc. ("CCC"), at the time that you opened your Rightslink account and that are available at any time at http://myaccount.copyright.com).

GENERAL TERMS

2. Elsevier hereby grants you permission to reproduce the aforementioned material subject to the terms and conditions indicated.

3. Acknowledgement: If any part of the material to be used (for example, figures) has appeared in our publication with credit or acknowledgement to another source, permission must also be sought from that source. If such permission is not obtained then that material may not be included in your publication/copies. Suitable acknowledgement to the source must be made, either as a footnote or in a reference list at the end of your publication, as follows:

"Reprinted from Publication title, Vol /edition number, Author(s), Title of article / title of chapter, Pages No., Copyright (Year), with permission from Elsevier [OR APPLICABLE SOCIETY COPYRIGHT OWNER]." Also Lancet special credit - "Reprinted from The Lancet, Vol. number, Author(s), Title of article, Pages No., Copyright (Year), with permission from Elsevier."

4. Reproduction of this material is confined to the purpose and/or media for which permission is hereby given.

5. Altering/Modifying Material: Not Permitted. However figures and illustrations may be altered/adapted minimally to serve your work. Any other abbreviations, additions, deletions and/or any other alterations shall be made only with prior written authorization of Elsevier Ltd. (Please contact Elsevier at permissions@elsevier.com). No modifications can be made to any Lancet figures/tables and they must be reproduced in full.

6. If the permission fee for the requested use of our material is waived in this instance, please be advised that your future requests for Elsevier materials may attract a fee.

7. Reservation of Rights: Publisher reserves all rights not specifically granted in the combination of (i) the license details provided by you and accepted in the course of this licensing transaction, (ii) these terms and conditions and (iii) CCC's Billing and Payment terms and conditions.

8. License Contingent Upon Payment: While you may exercise the rights licensed immediately upon issuance of the license at the end of the licensing process for the transaction, provided that you have disclosed complete and accurate details of your proposed use, no license is finally effective unless and until full payment is received from you (either by publisher or by CCC) as provided in CCC's Billing and Payment terms and conditions. If full payment is not received on a timely basis, then any license preliminarily granted shall be deemed automatically revoked and shall be void as if never granted. Further, in the event that you breach any of these terms and conditions or any of CCC's Billing and Payment terms and conditions, the license is automatically revoked and shall be void as if never granted. Use of materials as described in a revoked license, as well as any use of the materials beyond the scope of an unrevoked license, may constitute copyright infringement

and publisher reserves the right to take any and all action to protect its copyright in the materials.

9. Warranties: Publisher makes no representations or warranties with respect to the licensed material.

10. Indemnity: You hereby indemnify and agree to hold harmless publisher and CCC, and their respective officers, directors, employees and agents, from and against any and all claims arising out of your use of the licensed material other than as specifically authorized pursuant to this license.

11. No Transfer of License: This license is personal to you and may not be sublicensed, assigned, or transferred by you to any other person without publisher's written permission.

12. No Amendment Except in Writing: This license may not be amended except in a writing signed by both parties (or, in the case of publisher, by CCC on publisher's behalf).

13. Objection to Contrary Terms: Publisher hereby objects to any terms contained in any purchase order, acknowledgment, check endorsement or other writing prepared by you, which terms are inconsistent with these terms and conditions or CCC's Billing and Payment terms and conditions. These terms and conditions, together with CCC's Billing and Payment terms and conditions (which are incorporated herein), comprise the entire agreement between you and publisher (and CCC) concerning this licensing transaction. In the event of any conflict between your obligations established by these terms and conditions and those established by CCC's Billing and Payment terms and conditions, these terms and conditions shall control.

14. Revocation: Elsevier or Copyright Clearance Center may deny the permissions described in this License at their sole discretion, for any reason or no reason, with a full refund payable to you. Notice of such denial will be made using the contact information provided by you. Failure to receive such notice will not alter or invalidate the denial. In no event will Elsevier or Copyright Clearance Center be responsible or liable for any costs, expenses or damage incurred by you as a result of a denial of your permission request, other than a refund of the amount(s) paid by you to Elsevier and/or Copyright Clearance Center for denied permissions.

LIMITED LICENSE

The following terms and conditions apply only to specific license types:

15. **Translation**: This permission is granted for non-exclusive world **English** rights only unless your license was granted for translation rights. If you licensed translation rights you may only translate this content into the languages you requested. A professional translator must perform all translations and reproduce the content word for word preserving the integrity of the article.

16. **Posting licensed content on any Website**: The following terms and conditions apply as follows: Licensing material from an Elsevier journal: All content posted to the web site must maintain the copyright information line on the bottom of each image; A hyper-text must be included to the Homepage of the journal from which you are licensing at

http://www.sciencedirect.com/science/journal/xxxxx or the Elsevier homepage for books at http://www.elsevier.com; Central Storage: This license does not include permission for a scanned version of the material to be stored in a central repository such as that provided by Heron/XanEdu.

Licensing material from an Elsevier book: A hyper-text link must be included to the Elsevier homepage at http://www.elsevier.com . All content posted to the web site must maintain the copyright information line on the bottom of each image.

Posting licensed content on Electronic reserve: In addition to the above the following clauses are applicable: The web site must be password-protected and made available only to bona fide students registered on a relevant course. This permission is granted for 1 year only. You may obtain a new license for future website posting.

17. **For journal authors:** the following clauses are applicable in addition to the above:

Preprints:

A preprint is an author's own write-up of research results and analysis, it has not been peer-reviewed, nor has it had any other value added to it by a publisher (such as formatting, copyright, technical enhancement etc.).

Authors can share their preprints anywhere at any time. Preprints should not be added to or enhanced in any way in order to appear more like, or to substitute for, the final versions of articles however authors can update their preprints on arXiv or RePEc with their Accepted Author Manuscript (see below).

If accepted for publication, we encourage authors to link from the preprint to their formal publication via its DOI. Millions of researchers have access to the formal publications on ScienceDirect, and so links will help users to find, access, cite and use the best available version. Please note that Cell Press, The Lancet and some society-owned have different preprint policies. Information on these policies is available on the journal homepage.

Accepted Author Manuscripts: An accepted author manuscript is the manuscript of an article that has been accepted for publication and which typically includes author-incorporated changes suggested during submission, peer review and editor-author communications.

Authors can share their accepted author manuscript:

- immediately
    - via their non-commercial person homepage or blog
    - by updating a preprint in arXiv or RePEc with the accepted manuscript
    - via their research institute or institutional repository for internal institutional uses or as part of an invitation-only research collaboration work-group
    - directly by providing copies to their students or to research collaborators for their personal use
    - for private scholarly sharing as part of an invitation-only work group on commercial sites with which Elsevier has an agreement

- After the embargo period
    - via non-commercial hosting platforms such as their institutional repository
    - via commercial sites with which Elsevier has an agreement

In all cases accepted manuscripts should:

- link to the formal publication via its DOI
- bear a CC-BY-NC-ND license - this is easy to do
- if aggregated with other manuscripts, for example in a repository or other site, be shared in alignment with our hosting policy not be added to or enhanced in any way to appear more like, or to substitute for, the published journal article.

Published journal article (JPA): A published journal article (PJA) is the definitive final record of published research that appears or will appear in the journal and embodies all value-adding publishing activities including peer review co-ordination, copy-editing, formatting, (if relevant) pagination and online enrichment.

Policies for sharing publishing journal articles differ for subscription and gold open access articles:

Subscription Articles: If you are an author, please share a link to your article rather than the full-text. Millions of researchers have access to the formal publications on ScienceDirect, and so links will help your users to find, access, cite, and use the best available version.

Theses and dissertations which contain embedded PJAs as part of the formal submission can be posted publicly by the awarding institution with DOI links back to the formal publications on ScienceDirect.

If you are affiliated with a library that subscribes to ScienceDirect you have additional private sharing rights for others' research accessed under that agreement. This includes use for classroom teaching and internal training at the institution (including use in course packs and courseware programs), and inclusion of the article for grant funding purposes.

Gold Open Access Articles: May be shared according to the author-selected end-user license and should contain a CrossMark logo, the end user license, and a DOI link to the formal publication on ScienceDirect.

Please refer to Elsevier's posting policy for further information.

18. **For book authors** the following clauses are applicable in addition to the above: Authors are permitted to place a brief summary of their work online only. You are not allowed to download and post the published electronic version of your chapter, nor may you scan the printed edition to create an electronic version. **Posting to a repository:** Authors are permitted to post a summary of their chapter only in their institution's repository.

19. **Thesis/Dissertation**: If your license is for use in a thesis/dissertation your thesis may be submitted to your institution in either print or electronic form. Should your thesis be published commercially, please reapply for permission. These requirements include permission for the Library and Archives of Canada to supply single copies, on demand, of the complete thesis and include permission for Proquest/UMI to supply single copies, on demand, of the complete thesis. Should your thesis be published commercially, please

REFERENCES

Alcalá, M. D.; Real, C. Synthesis based on the wet impregnation method and characterization of iron and iron oxide-silica nanocomposites. *Solid State Ionics* **2006,** *177* (9), 955-960.

Amama, P. B.; Lim, S.; Ciuparu, D.; Yang, Y.; Pfefferle, L.; Haller, G. L. Synthesis, Characterization, and Stability of Fe−MCM-41 for Production of Carbon Nanotubes by Acetylene Pyrolysis. *J. Phys. Chem. B* **2005,** *109* (7), 2645-2656.

Ault, A. P.; Peters, T. M.; Sawvel, E. J.; Casuccio, G. S.; Willis, R. D.; Norris, G. A.; Grassian, V. H. Single-Particle SEM-EDX Analysis of Iron-Containing Coarse Particulate Matter in an Urban Environment: Sources and Distribution of Iron within Cleveland, Ohio. *Environ. Sci. Technol.* **2012,** *46* (8), 4331-4339.

Balek, V.; Subrt, J. Thermal behaviour of iron(III) oxide hydroxides. *Pure & Appl. Chem.* **1995,** *67* (11), 1839.

Beletskii, I. P., Gorlov, Y.I. & Chuiko, A.A. EPR spectra of impurity Fe3+ ions in silica gels. *Theor. Exp. Chem.* **1980,** *16* (2), 229-231.

Berger, R.; Bissey, J.-C.; Kliava, J.; Daubric, H.; Estournès, C. Temperature dependence of superparamagnetic resonance of iron oxide nanoparticles. *J. Magn. Magn. Mater.* **2001,** *234* (3), 535-544.

Berlier, G.; Spoto, G.; Bordiga, S.; Ricchiardi, G.; Fisicaro, P.; Zecchina, A.; Rossetti, I.; Selli, E.; Forni, L.; Giamello, E.; Lamberti, C. Evolution of extraframework iron species in Fe silicalite 1. Effect of Fe content, activation temperature, and interaction with redox agents. *J. Catal.* **2002,** *208*, 64-82.

Bernal, J. The Oxides and Hydroxides of Iron and Their Structural Inter-Relationships. *Clay Miner.* **1959,** *4*, 15-30.

Bhaumik, A.; Samanta, S.; Mal, N. Iron oxide nanoparticles stabilized inside highly ordered mesoporous silica. *Pramana* **2005,** *65*, 855-862.

Bordiga, S.; Buzzoni, R.; Geobaldo, F.; Lamberti, C.; Giamello, E.; Zecchina, A.; Leofanti, G.; Petrini, G.; Tozzola, G.; Vlaic, G. Structure and Reactivity of Framework and Extraframework Iron in Fe-Silicalite as Investigated by Spectroscopic and Physicochemical Methods. *J. Catal.* **1996,** *158* (2), 486-501.

Bourlinos, A.; Simopoulos, A.; Petridis, D.; Okumura, H.; Hadjipanayis, G. Silica–Maghemite Nanocomposites. *Adv. Mater.* **2001,** *13* (4), 289-291.

Breeuwsma, A. Adsorption of ions on hematite (alpha-Fe2O3) : a colloid-chemical study. Doctoral Thesis, Wageningen University, NL, 1973.

Brook Robert, D.; Rajagopalan, S.; Pope, C. A.; Brook Jeffrey, R.; Bhatnagar, A.; Diez-Roux Ana, V.; Holguin, F.; Hong, Y.; Luepker Russell, V.; Mittleman Murray, A.; Peters, A.; Siscovick, D.; Smith Sidney, C.; Whitsel, L.; Kaufman Joel, D. Particulate Matter Air Pollution and Cardiovascular Disease. *Circulation* **2010,** *121* (21), 2331-2378.

Bywalez, R.; Karacuban, H.; Nienhaus, H.; Schulz, C.; Wiggers, H. Stabilization of mid-sized silicon nanoparticles by functionalization with acrylic acid. *Nanoscale Res. Lett.* **2012,** *7* (1), 76-76.

Cadet, J.; Delatour, T.; Douki, T.; Gasparutto, D.; Pouget, J.-P.; Ravanat, J.-L.; Sauvaigo, S. Hydroxyl radicals and DNA base damage. *Mutat. Res., Fundam. Mol. Mech. Mutagen.* **1999,** *424* (1), 9-21.

Campbell, A. S.; Schwertmann, U. Iron oxide mineralogy of placic horizons. *J. Soil Sci.* **1984,** *35* (4), 569-582.

Cannas, C.; Gatteschi, D.; Musinu, A.; Piccaluga, G.; Sangregorio, C. Structural and Magnetic Properties of Fe2O3 Nanoparticles Dispersed over a Silica Matrix. *J. Phys. Chem. B* **1998,** *102* (40), 7721-7726.

Castle, J. E. The Composition of Metal Surfaces After Atmospheric Exposure: An Historical Perspective. *J. Adhes.* **2008,** *84* (4), 368-388.

Cheung, K.; Shafer, M. M.; Schauer, J. J.; Sioutas, C. Diurnal Trends in Oxidative Potential of Coarse Particulate Matter in the Los Angeles Basin and Their Relation to Sources and Chemical Composition. *Environ. Sci. Technol.* **2012,** *46* (7), 3779-3787.

Church, D. F.; Pryor, W. A. Free-radical chemistry of cigarette smoke and its toxicological implications. *Environ. Health Perspect.* **1985,** *64*, 111-126.

Cormier, S. A.; Lomnicki, S.; Backes, W.; Dellinger, B. Origin and health impacts of emissions of toxic by-products and fine particles from combustion and thermal treatment of hazardous wastes and materials. *Environ. Health Perspect.* **2006,** *114* (6), 810-817.

Dellinger, B.; Khachatryan, L.; Masko, S.; Lomnicki, S. Free Radicals in Tobacco Smoke. *Mini-Rev. Org. Chem.* **2011,** *8*, 427.

Dellinger, B.; Pryor, W. A.; Cueto, B.; Squadrito, G. L.; Deutsch, W. A. The role of combustion-generated radicals in the toxicity of PM2.5. *Proc. Combust. Inst.* **2000,** *28* (2), 2675-2681.

Dellinger, B.; Pryor, W. A.; Cueto, R.; Squadrito, G. L.; Hegde, V.; Deutsch, W. A. Role of Free Radicals in the Toxicity of Airborne Fine Particulate Matter. *Chem. Res. Toxicol.* **2001,** *14* (10), 1371-1377.

deVries, J. E.; Haack, L. P.; Coduti, P. L. Measurement of Carbon on Cold-Rolled Steel: A Comparative Study Using Surface Analytical and Coulometric Methodologies. *Ind. Eng. Chem. Res.* **1994,** *33* (11), 2618-2630.

Dixon, J. B.; Weed, S. B. *Minerals in Soil Environments*. 2nd ed.; Soil Science Society of America: Madison, WI, 1989.

Djebbar, M.; Djafri, F.; Bouchekara, M.; Djafri, A. Adsorption of phenol on natural clay. *Appl. Water Sci.* **2012,** *2* (2), 77-86.

Du, P.; Du, R.; Ren, W.; Lu, Z.; Zhang, Y.; Fu, P. Variations of bacteria and fungi in PM2.5 in Beijing, China. *Atmos. Environ.* **2018,** *172*, 55-64.

Duan, J.; Tan, J. Atmospheric heavy metals and Arsenic in China: Situation, sources and control policies. *Atmos. Environ.* **2013,** *74*, 93-101.

Dyrek, K. Chemisorption of oxygen on transition metal oxides studied by EPR. *Adv. Mol. Relax.* **1973,** *5* (1), 211-218.

Eaton GR, E. S., Barr DP, Weber RT. *Quantitative EPR*. Springer-Verlag/Wein: New York, 2010.

EPA. NAAQS Table. https://www.epa.gov/criteria-air-pollutants/naaqs-table (accessed Janurary 18, 2020).

EPA. Particulate Matter (PM) Basics. https://www.epa.gov/pm-pollution/particulate-matter-pm-basics#PM (accessed April 24, 2018).

Fan, Y.; Bao, Y.; Song, Z.; Sun, Z.; Wang, D.; Han, D.; Niu, L. Controllable synthesis of coloured Ag0/AgCl with spectral analysis for photocatalysis. *RSC Adv.* **2018,** *8* (44), 24812-24818.

Ferretti, A. M.; Oliva, C.; Forni, L.; Berlier, G.; Zecchina, A.; Lamberti, C. Evolution of Extraframework Iron Species in Fe Silicalite: 2. Effect of Steaming. *J. Catal.* **2002,** *208* (1), 83-88.

Gehling, W. Environmentally Persistent Free Radicals (Epfrs) In Pm2.5: Their Contribution To Hydroxyl Radical Formation and Atmospheric Transformation. Ph.D. dissertation, Louisiana State University, Baton Rouge, LA, 2013.

Gehling, W.; Dellinger, B. Environmentally Persistent Free Radicals and Their Lifetimes in PM2.5. *Environ. Sci. Technol.* **2013,** *47* (15), 8172-8178.

Gehling, W.; Khachatryan, L.; Dellinger, B. Hydroxyl Radical Generation from Environmentally Persistent Free Radicals (EPFRs) in PM2.5. *Environ. Sci. Technol.* **2014,** *48* (8), 4266-4272.

Geinguenaud, F.; Banissi, C.; Carpentier, A. F.; Motte, L. Iron Oxide Nanoparticles Coated with a Phosphorothioate Oligonucleotide and a Cationic Peptide: Exploring Four Different Ways of Surface Functionalization. *Nanomaterials* **2015,** *5* (4), 1588-1609.

Gervasini, A.; Manzoli, M.; Martra, G.; Ponti, A.; Ravasio, N.; Sordelli, L.; Zaccheria, F. Dependence of Copper Species on the Nature of the Support for Dispersed CuO Catalysts. *J. Phys. Chem. B* **2006,** *110* (15), 7851-7861.

Goldfarb, D.; Bernardo, M.; Strohmaier, K. G.; Vaughan, D. E. W.; Thomann, H. Characterization of Iron in Zeolites by X-band and Q-Band ESR, Pulsed ESR, and UV-Visible Spectroscopies. *J. Am. Chem. Soc.* **1994,** *116* (14), 6344-6353.

Goss, C. J. The kinetics and reaction mechanism of the goethite to hematite transformation. *Mineral. Mag.* **1987,** *51* (361), 437-451.

Greczynski, G.; Hultman, L. X-ray photoelectron spectroscopy: Towards reliable binding energy referencing. *Prog. Mater. Sci.* **2020,** *107*, 100591.

Griffin, R. The Sources and Impacts of Tropospheric Particulates. *Nat. Educ. Knowl.* **2013,** *4* (5), 1.

Guarieiro, A. L. N.; Santos, J. V. d. S.; Eiguren-Fernandez, A.; Torres, E. A.; da Rocha, G. O.; de Andrade, J. B. Redox activity and PAH content in size-classified nanoparticles emitted by a diesel engine fuelled with biodiesel and diesel blends. *Fuel* **2014,** *116*, 490-497.

Hamill, S. Unveiling a Museum, a Pennsylvania Town Remembers the Smog That Killed 20. https://www.nytimes.com/2008/11/02/us/02smog.html (accessed April 24, 2018).

Hazari, M. S.; Stratford, K. M.; Krantz, Q. T.; King, C.; Krug, J.; Farraj, A. K.; Gilmour, M. I. Comparative Cardiopulmonary Effects of Particulate Matter- And Ozone-Enhanced Smog Atmospheres in Mice. *Environ. Sci. Technol.* **2018,** *52* (5), 3071-3080.

Herring, M. P. Fe(III)2O3 Nanoparticle Mediated Molecular Growth and Soot Particle Inception from the Oxidative Pyrolysis of 1-Methylnaphthalene. Ph.D. dissertation, Louisiana State University, Baton Rouge, LA, 2013.

Herring, M. P.; Khachatryan, L.; Dellinger, B. Speciation of Iron (III) Oxide Nanoparticles and Other Paramagnetic Intermediates during High-Temperature Oxidative Pyrolysis of 1-Methylnaphthalene. *World Acad Sci Eng Technol.* **2015,** *9* (7), 804-812.

Herring, M. P.; Potter, P. M.; Wu, H.; Lomnicki, S.; Dellinger, B. Fe(2)O(3) nanoparticle mediated molecular growth and soot inception from the oxidative pyrolysis of 1-methylnaphthalene. *Proc. Combust. Inst.* **2013,** *34* (1), 1749-1757.

Hosseini-Zori, M.; Bondioli, F.; Manfredini, T.; Taheri-Nassaj, E. Effect of synthesis parameters on a hematite–silica red pigment obtained using a coprecipitation route. *Dyes Pigm.* **2008,** *77* (1), 53-58.

IARC. Outdoor air pollution a leading environmental cause of cancer deaths. https://www.iarc.fr/news-events/iarc-outdoor-air-pollution-a-leading-environmental-cause-of-cancer-deaths/ (accessed May 8, 2018).

Iraj, K.; Mosivand, S. Phase Transition of Electrooxidized Fe3O4 to gamma and alpha-Fe2O3 Nanoparticles Using Sintering Treatment. *Acta Phys. Pol., A* **2014,** *125*, 1210-1214.

Jones, A. Electron Diffraction and the Study of Ferrihydrite Coatings on Kaolinite. *Clay Miner.* **1986,** *21*, 85-92.

Kenny, L. C.; Gussman, R.; Meyer, M. Development of a Sharp-Cut Cyclone for Ambient Aerosol Monitoring Applications. *Aerosol Sci. Technol.* **2000,** *32* (4), 338-358.

Kiruri, L. W.; Khachatryan, L.; Dellinger, B.; Lomnicki, S. Effect of Copper Oxide Concentration on the Formation and Persistency of Environmentally Persistent Free Radicals (EPFRs) in Particulates. *Environ. Sci. Technol.* **2014,** *48* (4), 2212-2217.

Koenig, J.; Balfanz, E.; Funcke, W.; Romanowski, T. Determination of oxygenated polycyclic aromatic hydrocarbons in airborne particulate matter by capillary gas chromatography and gas chromatography/mass spectrometry. *Anal. Chem.* **1983,** *55* (4), 599-603.

Krötz, F.; Sohn, H. Y.; Gloe, T.; Zahler, S.; Riexinger, T.; Schiele, T. M.; Becker, B. F.; Theisen, K.; Klauss, V.; Pohl, U. NAD(P)H oxidase–dependent platelet superoxide anion release increases platelet recruitment. *Blood* **2002,** *100* (3), 917-924.

Labs, M. PQ 200 Air Sampler User Manual. https://bgi.mesalabs.com/pq200-particulate-sampler/ (accessed January 31, 2020).

Lakey, P. S. J.; Berkemeier, T.; Tong, H.; Arangio, A. M.; Lucas, K.; Pöschl, U.; Shiraiwa, M. Chemical exposure-response relationship between air pollutants and reactive oxygen species in the human respiratory tract. *Sci. Rep.* **2016,** *6*, 32916.

Lassoued, A.; Dkhil, B.; Gadri, A.; Ammar, S. Control of the shape and size of iron oxide (α-Fe2O3) nanoparticles synthesized through the chemical precipitation method. *Results Phys.* **2017,** *7*, 3007-3015.

Ledoux, F.; Zhilinskaya, E.; Bouhsina, S.; Courcot, L.; Bertho, M.-L.; Aboukaïs, A.; Puskaric, E. EPR investigations of Mn2+, Fe3+ ions and carbonaceous radicals in atmospheric particulate aerosols during their transport over the eastern coast of the English Channel. *Atmos. Environ.* **2002,** *36* (6), 939-947.

Ledoux, F.; Zhilinskaya, E. A.; Courcot, D.; Aboukaïs, A.; Puskaric, E. EPR investigation of iron in size segregated atmospheric aerosols collected at Dunkerque, Northern France. *Atmos. Environ.* **2004,** *38* (8), 1201-1210.

Li, H.; Guo, H.; Pan, B.; Liao, S.; Zhang, D.; Yang, X.; Min, C.; Xing, B. Catechol degradation on hematite/silica–gas interface as affected by gas composition and the formation of environmentally persistent free radicals. *Sci. Rep.* **2016,** *6* (1), 24494.

Lin, D. H.; Coudurier, G.; Vedrine, J. C. Fe-ZSM-5: Physicochemical and Catalytic Properties. In *Studies in Surface Science and Catalysis*, Jacobs, P. A.; van Santen, R. A., Eds. Elsevier: 1989; Vol. 49, pp 1431-1448.

Liyanage, N. Synthesis, characterization, and investigation of the catalytic activity of NiO, CuO, and NiO-CuO nanoparticles on silica as surrogates of combustion-generated nanoparticles. Ph.D. dissertation, Louisiana State University, Baton Rouge, LA, 2014.

Loktev, M. I.; Slinkin, A. A. Investigation of the ESR Spectra of Adsorbed Radical-ions as a Method for the Study of the Oxidation-reduction Properties of Zeolites. *Russ. Chem. Rev.* **1976,** *45* (9), 807-822.

Lomnicki, S.; Truong, H.; Vejerano, E.; Dellinger, B. Copper Oxide-Based Model of Persistent Free Radical Formation on Combustion-Derived Particulate Matter. *Environ. Sci. Technol.* **2008,** *42* (13), 4982-4988.

Machala, L.; Zboril, R.; Gedanken, A. Amorphous Iron(III) OxideA Review. *J. Phys. Chem. B* **2007,** *111* (16), 4003-4018.

Marceau, E. C., X.; Che, M. Impregnation and Drying. In *Synthesis of Solid Catalysts*, Jong, D., Ed. Wiley-VCH Verlag GmbH & Co. KGaA: Weinheim (DE), 2009; pp 59-82.

Maskos, Z.; Khachatryan, L.; Cueto, R.; Pryor, W. A.; Dellinger, B. Radicals from the Pyrolysis of Tobacco. *Energy Fuels* **2005,** *19* (3), 791-799.

McBride, M. B.; Kung, K.-H. Adsorption of phenol and substituted phenols by iron oxides. *Environ. Toxicol. Chem.* **1991,** *10* (4), 441-448.

Merget, R.; Bauer, T.; Küpper, H.; Philippou, S.; Bauer, H.; Breitstadt, R.; Bruening, T. Health hazards due to the inhalation of amorphous silica. *Arch. Toxicol.* **2002,** *75* (11), 625-634.

Naono, H.; Fujiwara, R.; Yagi, M. Determination of physisorbed and chemisorbed waters on silica gel and porous silica glass by means of desorption isotherms of water vapor. *J. Colloid Interface Sci.* **1980,** *76* (1), 74-82.

Nwosu, U.; Khachatryan, L.; Youm, S.; Roy, A.; Dela Cruz, A. L.; Nesterov, E.; Dellinger, B.; Cook, R. Model System Study of Environmentally Persistent Free Radicals Formation in a

Semiconducting Polymer Modified Copper Clay System at Ambient Temperature. *RSC Adv.* **2016,** *6*.

Palomares-Sánchez, S.; Selina, P.; Martinez, J. R.; Ruiz, F. Determination of phases of α-Fe2O3:SiO2 compound by the Rietveld refinement. *Rev. Mex. Fis.* **2002,** *48*, 438-442.

Patterson, M. C.; DiTusa, M. F.; McFerrin, C. A.; Kurtz, R. L.; Hall, R. W.; Poliakoff, E. D.; Sprunger, P. T. Formation of environmentally persistent free radicals (EPFRs) on ZnO at room temperature: Implications for the fundamental model of EPFR generation. *Chem. Phys. Lett.* **2017,** *670*, 5-10.

Patterson, M. C.; Keilbart, N. D.; Kiruri, L. W.; Thibodeaux, C. A.; Lomnicki, S.; Kurtz, R. L.; Poliakoff, E. D.; Dellinger, B.; Sprunger, P. T. EPFR formation from phenol adsorption on Al2O3 and TiO2: EPR and EELS studies. *Chem. Phys.* **2013,** *422*, 277-282.

Piao, H.; McIntyre, N. S. Adventitious carbon growth on aluminium and gold–aluminium alloy surfaces. *Surf. Interface Anal.* **2002,** *33* (7), 591-594.

Polichetti, G.; Cocco, S.; Spinali, A.; Trimarco, V.; Nunziata, A. Effects of particulate matter (PM10, PM2.5 and PM1) on the cardiovascular system. *Toxicology* **2009,** *261* (1), 1-8.

Pope, C. A., 3rd; Burnett, R. T.; Turner, M. C.; Cohen, A.; Krewski, D.; Jerrett, M.; Gapstur, S. M.; Thun, M. J. Lung cancer and cardiovascular disease mortality associated with ambient air pollution and cigarette smoke: shape of the exposure-response relationships. *Environ. Health Perspect.* **2011,** *119* (11), 1616-1621.

Richter, H.; Howard, J. B. Formation of polycyclic aromatic hydrocarbons and their growth to soot—a review of chemical reaction pathways. *Prog. Energy Combust. Sci.* **2000,** *26* (4), 565-608.

Rogula-Kozłowska, W.; Klejnowski, K.; Rogula-Kopiec, P.; Ośródka, L.; Krajny, E.; Błaszczak, B.; Mathews, B. Spatial and seasonal variability of the mass concentration and chemical composition of PM2.5 in Poland. *Air Qual., Atmos. Health* **2014,** *7* (1), 41-58.

Ross, M. M.; Chedekel, M. R.; Risby, T. H.; Lestz, S. S.; Yasbin, R. E. Electron paramagnetic resonance spectrometry of diesel particulate matter. *Environ. Int.* **1982,** *7* (5), 325-329.

Rouault, T. *Iron-Sulfur Clusters in Chemistry and Biology*. 2nd ed.; De Gruyter: 2017; Vol. Volume 1 Characterization, Properties and Applications.

Sagar, V. Electron spin resonance based investigations of cooper doped zeolites as selective catalytic reduction catalysts for deNOx applications. The State University of New Jersey, Electronic Thesis and Dissertation Library, 2015.

Sawhney, B.; Kozloski, R.; Isaacson, P.; Martin, G. Polymerization of 2,6-Dimethylphenol on Smectite Surfaces. *Clays Clay Miner.* **1984,** *32*, 108-114.

Schwertmann, U. Transformation of Hematite to Goethite in Soils. *Nature* **1971,** *232* (5313), 624-625.

Schwertmann, U.; Murad, E. Effect of pH on the Formation of Goethite and Hematite from Ferrihydrite. *Clays Clay Miner.* **1983,** *31* (4), 277-284.

Sjoholm, P.; Ingham, D. B.; Lehtimaki, M.; Perttu-Roiha, L.; Goodfellow, H.; Torvela, H. 13 - Gas-Cleaning Technology. In *Industrial Ventilation Design Guidebook*, Goodfellow, H.; Tähti, E., Eds. Academic Press: San Diego, 2001; pp 1197-1316.

Su, W.-F. Characterization of Polymer. In *Principles of Polymer Design and Synthesis*, Su, W.-F., Ed. Springer Berlin Heidelberg: Berlin, Heidelberg, 2013; Vol. 82, pp 89-110.

Tian, L.; Koshland, C. P.; Yano, J.; Yachandra, V. K.; Yu, I. T. S.; Lee, S. C.; Lucas, D. Carbon-Centered Free Radicals in Particulate Matter Emissions from Wood and Coal Combustion. *Energy Fuels* **2009,** *23* (5), 2523-2526.

Tuel, A.; Arcon, I.; Millet, J. M. M. Investigation of sructural iron species in Fe-mesoporous silicas by spectroscopic techniques. *J. Chem. Soc., Faraday Trans.* **1998,** *94*, 3501-3510.

Upadhyay, S. *Chemical Kinetics and Reaction Dynamics*. Anamaya Publishers: India, 2006.

Valavanidis, A.; Fiotakis, K.; Bakeas, E.; Vlahogianni, T. Electron paramagnetic resonance study of the generation of reactive oxygen species catalysed by transition metals and quinoid redox cycling by inhalable ambient particulate matter. *Redox Rep.* **2005,** *10* (1), 37-51.

Valavanidis, A.; Iliopoulos, N.; Gotsis, G.; Fiotakis, K. Persistent free radicals, heavy metals and PAHs generated in particulate soot emissions and residue ash from controlled combustion of common types of plastic. *J. Hazard. Mater.* **2008,** *156* (1), 277-284.

Vallyathan, V.; Shi, X.; Dalal, N. S.; Irr, W.; Castranova, V. Generation of Free Radicals from Freshly Fractured Silica Dust: Potential Role in Acute Silica-induced Lung Injury. *Am. Rev. Respit. Dis.* **1988,** *138* (5), 1213-1219.

Vejerano, E. Formation and Stabilization of Combustion-Generated Environmentally Persistent Free Radicals on Transition Metal Oxides Suppoted on Silica. Ph.D. dissertation, Louisiana State University, Baton Rouge, LA, 2011.

Vejerano, E.; Lomnicki, S.; Dellinger, B. Formation and Stabilization of Combustion-Generated Environmentally Persistent Free Radicals on an Fe(III)2O3/Silica Surface. *Environ. Sci. Technol.* **2011,** *45* (2), 589-594.

Vejerano, E.; Lomnicki, S.; Dellinger, B. Lifetime of combustion-generated environmentally persistent free radicals on Zn(II)O and other transition metal oxides. *J. Environ. Monit.* **2012,** *14*, 2803-6.

Vejerano, E.; Lomnicki, S. M.; Dellinger, B. Formation and Stabilization of Combustion-Generated, Environmentally Persistent Radicals on Ni(II)O Supported on a Silica Surface. *Environ. Sci. Technol.* **2012,** *46* (17), 9406-9411.

Wang, M.; Hu, H.-p.; Chen, Q.-y.; Ji, G.-f. FT-IR, XPS, and DFT Study of Adsorption Mechanism of Sodium Acetohydroxamate onto Goethite or Hematite. *Chin. J. Chem. Phys.* **2016,** *29*, 308-318.

Weckhuysen, B.; Wang, D.; Rosynek, M. B.; H. Lunsford, J. Catalytic Conversion of Methane into Aromatic Hydrocarbons over Iron Oxide Loaded ZSM-5 Zeolites. *Angew. Chem., Int. Ed. Engl.* **1997,** *36*.

West, J. J.; Cohen, A.; Dentener, F.; Brunekreef, B.; Zhu, T.; Armstrong, B.; Bell, M. L.; Brauer, M.; Carmichael, G.; Costa, D. L.; Dockery, D. W.; Kleeman, M.; Krzyzanowski, M.; Künzli, N.; Liousse, C.; Lung, S.-C. C.; Martin, R. V.; Pöschl, U.; Pope, C. A.; Roberts, J. M.; Russell, A. G.; Wiedinmyer, C. "What We Breathe Impacts Our Health: Improving Understanding of the Link between Air Pollution and Health". *Environ. Sci. Technol.* **2016,** *50* (10), 4895-4904.

Xin, H.; Liu, J.; Fan, F.; Feng, Z.; Jia, G.; Yang, Q.; Li, C. Mesoporous ferrosilicates with high content of isolated iron species synthesized in mild buffer solution and their catalytic application. *Microporous and Mesoporous Mater.* **2008,** *113* (1), 231-239.

Yi, P.; Chen, Q.; Li, H.; Lang, D.; Zhao, Q.; Pan, B.; Xing, B. A Comparative Study on the Formation of Environmentally Persistent Free Radicals (EPFRs) on Hematite and Goethite: Contribution of Various Catechol Degradation Byproducts. *Environ. Sci. Technol.* **2019**.

Zhou, X.; Chen, Q.; Tao, Y.; Weng, H. Effect of vacuum impregnation on the performance of Co/SiO2 Fischer-Tropsch catalyst. *J. Nat. Gas Chem.* **2011,** *20* (4), 350-355.

VITA

Cholena Ren was born in Florida. She earned a Bachelor of Science degree in Chemistry from the University of West Florida in May 2012. Subsequently she was accepted into Louisiana State University to purse a Ph.D. degree in Chemistry. She expects to graduate with her Ph.D. degree in August 2020.